UNIVERSITÄT LEIPZIG
Fakultät für Physik und Geowissenschaften
Institut für Meteorologie

Analysis of water vapour mixing ratio profiles in the Arctic from Raman lidar measurements during the MOSAiC-campaign

Master thesis

Leipzig, 11th August 2022

submitted by: Clara Seidel
Course of studies: Meteorology

Contact person: Dr. Dietrich Althausen
First supervisor: Dr. Albert Ansmann
Second supervisor: Prof. Dr. Manfred Wendisch

Contents

1 Introduction **3**

2 Meteorological conditions in the Arctic and MOSAiC **6**
2.1 Characteristics of the Arctic . . . 6
2.1.1 The definition of the Arctic and the seasonal cycle of the Arctic climate system . . . 6
2.1.2 The Atmospheric circulation in the Arctic . . . 7
2.2 Water vapour in the Arctic . . . 7
2.2.1 The atmospheric water budget and moisture transport . . . 7
2.2.2 The impact of water vapour on the radiation budget . . . 8
2.3 The MOSAiC-campaign . . . 9
2.3.1 The campaign . . . 9
2.3.2 Meteorological conditions and the Arctic Oscillation index between October 2019 and February 2020 . . . 9

3 Theory: Instrumentation and Methods **11**
3.1 Instrumentation . . . 11
3.1.1 The Raman lidar . . . 11
3.1.2 The radiosonde . . . 13
3.1.3 The Microwave Radiometer . . . 14
3.1.4 The pyrgeometer . . . 14
3.2 Lidar data processing . . . 15
3.2.1 Determination of the water vapour mixing ratio . . . 15
3.2.2 Processing of the lidar signals from water vapour and nitrogen . . . 16
3.2.3 Calculation of the differential transmission . . . 17
3.2.4 Dependence of the signal ratio on the temperature of the atmospheric scatterers . . . 20
3.2.5 Determination of the integrated water vapour . . . 20
3.2.6 Error analysis . . . 21
3.3 Calibration methods . . . 22
3.3.1 Calibration with radiosonde . . . 22
3.3.2 Calibration with integrated water vapour . . . 23
3.3.3 Determination of one calibration constant for the MOSAiC winter data . 24

4 Calibration results **25**
4.1 Technical criteria for the determination of the calibration constants . . . 25
4.1.1 Calibration with radiosonde . . . 25
4.1.2 Calibration with integrated water vapour . . . 26
4.1.3 Influence of the chosen threshold of the SNR . . . 27

4.1.4 Choice of calibration time periods . . . 28
4.2 Discussion of the calibration methods . . . 28
4.3 Determination of the final calibration constants . . . 32

5 Analysis of water vapour profiles 36
5.1 Methods to analyse profiles of the WVMR . . . 36
5.1.1 Definition of atmospheric layers . . . 37
5.1.2 Analysis of gradients . . . 39
5.1.3 Determination of a characteristic temperature . . . 39
5.2 Case studies . . . 40
5.2.1 Water vapour profiles during the negative phase of the Arctic Oscillation - Case 13 November 2019 . . . 40
5.2.2 Water vapour profiles during the positive phase of the Arctic Oscillation - Case 11 February 2020 . . . 44
5.2.3 Summary from case studies . . . 47
5.3 The influence of the vertical distributed WVMR on the downward longwave radiation during clear-sky conditions . . . 48
5.3.1 Results from correlating IWV, DLR and temperature . . . 48
5.3.2 Discussion of the correlation between IWV, DLR and temperature . . . 50
5.4 Statistical analyses of WVMR profiles and the influence of the Arctic Oscillation 51
5.4.1 Choice of measurement cases for the statistical evaluations . . . 51
5.4.2 Temporal development of the WVMR and the temperature . . . 52
5.4.3 Analysis of vertical water vapour layers . . . 53
5.4.4 Analysis of the vertical gradients of the WVMR . . . 56

6 Conclusion and Outlook 59

7 Bibliography 64

List of Symbols and Abbreviations 69

List of Figures 71

List of Tables 72

A Additional figures 73
A.1 Synoptic conditions for the case studies . . . 73

Chapter 1

Introduction

Water vapour in the atmosphere is a major greenhouse gas and plays an important role for the climate (Chahine, 1992). Its distribution is highly variable in time and space on global and regional scales (Jacob, 2001). While the total column water vapour is large in the tropics, the conditions are very dry in the polar regions. The global atmospheric circulation provides for the exchange of airmasses around the globe and the compensation of the energy surplus at the equator and the energy deficit at the poles. An important part of this energy is transported as latent heat in form of water vapour within the airmasses. Beside its contribution as latent heat to the energy budget of the atmosphere, water vapour contributes to the radiation budget by the emission of longwave radiation. The downward longwave radiation is an important part of the greenhouse effect and impacts the surface temperature and energy budget (Doyle et al., 2011). As the atmospheric temperatures increase due to climate change, the atmosphere can contain more water vapour (O'Gorman & Muller, 2010), which leads to a positive water vapour feedback (Ghatak & Miller, 2013). In the atmosphere itself, water vapour is prerequisite for many physical processes like the formation of clouds and precipitation. Sources for atmospheric moisture are evaporation from the Earth's surface or from cloud droplets in the atmosphere. Sinks are mainly precipitation and cloud or ice formation. The transport of water vapour is a sink in one region and a source in another region (Vázquez et al., 2016).

The Arctic is a key-region for climate change, as it is warming much faster than the rest of the globe (Graversen et al., 2008; Screen & Simmonds, 2010; Wendisch et al., 2017; Boeke & Taylor, 2018). Beside the changes in surface temperatures, changes in the moisture content were reported by Screen & Simmonds (2010), Rinke et al. (2019) and others. The moistening trend is regional and seasonal different (Rinke et al., 2019), and differs also vertically (Graversen et al., 2008; Screen & Simmonds, 2010). In the mentioned studies, two main sources for the increasing moisture in the Arctic were presented. On the one hand, changes at the surface, like snow and sea-ice retreat, lead to an enhanced evaporation and more moisture near the surface (Screen & Simmonds, 2010). On the other hand, the advection of warm and moist air plays a role in larger heights (Graversen et al., 2008). The role of the horizontal transport of water vapour with the atmospheric circulation was considered in many studies (Vázquez et al., 2016; Nash et al., 2018; Naakka et al., 2019; Rinke et al., 2019; Nygård et al., 2019, 2020). It was shown, that atmospheric rivers, which are narrow pathways of large amounts of water vapour, play an important role for the water budget of the Arctic and the meridional transport of water vapour into the Arctic (Nash et al., 2018). The influence of the large-scale circulation on the distribution of water vapour, but also on the longwave radiation, is mainly determined by the horizontal moisture transport and the large-scale pressure distribution (Nygård et al., 2019). Changes in the mid-latitude circulation determines the temperature in many parts of

the Arctic, which impacts the trend in integrated water vapour and moisture transport (Nygård et al., 2020).
Several studies used large-scale circulation indices, like the Arctic Oscillation (AO) index to quantify the large-scale circulation (Devasthale et al., 2012; Nygård et al., 2019). The different phases of the AO are linked to the temperatures (Graversen et al., 2008), but also to the moisture transport into the Arctic (Nygård et al., 2019). Beside, the specific synoptics at one place can be very different for the same phase of the AO (Nygård et al., 2019). The AO index can be used as a first overview over the atmospheric circulation, but the specific synoptics have to be taken into account for the evaluation of specific cases.
Moreover, the atmospheric water vapour impacts the surface radiation budget. Doyle et al. (2011) emphasised the importance of water vapour intrusions on the surface energy budget in the Arctic winter. Ruckstuhl et al. (2007) and Ghatak & Miller (2013) considered the relationship between monthly mean values of the downward longwave radiation (DLR) and the integrated water vapour (IWV) in the Alps and in the Arctic and found a correlation by a power function. The correlation function shows a much steeper slope for small IWV values, which occur in the Arctic winter than for higher IWV in summer. This correlation implies a huge influence of temporal changes in the wintertime IWV due to the advection of water vapour layers on small timescales or an increasing moisture content in context with the Arctic warming. The influence of the IWV on the radiation budget can be evaluated by model results, but measurements of the vertical distributed water vapour and the downward longwave radiation would deliver new detailed insights in the correlation of those two quantities.

Most studies mentioned above are based on the evaluation of model data, satellite measurements of integrated values or measurements at the north coast of the continents, because there are no regular measurements in the Central Arctic. Satellite measurements are regularly available, but none of them covers the whole Arctic (Rinke et al., 2019). Models instead use the input from data assimilation of all available measurements, but since the data coverage over the Arctic is low and some of the processes are still not fully understood, the models contain uncertainties (Rinke et al., 2019). For that reason, local measurements in the Central Arctic are needed to investigate the processes and improve the models. One large campaign, that conducted measurements in the Central Arctic for one full year, was the ‘Surface Heat Budget of the Arctic Ocean’ (SHEBA) campaign (Uttal et al., 2002; Andreas et al., 2002). During this campaign, a ship was frozen in the ice from 2 October 1997 to 11 October 1998 in the Central Arctic north of Alaska and many different meteorological parameters were measured on the ice around the ship. Based on the experiences from this campaign, another campaign was carried out in winter 2019/20. For the ‘Multidisciplinary drifting Observatory for the Study of Arctic Climate’ (MOSAiC) campaign (Shupe et al., 2020, 2022), the German research vessel Polarstern was frozen in the Arctic ice for one full year from September 2019 until October 2020. The cooperation and contribution of scientists and institutions from all over the world enabled year-round measurements of many parameters in the atmosphere, the ocean, the ice and the ecosystem. Among others, a Raman lidar was brought to the Central Arctic for the first time, which delivered continuous and vertically high-resolved profiles of aerosol and water vapour. This dataset opens the possibility to analyse the vertical structure and the temporal evolution of water vapour over the Arctic sea ice. Continuous measurements of the vertical distributed water vapour were possible during the polar night in the Arctic winter.

This work evaluates the water vapour measurements from the Raman lidar PollyXT, that were conducted during the MOSAiC campaign (Engelmann et al., 2021). Although measurements below clouds are possible, this work focus on clear-sky cases in the time period between

25 October 2019 and 29 February 2020. Before the data can be analysed, they have to be processed and calibrated (Foth et al., 2015; Dai et al., 2018). After presenting the theoretical background to the instruments and the lidar data processing (Chapter 3), the first part of this work deals with the explanation of different calibration methods, their adaption to the very dry conditions in the Arctic and their application on the MOSAiC winter data (Chapter 4). The calibration results are compared to determine the method with the smallest uncertainty and assign a calibration constant for all evaluations (Sect. 4.3). The second part of this work comprises the analysis of calibrated WVMR profiles in Chapter 5 with the aim of examining three main research question. Firstly, the vertical structure, temporal development and amount of water vapour is considered in general in the Central Arctic winter to improve the knowledge about the general distribution and related processes. Secondly, the influence of the vertical distributed water vapour on the DLR is investigated at clear-sky conditions. Thirdly, the relation of the water vapour structures to the Arctic Oscillation and the synoptics is evaluated, since the atmospheric circulation has an impact on the water vapour distribution. Therefore two case studies are presented in Sect. 5.2, one from the negative and one from the positive phase of the Arctic Oscillation. The studies include a general description of the water vapour distribution, its influence on surface parameters like the DLR and the synoptics. The impact of the water vapour on the DLR is investigated in Sect. 5.3 for several cases. Statistical evaluations of many profiles of the chosen time period are conducted in Sect. 5.4 to draw conclusions about the vertical structure of water vapour in the Arctic winter and the relation to the atmospheric circulation. The main results of both parts, the calibration and the analyses, are finally concluded in Chapter 6.

Chapter 2

Meteorological conditions in the Arctic and the MOSAiC-campaign

2.1 Characteristics of the Arctic

2.1.1 The definition of the Arctic and the seasonal cycle of the Arctic climate system

Different definitions for the Arctic are used in studies dependent on their topics. Model studies often use the definition of an area north of a certain latitude, mostly 60° (e.g. Naakka et al. (2018)) or 70° N (e.g.Ghatak & Miller (2013); Screen & Simmonds (2010); Rinke et al. (2019)), and characterise the Arctic by averaged values over that domain. The net moisture transport into the Arctic is also often calculated at a latitudinal cycle at 60-70° N (Graversen et al., 2008; Nash et al., 2018; Naakka et al., 2019). Other studies define the Arctic as the region north of a certain air or sea temperature isotherm (e.g. Vázquez et al. (2016)), which is especially usefull for biological or hydrological considerations. All those definitions enclose a large region with many different characteristics, so that averaged model results have to be separated from measurements or evaluations at a specific location. The data of the MOSAiC campaign (cf. Sect. 2.3), which are used in this work, are point measurements, that were collected north of 85° during the winter 2019/20. The results from these measurements are only partly comparable to averaged model results.

Independent of the exact definition, the Arctic is the area around the North Pole, which is characterised by the Arctic Ocean surrounded by land. The circulation in the Arctic Ocean is connected to the Pacific and the Atlantic through the Bering and Fram Strait (Timmermans & Marshall, 2020). Large parts of the Arctic Ocean are covered by sea ice, which is an important part of the Arctic climate system. The sea ice drifts with the transpolar drift from the source regions north of Siberia over the North Pole area towards the Fram Strait (Krumpen et al., 2019). The Arctic climate shows a strong seasonal cycle between the summer with polar day and the winter with polar night. The sea ice concentration is lowest after the summer melting in September and highest at the end of the winter. The mean air temperatures and integrated water vapour (IWV) fluctuates between their maximum in the summer month and their minimum at the end of February or beginning of March (Rinke et al., 2021). The temperatures reach values between slightly above 0 and $-40\,^{\circ}\mathrm{C}$ and the IWV reaches values between 1 and up to 25-30 $\mathrm{kg\,m^{-2}}$ in peaks (Rinke et al., 2021). The Arctic winter is characterised by very cold surface surface temperatures and very low values of IWV of below $5\,\mathrm{kg\,m^{-2}}$. The atmospheric parameters are strongly influenced by the sea ice and the Arctic Ocean below. The structure of the atmosphere over sea ice is described in detail in Persson & Vihma (2017). The Arctic is warming faster than the rest of the globe (Wendisch et al., 2017), leading to fundamental changes in the Arctic climate system, like the sea ice concentration (Perovich et al., 2019), the transpolar drift (Krumpen et al., 2019) or the atmospheric circulation and the moisture transport (Rinke et al., 2019; Nygård et al., 2020).

2.1.2 The Atmospheric circulation in the Arctic

The mean circulation in the Arctic was described by Serreze & Barry (2014) for all seasons and different heights using NCEO/NCAR data from 1970-1999. They found three main pressure systems, that influence the Arctic during wintertime: a High over Siberia, the Icelandic Low and the Aleutian Low in the North Pacific. The Arctic Ocean is then influenced by relatively high pressure. In a height of 500 hPa, they found an asymmetrical Low over the Arctic with its pressure minimum over the Canadian Archielago. The stratosphere in 30 hPa is characterised by a strong, cold and symmetric polar vortex, that is surrounded by westerlies in the middle and upper stratosphere (Serreze & Barry, 2014). These circulation pattern are a long-term mean and the actual circulation differs due to the interannual and regional variability.

The large-scale atmospheric circulation in the Arctic can be expressed by the Arctic Oscillation (AO) (Thompson & Wallace, 1998), which is quantified by the AO index. The AO index is defined as the projection of the daily 1000 hPa height anomalies at 00 UTC on the loading pattern of the AO. The loading pattern of the AO is determined by the leading mode of the Empirical Orthogonal Function (EOF) analysis of the monthly mean 1000 hPa height during the period from 1979-2000 [1]. The resulting AO indices are positive or negative values in the order of magnitude of 10^0.

The Arctic Oscillation index represents the strength of the stratospheric polar vortex and its influence on the surface pressure (Serreze & Barry, 2014). A positive phase of the AO is characterised by a strong polar vortex, surrounded by a strong jetstream leading to a weak meridional transport into the Arctic. In contrast, during the negative phase of the AO, the polar vortex is weak or distorted with a strong meandering jetstream, leading to larger meridional transport. This meridional transport, which often brings warm and moist air into the Arctic, has an influence on the amount of water vapour in the Arctic and potentially also on its vertical structures.

2.2 Water vapour in the Arctic

2.2.1 The atmospheric water budget and moisture transport

The amount of atmospheric water vapour shows a strong seasonal cycle in the Arctic. Rinke et al. (2019) evaluated monthly mean values of the IWV from four different models averaged over 1979-2016 and found minimum values in January and February with a mean IWV of about 2.2 mm and maximum values in July with an IWV up to 14 mm. Beside, the IWV differs regionally for the ice-covered Arctic Ocean, the continents and open ocean areas.

The atmospheric water vapour budget of the Arctic is mainly controlled by local sinks and sources and by transport processes (Nash et al., 2018). A local source is evaporation, while local sinks are precipitation and cloud and ice formation. Horizontal transport processes of water vapour as well as trends in the moisture transport were considered in many studies (Vázquez et al., 2016; Nash et al., 2018; Naakka et al., 2019; Rinke et al., 2019; Nygård et al., 2019,

---

[1] `https://www.cpc.ncep.noaa.gov/products/precip/CWlink/daily_ao_index/ao.shtml`, 15-07-2022

2020). Vázquez et al. (2016) found four major sources for water vapour throughout the year with the Atlantic and the Pacific Oceans as main sources during winter and the landmasses North America and Siberia as dominant sources during summer. Beside, they could show the influence of each source on a specific region, which is mainly the area northeast of the source. Nygård et al. investigated the regional moistening pattern in the Arctic and found interactions between the moisture transport, surface evaporation and total column water vapour. They concluded that the moistening pattern in the Arctic is mainly due to moisture transport and that evaporation only plays a larger role in the marginal ice zone. Moreover, there are some interactions between both. Large evaporation can strengthen the horizontal transport, whereas large horizontal transport can suppress evaporation. As MOSAiC took place in the Arctic ice, moisture transport would be expected as the main source of atmospheric moisture, but at the specific location and on short time scales local evaporation could also have an impact.

New insights about the influence of evaporation over sea ice were also found from the SHEBA campaign, which are presented in Uttal et al. (2002) and Andreas et al. (2002). Andreas et al. showed, that the near-surface relative humidity is always near or even slightly above saturation with respect to ice, by evaluating different measurements of relative humidity in several heights and with multiple sensors. With the help of a simple model of the moisture content in the atmospheric boundary layer, they found open leads and polynyas as reason for the saturated air near the surface.

2.2.2 The impact of water vapour on the radiation budget

The amount of water vapour in the atmosphere influences the energy budget at the surface and in the atmosphere. Water vapour impacts the surface energy budget in two ways (Shupe et al., 2022). On the one hand, vertical fluxes of latent heat play a role. On the other hand, the vertical distributed water vapour in the atmosphere contributes to the downward longwave radiation at the surface. In the Arctic winter, the longwave radiation is an essential source in the surface radiation budget due to the absence of sunlight (Shupe et al., 2022). The largest changes in the downward longwave radiation are induced by clouds, leading to a warming of the surface. In contrast, the surface is cooling during clear-sky periods (Shupe et al., 2022), showing the direct impact of the radiation budget on the surface temperatures. Doyle et al. (2011) and others showed, that the atmospheric water vapour is influencing the downward longwave radiation during clear-sky conditions, for example the advection of large amounts of water vapour increases the DLR.

Ghatak & Miller (2013) evaluated monthly mean values of precipitable water (PW) and DLR from two different reanalysis models (ERA-interim and JRA 25) for the time period between 1979 and 2011. They presented a positive feedback loop between temperature, PW and DLR, meaning that all three variables change in the same direction. For simplicity they used PW as a measure for the water vapour in the atmosphere, but they stated the importance of the vertical distribution. One result of Ghatak & Miller (2013) was the non-linear correlation between DLR and PW, which is shown in Fig. 2.1. In principle, large amounts of water vapour are correlated with large DLR, which can be seen for the values from summer. In contrast, lower values of PW are observed during winter, which correlate with a lower DLR. The lower values of DLR show a much higher sensitivity on changes of PW than the higher values in summer. That means, that the advection of humidity layers has a huge influence on the DLR during wintertime.

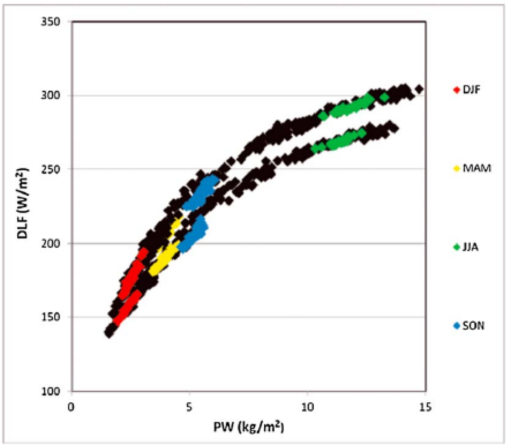

Figure 2.1: Relationship of downward longwave flux (DLF) and precipitable water (PW) based on the reanalyses ERA-interim (top curve) and JRA 25 (bottom curve) from 1979 to 2011. The black diamonds represent monthly data, the coloured diamonds show seasonal means for winter (DJF, red), spring (MAM, yellow), summer (JJA, green) and autumn (SON, blue) (Ghatak & Miller, 2013).

2.3 The MOSAiC-campaign

2.3.1 The campaign

The **M**ultidisciplinary drifting **O**bservatory for the **S**tudy of **Ar**cti**c** **C**limate (MOSAiC) expedition (Shupe et al., 2020, 2022) was an international research campaign in the Central Arctic with the goal of measuring the coupled Arctic processes continuously during a whole year. Therefore, the German icebreaker Polarstern was frozen in the ice in October 2019 north of Siberia and drifting with the transpolar drift close to the North Pole until it reached the Fram Strait end of July 2020. This was earlier than expected, so that the Polarstern was steered back to the Central Arctic to study the onset of the freezing as last missing process of the yearly cycle until the campaign ended in October 2020. The ship was the basis of the campaign during the whole drift and home for scientists from many countries. Some of the large and complex instruments were installed directly on the ship. Around the ship, a research camp was build up on the ice, measuring many different parameters of the atmosphere, the ocean, the cryosphere and the biosphere. In greater distance of $\approx 50\,\mathrm{km}$, a distributed network was set up on the ice for regional surrounding measurements of the heterogeneous processes in an area as large as one model gridbox to understand sub-grid scale processes. The campaign delivered exceptional measurements of the complex Arctic climate system with the aim of understanding processes and improving climate models.

The Raman lidar from the Leibniz Institute for Tropospheric Research (TROPOS) was installed in the OCEANET container (Engelmann et al., 2021), which was positioned on top of the D deck at the bow area of Polarstern. The container housed also two microwave radiometers, a sun and a lunar photometer, two distrometers and radiation measurement systems including a pyrgeometer. The pyrgeometer, which will be used for this study, was positioned at the bow crane of Polarstern. The radiosonde launches took place on another deck of Polarstern, but at the same height as the lidar position, which is important for the application of the calibration of the water vapour mixing ratio profiles (WVMR) profiles described in Sect. 3.3.

2.3.2 Meteorological conditions and the Arctic Oscillation index between October 2019 and February 2020

Rinke et al. (2021) provide an overview over the development of different meteorological parameters during the MOSAiC campaign. With the help of a comparison to the climatology between 1979-2019, an estimation was done about the normality of that year. The mean sea level pressure was lower than the long-term mean between January and April with es-

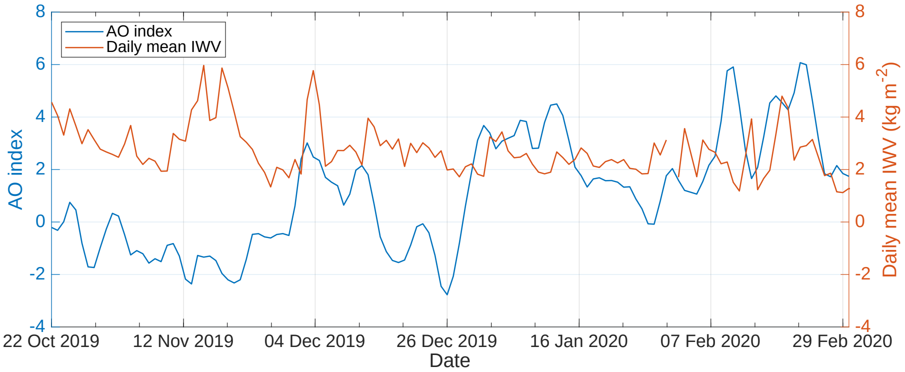

Figure 2.2: Time series of the AO index[2]and the measured daily mean integrated water vapour (IWV) from the microwave radiometer LHUMPRO (Walbröl et al., 2022) for the MOSAiC winter period from 25 Oct 2019 to 29 Feb 2020.

pecially large differences in February and March, when many cyclones occured. The coldest temperatures between October 2019 and January 2020 were higher during MOSAiC than in the climatological mean. The first half of November 2019 was embossed by anomalously cold temperatures, whereas it was warmer in the second half due to two cyclones between 16 and 20 November 2019. Rinke et al. (2021) found two more warming events during the winter between 3-5 December 2019 and 18-22 February 2020. All of these events were accompanied by anomalous high values of the IWV due to the intrusions of moisture and related increases of the downward longwave radiation. The number of cyclones was below the long-term mean for October 2019 to January 2020 and within the mean for February and March 2020. In contrast, the cyclone intensity and depth was higher than the average in February and March 2020.

The development of the AO index was unusual between late autumn 2019 and early spring 2020 (Rinke et al., 2021), because of a record-breaking strong positive phase of the AO from January to March (Lawrence et al., 2020). The time period of this study from 25 Oct 2019 to 29 Feb 2020 can be divided into three parts regarding the AO. October and November 2019 were embossed by a negative phase of the AO, followed by a transition phase from 01 to 29 December 2019 and a strong positive phase from 30 December 2019 until April 2020 (Fig. 2.2). The AO index is shown in Fig. 2.2 for the studied time period from 25 Oct 2019 to 29 Feb 2020. The period can be divided in three parts, a negative phase of the AO in October and November, a transition phase from 01 to 29 December 2019 and a strong positive phase from 30 December 2019 until April 2020. Beside the AO index, Fig. 2.2 presents the temporal development of the IWV, that was measured by the microwave radiometer LHUMPRO onboard the Polarstern. The highest IWV values were measured during the reported warming events in mid of November, beginning of December and mid of February, although the latter maximum reached a slightly smaller maximum IWV compared to the two in November and December. Hence, a larger variability and larger maximum values of the IWV are seen during the negative phase of the AO in comparison with the positive phase, but no direct correlation of the IWV values to the AO index can be observed.

---

[2] `https://ftp.cpc.ncep.noaa.gov/cwlinks/` (31.05.2021)

Chapter 3

Theory: Instrumentation and Methods

The following chapter presents the methods, which were used in this study to derive calibrated profiles of the WVMR from the measurements of the Raman lidar PollyXT during MOSAiC. The four instruments, which are used for the calibration and the different evaluations are presented in Sect. 3.1. The processing of the lidar data and the determination of WVMR profiles is explained in Sect. 3.2. The WVMR profiles from the Raman lidar measurements have to be calibrated. Three methods are presented to determine the calibration constant by comparison of the lidar measurements with the measurements of a reference instrument (Sect. 3.3). The calculation of WVMR profiles from the lidar measurements and the determination of the calibration constant was done with an own matlab program according to the presented methods in this chapter. Some of the basic calculations were adopted from an earlier program, which was used for the calibration of PollyXT measurements of the WVMR by (Dai et al., 2018).

3.1 Instrumentation

3.1.1 The Raman lidar

A lidar (**li**ght **d**etection **a**nd **r**anging) is an active remote-sensing instrument for the distance-resolved measurement of atmospheric quantities. It measures vertical profiles of the backscatter and extinction properties of particles in the atmosphere. The measurements are done continuously and vertically high-resolved and can be used for a better understanding of particular processes as well as for long-term observations. The basic principle of a lidar is as follows. First, pulsed radiation with a selected wavelength is emitted by a laser and scattered at particles and molecules in the atmosphere. A small part of the scattered radiation is scattered back at 180° to the instrument, received by a telescope and seperated into different channels by a receiver optics. From the time t between sending and receiving the signal and the speed of light c, the distance z of the scattering particles and molecules can be calculated as (Weitkamp, 2006):

$$z = 0.5 \cdot t \cdot \mathrm{c}. \tag{3.1}$$

The use of different wavelengths supports the lidars sensitivity for different sizes of particles. As the used laser light is polarized, the received radiation can be seperated in perpendicular and parallel polarized radiation giving information about the shape of the scattering particles. For this work, the data of the PollyXT lidar *Arielle* are used, which was installed in the OCEANET container during MOSAiC (Engelmann et al., 2021). All instrument specifics are described in (Engelmann et al., 2016). The PollyXT is a multiwavelength Raman and polarization lidar emitting radiation with the three wavelength 355 nm, 532 nm and 1064 nm. Beside the particle backscattering coefficients at all three wavelengths, it allows the determination of the particle extinction coefficients and depolarization at 355 nm and 532 nm and the Raman backscattering at 387 nm and 407 nm. Moreover, it includes five near-range channels at 355, 387, 532 and 607 nm wavelength and at 532 nm cross polarized. The resolution of the raw data of the PollyXT amounts to 30 s temporally and 7.47 m vertically. The first measurement height is 3.75 m above the instrument, given from the data acquisition system.

The Raman lidar technique allows the detection of the inelastic scattering of the molecules of water vapour (at $\lambda_{\mathrm{H_2O}} = 407\,\mathrm{nm}$) and nitrogen (at $\lambda_{\mathrm{N_2}} = 387\,\mathrm{nm}$) from a transmitted laser wavelength of 355 nm. Profiles of the WVMR can directly be derived from the Raman backscattering at these wavelengths (Melfi et al., 1969; Whiteman, 2003b; Wandinger, 2005). The basic principle of the inelastic scattering is the frequency shift of the scattered radiation due to changes of the vibrational and rotational states of the molecules during the scattering processes, which are characteristic for each molecule. That means the wavelength of the scattered radiation λ_{R} differs from the wavelength of the emitted radiation λ_0. The underlying processes are explained in detail in Wandinger (2005). The scattering cross section for Raman scattering is very low compared to the elastic scattering cross section, so that only a few photons are scattered back to the receiver optics. It is challenging to separate these low signals from the background light, especially during daytime. For that reason, Raman lidars are mainly used at nighttime. For the application in the Arctic winter, the background light is no limitation as it is completely dark during the polar night.

Before using the measured data for further calculations and analyses, several corrections have to be performed (Weitkamp, 2006). The received signal P_{R} consists not only of the signal of the backscattered photons P_{sig}, but includes instrumental noise and signals from the background light from the sky P_{bg}:

$$P_{\mathrm{R}} = P_{\mathrm{sig}} + P_{\mathrm{bg}}. \tag{3.2}$$

Thus, the data have to be background-corrected to derive the particle backscattering, which can be done by two different approaches. The background signal is either calculated as the mean over the signals of a height range at large altitudes or as the mean over the signals from about 12.5 μs (250 bins) before the laser pulse. For PollyXT, the background is calculated as the mean over the first 250 bins in the data, which represent the background before the emitted laser pulse (pretrigger), as the first measurement bin after the laser-pulse emission is the bin 254. The scattering processes at most particles in the atmosphere generate spherical waves, but the telescope area covers only a small part of such a sphere. This fraction gets smaller with increasing distance z between the scattering volume and the telescope. To correct this distance-dependence, the signal is usually range-corrected by multiplying it with z^2. At closer distances between the lidar and the scattering volumes, the overlap between the laser and the telescope field of view is not complete, so that the signals from those heights have to be corrected for the overlap.

The measured signals of a Raman lidar can then be expressed by the Raman lidar equation including all the corrections named above:

$$P_{\mathrm{R}}(z) = \frac{\mathrm{K_R} O(z)}{z^2} \beta_{\mathrm{R}}(z) \left(\exp - \int_0^z \left[\alpha_{\lambda_0}(\xi) + \alpha_{\lambda_{\mathrm{R}}}(\xi) \right] \mathrm{d}\xi \right), \tag{3.3}$$

where $O(z)$ is the overlap function, $\mathrm{K_R}$ is a system constant, which comprises all range-indepent system parameters, e.g. telescope area, receiver transmission and detection efficiency. $\beta_{\mathrm{R}}(z)$ is the Raman backscattering coefficient and α_{λ_0} and $\alpha_{\lambda_{\mathrm{R}}}$ express the extinction of light on the way between lidar and the backscattering volume before and after the scattering process (Wandinger, 2005). The Raman backscattering coefficient $\beta_{\mathrm{R}}(z)$ results from the product of the molecular number density of the Raman-active gas $N_\mathrm{R}(z)$ and the differential cross section for the backward direction $\mathrm{d}\sigma(\pi)/\,\mathrm{d}\Omega$ (Wandinger, 2005):

$$\beta_\mathrm{R}(z) = N_\mathrm{R}(z)\frac{\mathrm{d}\sigma(\pi)}{\mathrm{d}\Omega}. \tag{3.4}$$

The measured lidar signals $P_\mathrm{R}(z)$ are counted photons, that follow a Poisson distribution. Hence, the statistical error of each signal $P_\mathrm{R}(z)$ is given by $\sqrt{P_\mathrm{R}(z)}$ (Wandinger, 2005). According to this error and the composition of the total signal (Eq. 3.2), the signal-to-noise ratio (SNR) $S(z)$ can be calculated for each measured signal to get a quantity for the data quality of the measurement (Heese et al., 2010):

$$S(z) = \frac{P_\mathrm{sig}(z)}{\sqrt{P_\mathrm{sig}(z) + 2P_\mathrm{bg}}}. \tag{3.5}$$

$P_\mathrm{sig}(z)$ is the background-corrected signal for each height and P_bg is the background signal. Both signals have the unit counts. If the signals of the backscattered photons are too small compared to the background, the data are noisy and the SNR becomes small. A simple method to assure the data quality of the lidar profiles and to exclude noisy data is to define a threshold of the SNR and to use only signals for evaluations with a higher SNR than that threshold. To minimize noise and to increase the SNR, the lidar signals are smoothed temporally and/or vertically by calculating the sum over several lidar signals. A small disadvantage of every smoothing is the decline of the resolution of the data, but for the purpose of higher data quality. To calculate the SNR of the smoothed profiles, the background signals have to be smoothed in the same manner as the signals. According to Eq. 3.5, summing up several single signals increases the resulting signal P_sig much more than the small background P_bg, so that the SNR increases. In the following study the signals of water vapour and nitrogen molecules will be used. Only the SNR of the water vapour signal will be considered for the quality assurance, since the Raman scattering of nitrogen is much higher than the Raman scattering of water vapour, due to the atmospheric abundance of the respective molecules.

3.1.2 The radiosonde

A radiosonde (RS) measures profiles of the basic atmospheric parameters such as temperature, relative humidity, pressure and wind. The vertical resolution of the profiles is very high with measurements every several meters. In contrast, the temporal resolution is limited to four soundings per day, but which are regularly provided during the whole MOSAiC campaign. During MOSAiC, radiosondes of the type Vaisala RS41 were used with relative measurement errors of maximum 0.1% in temperature and 4% in relative humidity (Survo et al., 2014). These are combined uncertainties including sensor errors and sounding uncertainties. This means for example the uncertainty in relative humidity is the maximum error for very low temperatures. The very accurate measurements make the radiosonde highly suitable for the calibration of other instruments measuring vertical profiles or vertical integrated variables. Examples are the calibration of the microwave radiometer measurements or the lidar measurements of water vapour. When using radiosonde profiles for calibration two characteristics of the radiosonde measurements have to be considered. The most important feature is the drift of the radiosonde with the wind field, leading to a shift of the profile into different airmasses, depending on wind speed and stratification. Another feature is the time shift of the profile with height, because the rising of the radiosonde takes a certain time. As for the calibration of water vapour mainly the lowest part of the troposphere is relevant, this shift is negligible. To conclude, the uncertainties given above should be used for evaluating the measurement errors in temperature and relative humidity and the drift of the radiosonde with the wind has to be considered. The radiosonde data from the MOSAiC campaign, that were used in this study are provided on Pangaea by Maturilli et al. (2021).

3.1.3 The Microwave Radiometer

The microwave radiometer (MWR) is a passive remote-sensing instrument, which measures the brightness temperature of the atmosphere at specific frequencies (Janssen, 1994). The emission of water vapour or trace gases like oxygen, are detected and profiles of temperature and absolute humidity and the vertically integrated water vapour (IWV) and liquid water path (LWP) are estimated. A big advantage of microwave radiometers is their ability to continuous measurements during all weather conditions except rain. Moreover, it is not sensitive to the thermal radiation of ice, but on that from liquid water, allowing the measurement of liquid water and water vapour only. During MOSAiC, two microwave radiometers were installed on the OCEANET container next to the lidar, allowing direct comparisons of the measurements. The microwave radiometer HATPRO (Humidity And Temperature PROfiler) has 7 channels in the water vapour absorption band between $22-31\,\mathrm{GHz}$ for humidity profiling and 7 channels in the oxygen absorption band between $51-58\,\mathrm{GHz}$ for temperature profiling (Rose et al., 2005). Main products of HATPRO are the integrated water vapour (IWV) and the liquid water path (LWP). The measurements of HATPRO from the MOSAiC campaign are published in Ebell et al. (2022). The second microwave radiometer LHUMPRO (or passive Microwave Radiometer for Arctic Clouds (MiRAC-P), Mech et al. (2019)) combines millimeter and submillimeter channels. It contains 6 channels centered around the strong water vapour line at 183.31 GHz and two window channels at 243 and 340 GHz (Mech et al., 2019). The high frequencies of the LHUMPRO are especially suitable for low amounts of water vapour. The instrument delivers IWV, LWP and humidity profiles. The measurements of LHUMPRO from the MOSAiC campaign are published in Walbröl et al. (2022).
Only the IWV (I) will be used in this study. The uncertainty of the measured IWV from the two MWR is given in their data files. In the case of HATPRO an absolute error is given in each data file for the different elevation angles. This absolute error is $\Delta I_{\mathrm{HATPRO}} = 0.37\,\mathrm{kg\,m^{-2}}$ for the used elevation angle of 90°. For the MWR LHUMPRO, the absolute error of the IWV is given in the data file to $\Delta I_{\mathrm{LHUMPRO}} = 0.07\,\mathrm{kg\,m^{-2}}$ for values of the IWV below $5\,\mathrm{kg\,m^{-2}}$. By averaging the MWR data over 5 minutes, this error can be reduced to an absolute error around 0.02-0.03 $\mathrm{kg\,m^{-2}}$ for HATPRO and $0.0042\,\mathrm{kg\,m^{-2}}$ for LHUMPRO (cf. Eq. **??**). According to Walbröl et al. (2021), the measurement uncertainty of HATPRO increase for low values of IWV, which appear frequently during the Arctic winter. The IWV of LHUMPRO showed a much better agreement with the IWV calculated from radiosonde profiles, than the IWV of HATPRO during winter time (Walbröl et al., 2021). As the following study is limited to the Arctic winter and due to the much smaller uncertainties in the IWV from LHUMPRO, the LHUMPRO was chosen for calibration and comparisons of the IWV.

3.1.4 The pyrgeometer

A pyrgeometer measures the up- or downwelling broadband longwave radiation. In this study, the downward longwave radiation (DLR) will be used, which was measured at the bow crane of the Polarstern. The instrument was part of the 'Scalable automatic weather station' (SCAWS), supervised by TROPOS. The data have a resolution of 1 second and the measurements were done continuously. The uncertainty of the instrument is negligible and can be given to 0.41%, which was deviated from the calibration of the instrument in Lindenberg. To proof a possible influence of the ship on the data, the data of one cloud-free case, namely the 13 November 2019, were compared with the radiation measurements of the ARM-site on the ice [1]. The comparison showed differences of $2 - 3\,\mathrm{W\,m^{-2}}$, which should be in mind.

As a pyrgeometer measures the broadband longwave radiation, the Stefan-Boltzmann-law can be used for conclusions about the temperature of the radiation source in a first approximation. The Stefan-Boltzmann-law expresses the broadband longwave radiation of a black body with the temperature T into the total half space (Kraus, 2007):

$$\pi F_{\mathrm{LW}} = \sigma T^4, \tag{3.6}$$

with $\sigma = 5.67 \cdot 10^{-8}\,\mathrm{W\,m^{-2}\,K^{-1}}$. In that case, the temperature T is the radiation temperature of the sky T_{rad} and can be calculated from the measured longwave radiation F_{LW} as:

$$T_{\mathrm{rad}} = \sqrt[4]{\frac{\pi F_{\mathrm{LW}}}{\sigma}}. \tag{3.7}$$

3.2 Lidar data processing

3.2.1 Determination of the water vapour mixing ratio

Two Raman signals are used for the determination of the water vapour mixing ratio (WVMR): the backscattered signal from the water vapour molecules at the wavelength of 407 nm and the signal of the nitrogen molecules at 387 nm as the reference gas (Wandinger, 2005). In general, the WVMR ($w_{\mathrm{H_2O}}$) is defined as the ratio of the mass of water vapour ($m_{\mathrm{H_2O}}$) and the mass of dry air (m_{air}):

$$w_{\mathrm{H_2O}}(z) = \frac{m_{\mathrm{H_2O}}(z)}{m_{\mathrm{air}}(z)} = \frac{\rho_{\mathrm{H_2O}}(z)}{\rho_{\mathrm{air}}(z)} \propto \frac{N_{\mathrm{H_2O}}}{N_{\mathrm{N_2}}}, \tag{3.8}$$

where the mass can be expressed as the densities of water vapour ($\rho_{\mathrm{H_2O}}$) and dry air (ρ_{air}) respectively, considering the same volume. Furthermore the WVMR is proportional to the ratio of the molecular number densities of water vapour and nitrogen ($N_{\mathrm{H_2O}}$ and $N_{\mathrm{N_2}}$), which are correlated to the Raman backscattering coefficients as shown in Eq. 3.4. Combining Eq. 3.3, 3.4 and 3.8 delivers an equation for the height-resolved WVMR measured by the Raman lidar in $\mathrm{g\,kg^{-1}}$ (Whiteman, 2003b; Wandinger, 2005; Foth et al., 2015):

$$w_{\mathrm{H_2O}}(z) = \mathrm{C_{H_2O}} \cdot \frac{F_{\mathrm{N_2}}[T(z)]}{F_{\mathrm{H_2O}}[T(z)]} \cdot \frac{P_{\mathrm{H_2O}}(z)}{P_{\mathrm{N_2}}(z)} \cdot \frac{\exp\left[-\int_0^z \alpha_{\lambda_{\mathrm{N_2}}}\right]}{\exp\left[-\int_0^z \alpha_{\lambda_{\mathrm{H_2O}}}\right]}. \tag{3.9}$$

The four factors of this equation represent the calibration constant $\mathrm{C_{H_2O}}$, the temperature dependence of the filter transmission $R_{\mathrm{F}} = F_{\mathrm{N_2}}[T(z)]/F_{\mathrm{H_2O}}[T(z)]$ (Sect. 3.2.4), the ratio of the measured backscattered signals R_{w} for the two gases $\mathrm{H_2O}$ and $\mathrm{N_2}$ ($P_{\mathrm{H_2O}}(z)/P_{\mathrm{N_2}}(z)$), and a differential transmission term. The differential transmission term accounts for the different atmospheric transmission at the two used wavelengths $\lambda_{\mathrm{N_2}}$ and $\lambda_{\mathrm{H_2O}}$ and will be estimated in Sect. 3.2.3. The calibration constant $\mathrm{C_{H_2O}}$ can be determined by the use of a reference instrument, e.g. a radiosonde or a microwave radiometer, as it is further explained in Sect. 3.3.

---

[1] `https://dq.arm.gov/dq-zoom/?ds=mosiceradriihimakiS3.b1&variable=LWdn&sdate=20191113&edate=20191113&coordinate=`, 26-07-2022

The uncalibrated WVMR ($\mathrm{WVMR_{uncal}}$), which will be used later, is defined as follows:

$$w_{\mathrm{H_2O,uncal}}(z) = \frac{F_{\mathrm{N_2}}[T(z)]}{F_{\mathrm{H_2O}}[T(z)]} \cdot \frac{P_{\mathrm{H_2O}}(z)}{P_{\mathrm{N_2}}(z)} \cdot \frac{\exp\left[-\int_0^z \alpha_{\lambda_{\mathrm{N_2}}}\right]}{\exp\left[-\int_0^z \alpha_{\lambda_{\mathrm{H_2O}}}\right]}. \tag{3.10}$$

The exact processing of the lidar data to derive the uncalibrated WVMR is explained in the next section (Sect. 3.2.2). For the calculation of the WVMR, no range-correction of the measured Raman lidar signals is needed due to the used ratio, but the signals of each channel have to be background corrected. An overlap correction is omitted, assuming the same overlap for both channels (Foth et al., 2015).

3.2.2 Processing of the lidar signals from water vapour and nitrogen

Several processing steps are necessary to derive the signal profiles $P_{\mathrm{H_2O}}(z)$ and $P_{\mathrm{N_2}}(z)$, that can be used to calculate the uncalibrated WVMR (Eq. 3.10). The raw data from the Raman lidar contains profiles of the counted backscattered photons at different wavelengths. For *Arielle*, the raw signals of nitrogen at 387 nm are stored in channel 3 and those of water vapour at 407 nm are stored in channel 4. For photon-counting detection systems a so-called detector deadtime is responsible for a certain amount of non-counted photons at high count rates. This deadtime effect depends on the pulse width of the single photon signal of each detector in which no other photon can be counted and the measured lidar signals have to be corrected for this deadtime effect. For the deadtime correction, the raw signals have to be converted from counts to Mcps:

$$P[\mathrm{Mcps}] = \frac{P[\mathrm{counts}]}{B \cdot S_{\mathrm{m}}} \times 10^{-6}, \tag{3.11}$$

with the temporal resolution of the data acquisition B, which is 50 ns for the *Arielle*, and the measurement shots per dataset S_{m}, which are 600 shots for *Arielle*. The vertical resolution of the lidar measurements is determined by the temporal resolution of the data acquisition (50 ns) to be 7.5 m according to Eq. 3.1. The deadtime correction (Engelmann et al., 2016) is then done by a 5-order polynomial with the polynomial coefficients, that are stored in the data file. For further calculations the signals are converted back to counts, which is especially necessary for the later determination of the SNR.

The next step is the smoothing of both signals, the water vapour and the nitrogen signal, and their background signals. The temporal and vertical smoothing is performed by summing over several deadtime corrected signals in time and height. The temporal smoothing length is fixed in the program input and applied equally to all signals. For clear-sky cases, the vertical smoothing length is adapted to the SNR of the water vapour signal. The number of water vapour molecules in the atmosphere is decreasing with height, leading to a decreasing SNR. The decreasing SNR is reaching the SNR threshold faster in the Arctic due to very small signals, leading to lower height ranges of the profiles. To counteract this problem, the vertical smoothing is increased with height. Therefore several assumptions were made. The equation of the SNR (Eq. 3.5) is the basis of the consideration as it shows the relation between the SNR and the corrected signal. The equation was simplified by assuming the background P_{bg} to be zero. That can be done in a good approximation, because the background is very small in the Arctic due to the complete darkness during the polar night and the used detectors having dark counts of less than $100\,\mathrm{s}^{-1}$. The signal P_{sig} is then replaced by the sum of n vertically consecutive signals $P_{\mathrm{sum},n}$ and for the SNR a specified threshold $\mathrm{SNR_{th}}$ (S_{th}) is taken. The resulting criterion is:

$$P_{\mathrm{sum},n} \geq (S_{\mathrm{th}})^2, \tag{3.12}$$

which have to be fulfilled in each height. The minimum smoothing length is $n = 3$ bins ($\approx 22.5\,\mathrm{m}$) close to the ground, starting at the second height bin. The smoothing length is kept constant with increasing height as long the criterion is fulfilled, otherwise n is increased until the criterion is reached. The maximum smoothing length was usually defined to be 101 bins, corresponding to around 750 m, but can be adapted in the program input. This criterion is only applied to the water vapour signals, because they are much smaller than the nitrogen signals and reach the threshold of the SNR at lower heights. The advantage of the enlarging smoothing length is, that the height range of the profile is increased, but the higher vertical resolution is kept near the surface, where the SNR of the water vapour signals is larger. The resulting lower vertical resolution in greater heights is limited by the maximum smoothing length.
After determining the vertical smoothing lengths in dependence of the SNR of the water vapour signals, the same smoothing lengths are applied to the corresponding nitrogen signals and the background signals of both channels. Then, the SNR of both channels is calculated with Eq. 3.5. This approach is not applicable to cloudy cases, were the upper limit of the profiles is determined by high backscattering of the clouds. In that case, a larger vertical smoothing length can not increase the upper limit of the profiles significantly and is strongly influenced by multiscattering in the cloud-region. For that reason, the vertical smoothing length is fixed to one value over all heights in cloudy cases. After the temporal and vertical smoothing of the signals and their corresponding background signals, each signal is corrected for its background noise.
The uncalibrated WVMR (Eq. 3.10) can now be calculated from the smoothed signals, the filter transmission (Sect. 3.2.4) and the differential transmission term (Sect. 3.2.3). To assure the data quality, some criteria has to be fulfilled for each height: the SNR of the water vapour signal has to be greater than the threshold, the WVMR has to be greater than zero and smaller than infinity. Data that not fulfill these criteria are set to NaN. The resulting uncalibrated profiles of the WVMR are mean profiles with different maximum heights due to the SNR's of each profile. They can be used for the calculation of the calibration constant. The calibrated profiles are then used for analyses of the atmosphere.
In dependence of the further use of the WVMR profiles, mean profiles are determined by either calculating one mean profile over a fixed time period or several smoothed profiles over a longer time period. If one single profile is needed, as for the calibration with radiosonde or the analysis of specific cases, one mean profile is calculated over a time period with a defined start and end time. If a time series of WVMR profiles is needed, as for example for the calibration with IWV or analyses of the temporal development, temporal smoothed profiles are calculated for every time step of the original lidar data (30 s). Therefore, the temporal smoothing is realized by summing over several time steps centered around each time step. The vertical smoothing is done centered around each height bin for both cases.

3.2.3 Calculation of the differential transmission

The last factor of Eq. 3.9 accounts for the differential transmission of the radiation at the two wavelengths $\lambda_{\mathrm{N_2}} = 387\,\mathrm{nm}$ and $\lambda_{\mathrm{H_2O}} = 407\,\mathrm{nm}$. It is expressed by:

$$\Delta T_{\mathrm{r}}(z) = \frac{\exp\left[-\int_0^z \alpha_{\lambda_{\mathrm{N_2}}}(\xi)\,\mathrm{d}\xi\right]}{\exp\left[-\int_0^z \alpha_{\lambda_{\mathrm{H_2O}}}(\xi)\,\mathrm{d}\xi\right]}, \tag{3.13}$$

with the extinction coefficients α_λ at the two wavelengths (Whiteman, 2003b; Wandinger, 2005). The atmospheric extinction coefficients consists of the molecular extinction $\alpha_\lambda^{\mathrm{m}}$ and the particle extinction $\alpha_\lambda^{\mathrm{p}}$ and both include the scattering and absorption of light:

$$\alpha_\lambda = \alpha_\lambda^{\mathrm{m}} + \alpha_\lambda^{\mathrm{p}}. \tag{3.14}$$

According to Whiteman (2003a), the molecular absorption is negligible at the used wavelength of 355 nm of the Nd:YAG laser, so that the molecular component of the atmospheric extinction can be expressed by the total volume scattering coefficient β^{m} of Rayleigh scattering:

$$\alpha_\lambda = \beta^{\mathrm{m}}_\lambda + \alpha^{\mathrm{p}}_\lambda. \tag{3.15}$$

The total Rayleigh volume scattering coefficient β^{m} $[\mathrm{cm}^{-1}\,\mathrm{sr}^{-1}]$ can be calculated from the molecular number density N and the total Rayleigh scattering cross section σ^{m} (Measures, 1984):

$$\beta^{\mathrm{m}}_\lambda(z) = \sigma^{\mathrm{m}} \cdot N(z) = \frac{8}{3}\pi \cdot \sigma^{\mathrm{m}}_\pi \cdot N(z), \tag{3.16}$$

which can be retrieved from the Rayleigh backscattering cross section σ^{m}_π. There are different possibilities to calculate the Rayleigh backscattering cross section. Whiteman (2003a) compared a complex solution, dependent on temperature, pressure and number density (Bucholtz, 1995) with a simpler numeric solution. This simpler solution is commonly used in lidar applications, but does not consider effects of the dispersion of depolarization (Whiteman, 2003a). They found, that the result of the numeric equation is $\approx 3\%$ smaller than that from the full calculation at the wavelength of 355 nm. The difference gets smaller at higher wavelengths.
Here, the numeric solution is used in the calibration procedure (Measures, 1984; Whiteman, 2003a):

$$\sigma^{\mathrm{m}}_\pi = 5.45 \left[\frac{550}{\lambda}\right] \times 10^{-28}\,\mathrm{cm}^2\,\mathrm{sr}^{-1}, \tag{3.17}$$

with the wavelength λ in nm. The total Rayleigh volume scattering coefficient for each height is calculated by inserting the result of Eg. 3.17 in Eq. 3.16.
The molecular number density N is proportional to the air density and decreases in the same manner with height. The decrease of the air density with height can be expressed by an exponential term including the scale height z_{s} of the atmosphere:

$$\rho(z) = \rho(z=0) \cdot exp\left(-\frac{z}{z_{\mathrm{s}}}\right). \tag{3.18}$$

It follows for the molecular number density:

$$N(z) = N(z=0) \cdot exp\left(-\frac{z}{z_{\mathrm{s}}}\right). \tag{3.19}$$

A scale height of 8.3 km is taken for the calculation, corresponding to the value at mean sea level at 15 °C. The molecular number density at mean sea level is $N(z=0) = 2.55 \times 10^{19}\,\mathrm{cm}^{-3}$.

The extinction coefficient due to particles $\alpha^{\mathrm{p}}_\lambda$ is dependent on the amount of particles in the atmosphere and can be retrieved from the lidar measurements at the emitted wavelength. The particle extinction at any wavelength λ_2 can be calculated from a known particle extinction at the wavelength λ_1 and a corresponding height-dependent Ångström coefficient $\mathring{\mathrm{A}}(z)$ with the following equation:

$$\frac{\alpha^{\mathrm{p}}_{\lambda_1}(z)}{\alpha^{\mathrm{p}}_{\lambda_2}(z)} = \left(\frac{\lambda_2}{\lambda_1}\right)^{\mathring{\mathrm{A}}(z)}. \tag{3.20}$$

Figure 3.1 illustrates the differential transmission due to molecular and particle extinction. The molecular extinction profiles were calculated with Eq. 3.16, using Eq. 3.17 and 3.19. The particle extinction coefficient was set to $10\,\mathrm{Mm}^{-1}$ at 355 nm for all heights, corresponding to an optical thickness of 0.1. Engelmann et al. (2021) and Ohneiser et al. (2021) report, that the

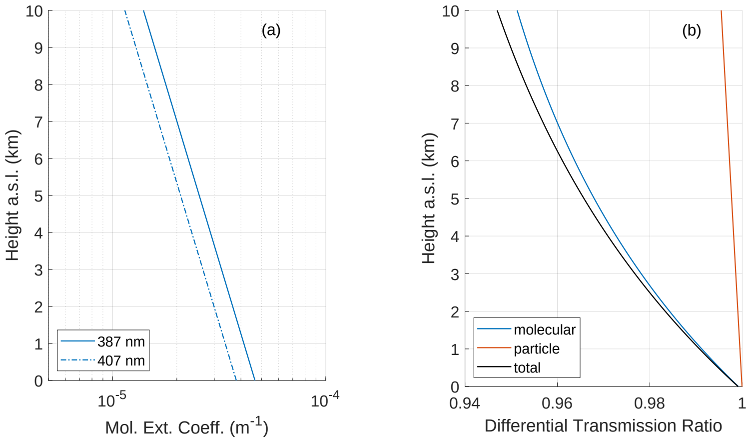

Figure 3.1: (a) Profiles of the molecular extinction coefficient at 387 and 407 nm. (b) Differential transmission due to pure molecular and particle extinction compared with the total differential transmission. The particle extinction coefficient was set to a constant value of 10 Mm^{-1} at 355 nm and an Ångström coefficient of 1.0 was assumed to calculate the differential transmission due to particles.

particle extinction can be higher close to the surface, but it is much smaller in large parts of the troposphere. Hence, assuming a constant particle extinction of 10 Mm^{-1} for all heights can be regarded as a maximum value. Assuming an Ångström coefficient of 1.0 leads to a particle extinction of 9.17 Mm^{-1} at 387 nm and 8.72 Mm^{-1} at 407 nm (Eq. 3.20). The differential transmission only due to particle extinction is then 0.9955 in 10 km height. That means, neglecting the particle extinction in the calculation of the total differential transmission results in an error of less than 0.5% in 10 km height and even less below. Engelmann et al. (2021) found a mean Ångström coefficient of 1.7 on 4 March 2020 during MOSAiC in Arctic haze, but even then the error in the differential transmission is smaller than 0.7%. Using a real extinction profile from 13 November 2019 at 16:40-16:50 UTC, the differential transmission due to particles is close to one for all heights, confirming that the air is very clean in the Arctic. All these calculations show, that the particle extinction can be neglected in the calculation of the differential transmission. Previous studies came to the same conclusion for different locations (Herold et al., 2011; Foth et al., 2015).

A second uncertainty in the differential transmission term results from the use of a simpler numeric equation for the calculation of the Rayleigh backscattering coefficient instead of the full Eq. 3.17. This error amounts to about 3% in each extinction coefficient for the used laser wavelength of 355 nm (Whiteman, 2003a). To consider its influence on the differential transmission, 3% higher values of the molecular extinction coefficient were taken and the differential transmission was calculated for the example shown in Fig. 3.1. The resulting differential transmission in 10 km height was 0.15% smaller than the one from the extinction coefficients from the numeric solution, which means, the numeric solution (Eq. 3.17) can be used without limitations and the error of the differential transmission term is negligible.

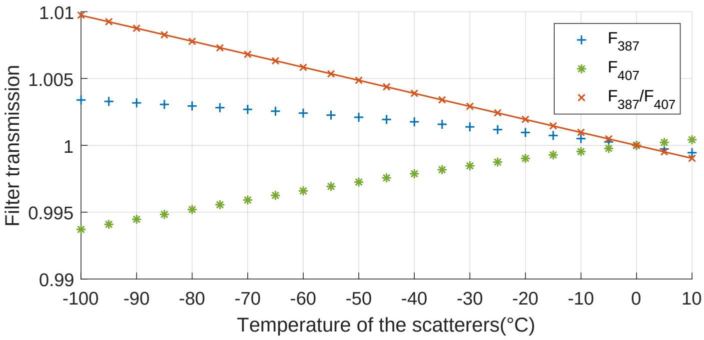

Figure 3.2: The transmission of the detected signals through the filters for nitrogen at 387 nm (F_{387}) and water vapour at 407 nm (F_{407}). Their ratio (F_{387}/F_{407}) is needed for the calculation of the WVMR. The temperature of the atmospheric scatterers determines the spectral properties of the backscattered radiation and thus its transmission through the filters.

3.2.4 Dependence of the signal ratio on the temperature of the atmospheric scatterers

The factors F_x in Eq. 3.9 include all the temperature-dependent variables (Whiteman, 2003a). The temperature dependence of the measurements is mainly determined by the temperature dependence of the rotational Raman scattering process in combination with the used filters and their properties (Whiteman, 2003b).

The intensity of the rotational Raman scattered radiation depends mainly on the specific molecule and on the wavelength of the incident radiation. The rotational Raman lines are distributed around a central wavelength for each molecule with different widths of the distribution. The used filters in the instrument need to have an appropriate transmission curve with a central wavelength and a full width at half maximum (FWHM) adapted to the rotational Raman spectrum of the observed molecules (Whiteman, 2003a). During MOSAiC, the filters for the nitrogen and water vapour channels were chosen to fulfil the requirements for the measurements of the backscattered light from the vibrational-rotational Raman transitions of the molecules. But it is to be regarded, that the intensities of the Raman lines are slightly different at different temperatures of the scatterers. The temperature dependent Raman spectrum is calculated and in combination with the transmission curves of the filters the total transmission of the detected signals through the filters was derived (*courtesy of R. Engelmann (TROPOS)*). Figure 3.2 shows the change of the total transmission of the signal with temperature for the nitrogen (F_{387}) and water vapour (F_{407}) molecules. The total transmission of the nitrogen signal changes by 0.34% between 0 and $-100\,°\mathrm{C}$, whereas the change amounts to 0.63% in the water vapour channel. The temperature dependent ratio R_F of the transmissions of these two channels is needed in the calculation of the WVMR (Eq. 3.9) and shown in orange in Fig. 3.2. It changes by only +0.97% between 0 and $-100\,°\mathrm{C}$ with the highest influence for very low temperatures. The temperature dependent total transmission of the signal through the filter is included in the calculation and no error of the ratio R_F is considered. The required temperature profile is taken from the nearest radiosonde.

3.2.5 Determination of the integrated water vapour

The integrated water vapour (IWV) is defined as the integral over the water vapour density $\rho_{\mathrm{H_2O}}(z)$ [$\mathrm{g\,m^{-3}}$], which can be expressed by the product of the water vapour mixing ratio $w_{\mathrm{H_2O}}$

$[\mathrm{g\,kg^{-1}}]$ and the density of dry air ρ_d $[\mathrm{kg\,m^{-3}}]$ (Elgered et al., 1982; Dai et al., 2018):

$$I_\mathrm{lidar} = \int_{z_\mathrm{min}}^{z_\mathrm{max}} \rho_\mathrm{H_2O}(z)\,\mathrm{d}z = \int_{z_\mathrm{min}}^{z_\mathrm{max}} w_\mathrm{H_2O}(z)\rho_\mathrm{d}(z)\,\mathrm{d}z \tag{3.21}$$

The resulting unit of the IWV is $\mathrm{g\,m^{-2}}$. For the calibration of the lidar water vapour measurements, the uncalibrated WVMR (Eq. 3.10) is used to determine an uncalibrated IWV of the lidar $I_\mathrm{lidar,uncal}$. The profile of the air density can be calculated from the ideal gas law for dry air:

$$\rho_\mathrm{d}(z) = \frac{p_\mathrm{d}(z)}{\mathrm{R_d} \cdot T(z)}, \tag{3.22}$$

with the pressure of dry air p_d, the temperature T and the individual gas constant for dry air $\mathrm{R_d} = 287.06\,\mathrm{J\,kg^{-1}\,K^{-1}}$. The required profiles of temperature and pressure can be taken from either another instrument, e.g. the radiosonde or the MWR, or from models like the Global Data Assimilation System (GDAS). In the following, radiosonde measurements are used. A problem is, that both, instruments and models, deliver only the pressure of moist air instead of the required partial pressure of dry air. An estimation shows the influence of water vapour on the total air pressure to be small, assuming a standard atmosphere and 100% relative humidity. In that case, the partial pressure of water vapour would amount to 1.7% of the total pressure at mean sea level and of less than 1% in 2 km height. Hence, the measured pressure of moist air can be used for the calculation of the density of dry air in a good approximation.

The integration range is chosen in dependence of the application. For comparison with the total IWV of the atmosphere from other instruments, the integration range should cover the whole atmosphere, but is limited by the increasing noise of the lidar data in greater heights. Especially in the Arctic with very low amounts of water vapour the maximum height range of the profiles is strongly limited. A great benefit of calculating the IWV from lidar profiles is the opportunity to determine the IWV of single layers.

3.2.6 Error analysis

According to Dai et al. (2018) and Whiteman (2003b), the relative error in the WVMR can be expressed by:

$$\frac{\sigma_w^2}{w^2}(z) = \frac{\sigma_\mathrm{C}^2}{\mathrm{C}^2} + \frac{\sigma_{R_\mathrm{F}}^2}{R_\mathrm{F}^2}(z) + \frac{\sigma_{R_\mathrm{w}}^2}{R_\mathrm{w}^2}(z) + \frac{\sigma_{\Delta T_\mathrm{r}}^2}{\Delta T_\mathrm{r}^2}(z), \tag{3.23}$$

where σ_x expresses the uncertainty of the quantity x. The uncertainties of the differential transmission term ΔT_r and the temperature dependence of the filter transmission R_F are negligible (Sect. 3.2.3 and 3.2.4). The uncertainty of the calibration constant σ_C will be considered in Sect. 3.3. This first term of Eq. 3.23 is left out in the estimation of an error of the uncalibrated WVMR.

The relative error of the signal ratio R_w results from the statistical error of the measured lidar signals. As explained in Sect. 3.1.1, the statistical error is determined by the Poisson statistics. Hence, the relative error of the signal ratio R_w can be calculated by use of the signal-to-noise ratio (SNR) (Dai et al., 2018):

$$\frac{\sigma_{R_\mathrm{w}}^2}{R_\mathrm{w}^2} = \frac{\sigma_{P_\mathrm{H_2O}(z)}^2}{P_\mathrm{H_2O}(z)^2} + \frac{\sigma_{P_\mathrm{N_2}(z)}^2}{P_\mathrm{N_2}(z)^2} = \frac{1}{S_\mathrm{H_2O}(z)^2} + \frac{1}{S_\mathrm{N_2}(z)^2}. \tag{3.24}$$

The error of the IWV from the lidar is determined by error propagation in the calculation of the IWV (Eq. 3.21). The uncertainty of the WVMR from the lidar is given in Eq. 3.23.

The uncertainty of the air density depends on the used instrument. When using the data from the radiosonde, several aspects have to be discussed. The measurement uncertainties of temperature and pressure are very small (cf. Sect. 3.1.2), leading to a negligible measurement uncertainty in the air density. Another small uncertainty occurs due to a possible time shift between the radiosonde launch and the lidar measurement. As the temperature changes over time are very small, this has a negligible influence. As the IWV from the lidar is numerically calculated by using a sum, the error of the IWV is calculated with the rules of error propagation as:

$$\Delta I_{\mathrm{lidar,uncal}} = \sqrt{\sum_z [\rho_\mathrm{d}(z) \cdot \sigma_{\mathrm{w_{uncal}}}(z)]^2}. \tag{3.25}$$

3.3 Calibration methods

A calibration is needed to derive profiles of the water vapour mixing ratio from the Raman lidar measurements. Therefore, water vapour measurements of a reference instrument are needed. In the following section, three methods will be compared. Two calibration methods using a radiosonde profile are explained in section 3.3.1 and the calibration method using the IWV will be shown in section 3.3.2.

3.3.1 Calibration with radiosonde

Radiosondes are often used instruments for the calibration of Raman lidar profiles as they are regularly provided and deliver accurate vertical profiles of water vapour. This method is described in literature in detail (e.g. Foth et al. (2015); Gerding et al. (2004); Herold et al. (2011); Melfi et al. (1969); Melfi & Whiteman (1985)).

In their paper about the automatical calibration of water vapour profiles from Raman lidar measured during the HOPE campaign (HD(CP)^2 Observational Prototype Experiment) in Jülich 2013, Foth et al. (2015) demonstrated two methods using radiosonde profiles: the regression and the profile method. For both methods, the WVMR profile of the radiosonde $w_{\mathrm{H_2O,RS}}$ is needed, which is calculated as

$$w_{\mathrm{H_2O,RS}} = 622 \cdot \frac{u_\mathrm{RS} \cdot e_\mathrm{sat}}{p_\mathrm{RS} - u_\mathrm{RS} \cdot e_\mathrm{sat}} \tag{3.26}$$

with the relative humidity of the radiosonde u_RS in %, the pressure of the radiosonde p_RS in Pa and the saturation pressure e_sat in hPa, which is calculated from the temperature of the RS.

The regression method is one calibration method using radiosonde profiles. Here, a linear regression is done between the WVMR measured by the radiosonde and the uncalibrated WVMR measured by the lidar. The calibration constant $\mathrm{C_{H_2O}}$ is determined by the slope of the regression line (Foth et al., 2015). Using this method, the measurement height of the data is not considered, so that small shifts in height between the two profiles may be compensated. As a quality check of the regression, the correlation coefficient R^2 can be used, which is larger for a better correlation between the two profiles. A large range of mixing ratios improves the correlation. To calculate an error of the calibration constant σ_C, the standard error of the slope of the regression line is used (Foth et al., 2015).

The other possible method is the profile method, where a calibration constant is calculated for each height:

$$\mathrm{C_{H_2O}}(z) = \frac{w_{\mathrm{H_2O,RS}}(z)}{w_{\mathrm{H_2O,uncal}}(z)}, \tag{3.27}$$

from the WVMR of the radiosonde $w_{\mathrm{H_2O,RS}}$ and the uncalibrated WVMR of the lidar $w_{\mathrm{H_2O,uncal}}$ (Eq. 3.10). The resulting calibration constant is the mean over all calibration constants of a specified height range. The standard deviation σ_{C} can be used as a measure for the uncertainty of the calibration constant (Foth et al., 2015). In this study, the standard deviation is used as the error of the calibration constant from the profile method, which is not directly comparable to the error of the calibration constant from the linear fit method.

It is essential for both methods to choose a height range, where the profiles of RS and lidar fit together. The minimum height should be chosen in dependence of the possible influence of surface structures or instrument setups. The maximum height depends on the drift of the radiosonde and its ascending time, which leads to differences between the lidar and the radiosonde profiles. In general, the profile method helps to determine height ranges, where the profiles of lidar and radiosonde fit best, because the determined height dependent calibration constants represents the relation between the WVMR of the radiosonde and the lidar. The standard deviation of the mean calibration constant over a certain height range is a measure for the congruence of the two profiles in that height range.

The atmospheric conditions should be cloud-free due to the limitations of the lidar by clouds. The water vapour distribution should be stable around the calibration time to minimize the influence of the radiosonde drift.

3.3.2 Calibration with integrated water vapour

Another calibration method for the WVMR of the lidar is based on the IWV. Possible reference instruments are a microwave radiometer (Foth et al., 2015) or a sun photometer (Dai et al., 2018). The sun photometer measures direct sunlight and thus can not be used in the Arctic winter. The microwave radiometer measures continuously and independent from clouds. Only during periods of rain, i.e., when the dome of the instrument is wet, the data cannot be used. The advantage of the MWR compared to the radiosonde as reference instrument is its continuous measuring parallel and close to the lidar, which are aligned directly vertical.

The calibration constant $\mathrm{C_{H_2O}}$ can be calculated as the ratio of the IWV from the reference instrument I_{ref} and the IWV from the lidar I_{lidar} (Eq. 3.21) for each measurement time:

$$\mathrm{C_{H_2O}}(t) = \frac{I_{\mathrm{ref}}(t)}{I_{\mathrm{lidar}}(t)}. \tag{3.28}$$

The atmospheric conditions have to be cloud-free during calibration periods due to the lidar limitations by clouds. In addition, the lidar profiles should cover large height ranges to capture most of the water vapour in the atmospheric column. The temporal variability of the vertical distributed water vapour should be small and should match the temporal smoothing length. A stable vertical distribution of the WVMR over the calibration time period allows to treat the different measurements as samples of similar atmospheric conditions and to average over them. Hence, a mean calibration constant is determined from the single calibration constants of each measurement time in the respective time period (Foth et al., 2015).

The error of each single calibration constant $\Delta\mathrm{C_{H_2O,t}}$ results from error propagation of Eq. 3.28 as follows:

$$\left(\frac{\Delta\mathrm{C_{H_2O,t}}}{\mathrm{C_{H_2O,t}}}\right)^2 = \left(\frac{\Delta I_{\mathrm{ref}}}{I_{\mathrm{ref}}}\right)^2 + \left(\frac{\Delta I_{\mathrm{lidar,uncal}}}{I_{\mathrm{lidar,uncal}}}\right)^2. \tag{3.29}$$

The uncertainty of the measured IWV from the MWR is part of the data files and presented in section 3.1.3. The uncertainty of the IWV from the lidar is determined by error propagation in the calculation of the IWV from lidar as shown in Eq. 3.25. During the Arctic winter, the error of the lidar IWV is much higher than the measurement error of the MWR. Thus, the error of each single calibration constant is mainly determined by the high uncertainty of the lidar IWV. The resulting calibration constant is the mean over all single calibration constant of the respective time period. The error of a mean value over certain number of single values that contain an error each, is calculated by applying the rules of the error propagation on the calculation of the mean. Hence, the error of the mean calibration constant $\Delta \mathrm{C}_{\mathrm{H_2O}}$ is calculated from the errors of all single calibration constants $\Delta \mathrm{C}_{\mathrm{H_2O,t}}$ as:

$$\Delta \mathrm{C}_{\mathrm{H_2O}} = \frac{1}{N}\sqrt{\sum_{t=1}^{N} (\Delta \mathrm{C}_{\mathrm{H_2O,t}})^2}, \tag{3.30}$$

with the amount of measurements N. This means, that the error of each mean calibration constant depends on the instrumental errors and the length of the chosen calibration time period.

3.3.3 Determination of one calibration constant for the MOSAiC winter data

Independent of the method, a calibration is only possible during specific conditions, which means at specific times. In recent studies, different approaches are used to determine which calibration constant to use during the times between the calibrations. One approach is to use the last calculated calibration constant (Foth et al., 2015), which could lead to sudden changes or errors if one constant was anomalous. The other possibility is to calculate a mean over all determined calibration constants at one location, if the instrumental setup is stable. This constant is then applied to all measurements of the instrument in that location and on that setup (Dai et al., 2018). The second approach is applied to the MOSAiC winter data due to the deployed stable instrumental setup.

Chapter 4

Calibration results

The total amount of water vapour in the Arctic is very small. Thus, the theoretical methods for calibration (Sect. 3.3) and the parameters in the lidar data processing have to be adapted to those very dry conditions in order to determine the calibration constant for the MOSAiC winter data appropriately. The adapted technical criteria are explained in Sect. 4.1, including the concrete settings for the data processing, discussions about the influence of the different parameters and the choice of the calibration time periods. All three calibration methods are then applied to one case on 27 October 2019 (Sect. 4.2). Finally, 55 calibration cases were found and are presented between 22 October 2019 and 29 February 2020. The calibration results for all these cases with all three methods are discussed in Sect. 4.3 and a mean calibration constant for each method is calculated. Taking the uncertainties of the different methods into account, one final calibration constant is selected, which is used for the further analyses of water vapour profiles in Chapter 5.

4.1 Technical criteria for the determination of the calibration constants

4.1.1 Calibration with radiosonde

Consistent setups are required in the calculation of the lidar profiles and several criteria have to be set in the calibration procedures to determine reasonable and comparable calibration constants. For the calibration with radiosonde, lidar profiles are needed at the same time as the radiosonde launches. The mean lidar profiles are calculated according to the processing steps in Sect. 3.2.2. The temporal smoothing was set to 10 minutes around the radiosonde launch, because 10 minutes are a good compromise between increasing the SNR of the resulting profile and keeping the atmospheric variability. Moreover, the radiosondes reach heights of around 3 km in 10 minutes, which is the maximum height chosen for some of the calibrations. The vertical smoothing length is increasing with height dependent on the SNR of the water vapour signal. The threshold of the SNR was set to 5, corresponding to a maximum statistical error of the WVMR of around 20% in the largest heights of the profiles, but much lower errors close to the surface, where the calibration was done.

The calibration height range was chosen in dependence of different criteria for the linear fit and the profile method. The minimum height was always set to 0.1 km to reduce the influences from the ship. The maximum height was determined manually for each lidar profile dependent on the correlation coefficient R^2 of the linear fit and the standard deviation of the profile method. Practically, a large maximum height was chosen and then decreased until the following criteria were fulfilled. For the choice of reliable calibration constants from the linear fit method and the corresponding height range, a threshold of the correlation coefficient was fixed. The threshold was set to a minimum correlation coefficient of 0.9 for this study. Simultaneously, the standard deviation of the profile method was set to be below 10% that height range with some exceptions. For the profile method, only the standard deviation of its calibration constant was considered. Hence, a stronger limit was set of a standard deviation below 5% with some exceptions for cases with a standard deviation between 5 and 10%.

To evaluate the calibration results, the wind speed in the calibration height range and the ascending time of the radiosonde were considered. The ascending time of the radiosonde should not strongly exceed the averaging time of the lidar profiles of 10 minutes to reach the maximum calibration height. A smaller height range should be better for high wind speeds, because of an expected strong drift of the radiosonde, but an evaluation of the changing wind speed with height is difficult. From quicklooks of the wind speed profiles, no correlation between wind speed and calibration height range was apparently for the calibrations.

4.1.2 Calibration with integrated water vapour

Before using the IWV of the MWR LHUMPRO for calibration, it was compared to the IWV calculated from the radiosonde profiles to assure a good performance of the MWR. Figure 4.1 shows a very good correlation between the IWV of the two instruments for all chosen calibration times. Only a small bias towards higher values is visible in the IWV of the MWR. The shift is slightly higher than the absolute error of $0.07\,\mathrm{kg\,m^{-2}}$, which is given in the data file of the MWR, and thus should be in mind when evaluating the calibration results.

For the calibration with the IWV, continuous profiles of cloudfree periods are necessary. The lidar profiles were calculated according to the processing steps in Sect. 3.2.2. The temporal smoothing was set to 30 minutes centered around each measured profile to decrease the error in the IWV of the lidar, but still get one profile every 30 seconds. The vertical smoothing is increasing with height and determined by the threshold of the SNR, which was set to 5 in a first step, but increased to 10 if the criteria could not be reached, which are explained later in this section.

The IWV was then calculated by integrating over the maximum height range of the calculated WVMR profiles (cf. Sect. 3.2.5). This height range do not cover the whole atmosphere. Hence, that lidar IWV is not comparable to the IWV of the MWR and has to be corrected for the covered height. The height-correction can be done with the help of the closest radiosonde profile. The RS profile of the WVMR cover the whole atmosphere and can be used to calculate a total column IWV (I_{RS}) as well as a partial IWV ($I_{\mathrm{RS,part}}$) for the height range of the respective lidar profile. The ratio $A = I_{\mathrm{RS,part}}/I_{\mathrm{RS}}$ of those two values gives the fraction of the total IWV, that is covered by the lidar IWV. The IWV of the MWR is now multiplied with this fraction A to be comparable with the determined lidar IWV. The calibration constant is then calculated from the height-corrected IWV of the MWR and the determined IWV of the lidar profile. This correction is done for each timestep seperately, because the maximum height of each lidar profile is different as it depends on the SNR of the profiles. This correction is absolutely necessary due the data processing. Beside, the correction solves the problem of the uncomplete coverage of the atmospheric column by the lidar IWV in the Arctic, because of very low amounts of water vapour. On the other hand, a radiosonde profile is necessary for the calibration. The temporal shift between the radiosonde launch and the calibration period can lead to errors in the correction and thus in the determined calibration constant, but this error is small, if the

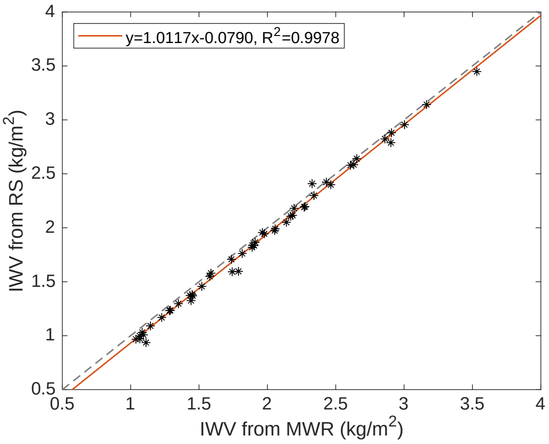

Figure 4.1: Correlation between the IWV measured by the MWR LHUMPRO and the radiosondes for 51 of the 55 calibration times with available MWR data.

lidar profile covers a high fraction of the total column water vapour.

Finally, two criteria are defined, which have to be fulfilled for every calibration constant. Firstly, the mean relative error of the IWV from the lidar over the chosen time period have to be minimal, but in any case smaller than 30%. Secondly, the coverage of the lidar IWV have to amount to more than 90% of the total atmospheric column IWV ($A \geq 0.9$). If the criteria could not be reached with 30 min temporal smoothing and a SNR threshold of 5, the SNR threshold was increased to 10. This increased threshold of the SNR leads to a stronger vertical smoothing and possibly to a lower height range of the profiles, but it reduces the statistical error in the WVMR and thus the error of the IWV. The lower height range of the profiles is corrected in the calculations and thus has a small influence. If the temporal smoothing would be increased instead, the lower resolution would lead to a loss of the covered atmospheric variability. Only for very stable distributions of the atmospheric water vapour, a temporal smoothing of 1 h would be reasonable. In contrast, a smoothing of 10 min is more appropriate for a high temporal atmospheric variability of water vapour, but then the second criterium could not be reached in most cases. The graphs of the IWV from lidar and MWR were compared for each calibration period to check their representation of the temporal variabilities. A measure for their congruence is the standard deviation of the mean calibration constant of that period, which is usually small.

4.1.3 Influence of the chosen threshold of the SNR

A threshold of the SNR of the water vapour signals was defined to assure the data quality. The relation between the maximum relative error of the WVMR and the minimum accepted SNR regarding the water vapour signal is given by Eq. 3.24. The SNR of the nitrogen signal is much higher than the SNR of the water vapour signal, due to much a greater amount of nitrogen molecules in the atmosphere, especially in the Arctic. Hence, the relative error of the WVMR is mainly determined by the SNR of the water vapour signal and the maximum relative error can be approximated by $1/\mathrm{SNR}_{\mathrm{th}}$. The SNR of the water vapour signal decreases with height due to the decreasing number of detected water vapour molecules. Hence, the relative error of the WVMR increases until its maximum in the height where the SNR has reached the defined threshold.

The errors of the WVMR's along the profile are influencing the error of the IWV from lidar (Eq. 3.25). A small threshold of the SNR leads to a high maximum relative error in the WVMR profile and thus to larger errors in the IWV. In contrast, a high threshold of the SNR leads to smaller height ranges of the profiles and thus an error in the IWV due to the uncomplete coverage of the atmospheric column. As the IWV of the lidar is corrected for the uncomplete atmospheric column in the calibration procedure, a higher SNR is preferred to reach smaller errors in the IWV. Beside, the SNR threshold influences the increasing range of the vertical smoothing and the height range covered by the profiles. A high SNR threshold leads to a stronger vertical smoothing and thus a lower resolution. As the vertical structure is crucial for the calibration with radiosonde, the vertical smoothing should be small in the calibration height range and the chosen threshold of the SNR should be not to large. For the determination of the IWV, the vertical resolution is not that important, so that the vertical smoothing and the SNR threshold could be larger. The resulting loss of vertical resolution is largest in the uppermost parts of the profiles, where the WVMR is usually very small and thus its influence on the IWV is small too. As a result of these considerations, the threshold of the SNR was set to 5 for the calibration with radiosonde and to 5 or 10 if necessary for the calibration with the IWV.

4.1.4 Choice of calibration time periods

The atmospheric conditions have to be cloudfree for all calibration methods and the vertical distribution of the water vapour should be stable during the calibration periods. The attenuated backscatter at 1064 nm was used to determine cloudfree periods. Cases with clouds above 6 km height were considered as cloud-free, because the calculated water vapour profiles have not reached that height and the contribution of the water vapour to the IWV is mostly negligible in that height (Foth et al., 2015). The temporal variability of the WVMR profiles should be in the order of the temporal smoothing length or lower to calculate reasonable mean profiles. A quicklook in the temporal development of the WVMR helped to determine cases with stable conditions around the radiosonde launch (calibration with radiosonde) or between the closest radiosonde launch and the calibration period (IWV method). The calibration with IWV is also possible between two radiosonde launches, but a radiosonde profile is needed for the height-correction of the lidar IWV. Therefore the closest radiosonde was chosen to minimize the error in the height-correction. A stable water vapour distribution is very important for those cases. Most calibration cases were chosen close to a radiosonde launch, so that calibration constants could be calculated with all methods.

4.2 Discussion of the calibration methods

The calibration procedures of the shown methods are discussed using the example of the 27 October 2019 in this section. The attenuated backscatter at 1064 nm shows clear-sky conditions between 00:00 and 13:30 UTC, so that two radiosondes are used for calibration on that day at 05:06 and 10:53 UTC. The shown example is the calibration with the radiosonde at 05:06 UTC.

An appropriate height range has to be determined for the calibration with radiosonde. A large height range between 0.1 and 3 km is chosen in a first step to calculate a preliminary calibration constant with the linear fit method. The WVMR profile of the lidar is then calibrated using this calibration constant and manually compared with the profile measured by the radiosonde. Figure 4.2a shows these profiles, but using the final calibration constant from the linear fit method of that case of $16.1117\,\mathrm{g\,kg^{-1}}$. A very good conformity of the profiles is visible until 2.5 km height, so that the calibration is repeated for that height range, resulting in a cali-

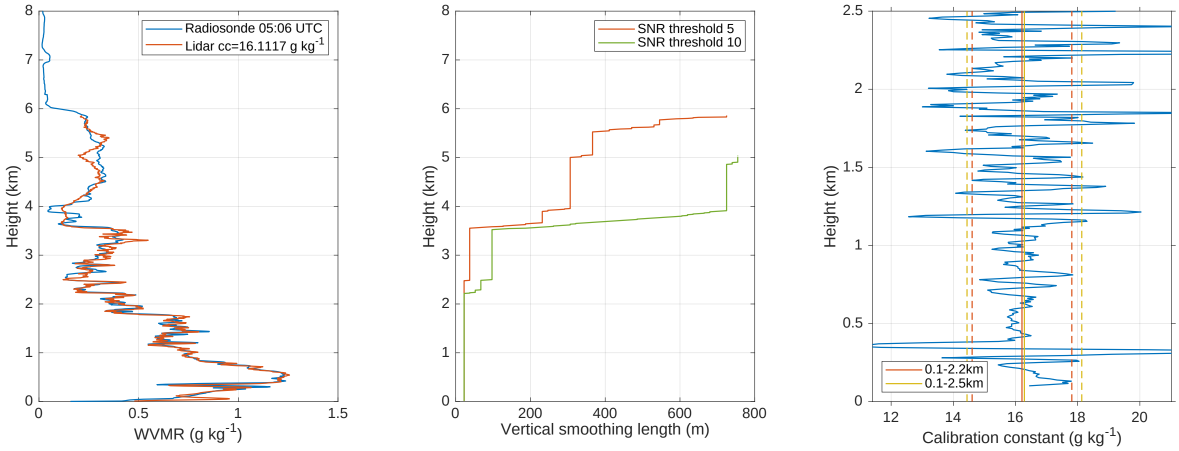

(a) WVMR profiles measured by the radiosonde and the lidar. The lidar profile was calibrated with $C_{H_2O} = 16.1117\,\mathrm{g\,kg^{-1}}$ determined with the linear fit method.

(b) Dependence of the vertical smoothing length of the lidar signals on the height for two different thresholds of the SNR of the water vapour signal.

(c) Calibration constants from the profile method. Vertical lines show the mean (straight) and standard deviation (dashed) of the calibration constants over the respective height ranges.

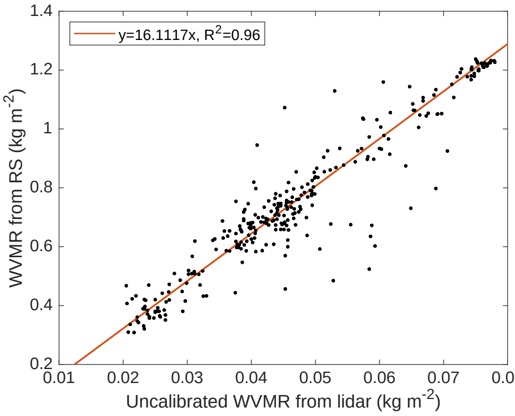

(d) Linear fit between the uncalibrated WVMR of the lidar and the WVMR of the RS between 0.1 and 2.2 km height. The slope of the regression line determines the calibration constant.

Figure 4.2: Calibration with radiosonde using an example case on 27 October 2019. The lidar profile was averaged between 05:00-05:10 UTC and the radiosonde was launched at 05:06 UTC.

bration constant of $16.1055 \pm 0.0551\,\mathrm{g\,kg^{-1}}$ with a correlation coefficient of $R^2 = 0.97$ for the linear fit. Parallel, the mean calibration constant from the profile method is determined to be $16.2861 \pm 1.8451\,\mathrm{g\,kg^{-1}}$ for that height range. The standard deviation of 11.3% was higher than the defined maximum 10% for the profile method, so that a smaller height range has to be chosen. It is chosen manually to $0.1 - 2.2\,\mathrm{km}$ by looking at the profile of calibration constants and their standard deviation in Fig. 4.2c. The mean calibration constant for that height range amounts to $16.2082 \pm 1.6029\,\mathrm{g\,kg^{-1}}$, which corresponds to a standard deviation of 9.9% and fulfill the criterion for the profile method. The calibration with the linear fit is repeated for that lower height range and results in a calibration constant of $16.1117 \pm 0.0577\,\mathrm{g\,kg^{-1}}$ with a

correlation coefficient of $R^2 = 0.96$. Those calibration constants are then taken for that case, because both criteria ($R^2 \geq 0.9$ and $\sigma_{\mathrm{C}} \leq 10\%$ for the profile method) are fulfilled.
It can be discussed, if it is better to choose a larger height range, where the correlation coefficient of the linear fit is higher or to choose a smaller height range, where the standard deviation of the profile method is below 10%. Both aspects are important and have to be balanced for each case. It can be seen from several cases, that a larger height range with a broader range of WVMR values increase the correlation of the linear fit, as long as the profiles do not diverge. In contrast, a smaller height range with a very good conformity is better for the profile method.
Figure 4.2b shows the vertical smoothing of the lidar profile for different thresholds of the SNR. As explained in Sect. 3.2.2, the vertical smoothing length increases with height depending on the SNR of the lidar water vapour signal. The example shows, that increasing the SNR threshold from 5 to 10 causes no difference in the vertical smoothing length below 2.2 km, slightly larger smoothing between 2.2 and 3.6 km and a strong increase above. That means, the SNR of the lidar signal is greater than 10 below 2.2 km height for the initial vertical smoothing over 22.5 m (3 bins). The found calibration height range matches this height and thus the calibration was done with the lowest vertical smoothing length of 22.5 m in that case. The smoothing length increase faster for a larger threshold of the SNR, corresponding to a higher quality demand on the WVMR profile, but also reaching the maximum smoothing length earlier and covering a lower height range. A stronger vertical smoothing is necessary for low amounts of water vapour or low quality of the lidar data, which is the case in larger heights, but depends also on the atmospheric conditions. For the calibration with radiosonde, the vertical smoothing should be small, as the vertical structure plays a huge role. The calibration height range begins close to the surface and thus covers the range of the smallest vertical smoothing and the highest data quality. The chosen threshold of the SNR usually plays a minor role in that height range.

For the calibration with IWV, the time period between 03:15 and 05:30 UTC was chosen, because of the relatively stable water vapour layering. The temporal development of the height-resolved WVMR during that timeperiod is shown in Fig. 4.3a. The vertical profiles are reaching a maximum height of nearly 6 km. A humid layer is visible below 1 km height, that is slowly shrinking with time. The changes occur slowly and thus allow the temporal smoothing of 30 minutes, which is necessary for the calculation of the IWV from the lidar profiles. The applied vertical smoothing lengths are plotted in Fig. 4.3b. The lowest smoothing length of 22.5 m matches the quality criterium up to a height of around 3.6 km and a medium smoothing is applied up to around 5.5 km. The WVMR measurements (Fig. 4.3a) above 3.6 km show very small values, leading to the enhanced smoothing. A possible influence of the changing smoothing length with height on the data could not be prooved, as the radiosonde drifts away from the lidar profile in greater heights, but it should be small due to the very low values of the WVMR in that height.
The uncalibrated IWV of the lidar was caclulated from each profile during that time period, corrected for the maximum height of the profiles and then used to determine calibration constants. The radiosonde at 05:06 UTC was used for the height-correction. Figure 4.4a shows the temporal developement of the calibrated and height-corrected IWV from the lidar compared with the IWV of the microwave radiometer LHUMPRO. Both instruments show a similar evolution, but there are also some differences. The lidar seems to react faster on changes and shows more small-scale variability, although the data were smoothed temporally over 30 minutes. On the other hand, the relative error of the lidar IWV is still high with a mean value of 23.27% over the shown time period due to very small amounts of water vapour in the Arctic. Such comparisons were done for every calibration time period to proof, if both instruments capture the atmospheric conditions similarly. Possible sources for differences are instrument-specific causes

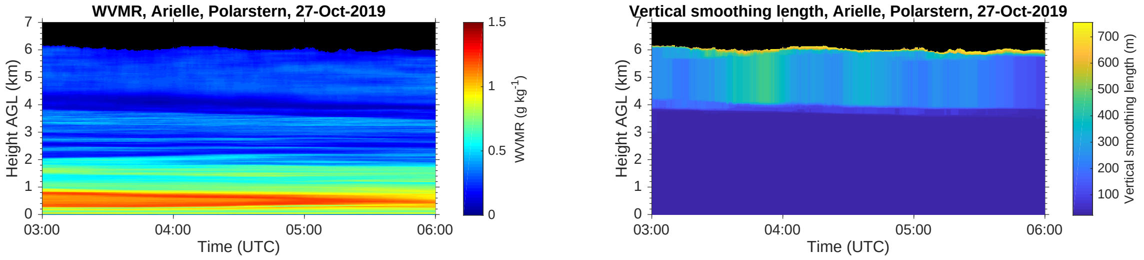

(a) Temporal development of the height-resolved WVMR measured by the lidar, calibrated with the final calibration constant of $C_{H_2O} = 15.96\,\mathrm{g\,kg^{-1}}$.

(b) The height-dependent vertical smoothing length of the lidar signals.

Figure 4.3: Example case on 27 October 2019 for the calibration with the IWV of a MWR: the time period of 03:15 to 05:30 UTC was chosen with a centered temporal smoothing over 30 minutes.

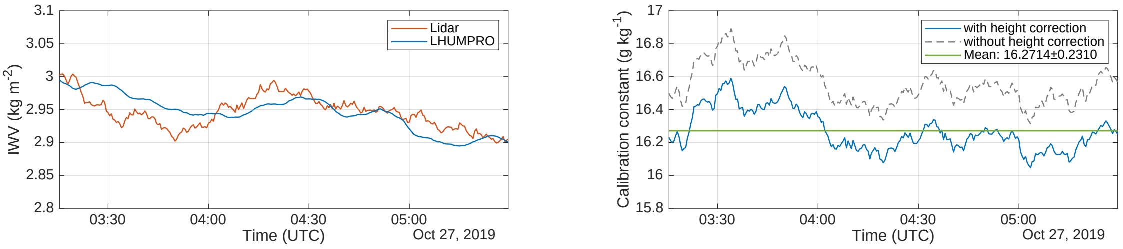

(a) The IWV of the lidar and the microwave radiometer LHUMPRO. The lidar IWV was calibrated with the mean calibration constant of that case of $C_{H_2O} = 16.2714\,\mathrm{g\,kg^{-1}}$ and corrected for the covered height range.

(b) The calibration constants determined with the IWV method (blue). The grey dashed line shows the calibration constants without applying the height correction due to the uncomplete lidar coverage.

Figure 4.4: Temporal development of the IWV and the calculated calibration constants in the calibration time period between 03:15 and 05:30 UTC on 27 October 2019.

like problems with the very dry conditions, slightly different observed atmospheric volumes or causes in the data processing like influences of the temporal smoothing. The small differences in the IWV of the two instruments are also reflected in the calculated calibration constants which are shown in Fig. 4.4b and leading to a mean calibration constant of $16.2714\,\mathrm{g\,kg^{-1}}$ and a standard deviation of $0.1233\,\mathrm{g\,kg^{-1}}$. Figure 4.4b also shows calibration constants, which were calculated without applying the height-correction on the IWV of the microwave radiometer. The resulting calibration constants are around $0.3\,\mathrm{g\,kg^{-1}}$ higher for that example, in spite of a very high vertical coverage of the lidar profile with 98.3% of the total IWV in average. Many other cases show a lower vertical coverage of the lidar profiles or strong changes in the maximum reached height, indicating the importance of that height-correction for a good calibration. The error calculation was done as explained in Sect. 3.3.2, leading to large uncertainties of each single calibration constant of around $\Delta C_{H_2O,t} = 3.786\,\mathrm{g\,kg^{-1}}$ in average, but to a much smaller final error of the mean calibration constant of $\Delta C_{H_2O} = 0.2310\,\mathrm{g\,kg^{-1}}$ due to error propagation. Thus the final constant from the IWV method is given to $C_{H_2O} = 16.2714 \pm 0.2310\,\mathrm{g\,kg^{-1}}$ for that case.

4.3 Determination of the final calibration constants

To deliver a final calibration constant, cloud-free and stable cases were chosen during the period 22 October 2019 to 29 February 2020. This measurement period starts at the earliest measurement time of the MWR LHUMPRO and includes all winter month. The first sunlight came back at the location of Polarstern around the 10 March 2020, so that some cases in the beginning of March may have been possible for calibration, but were not used here. In total, 55 cases were considered for calibration, but not for every case all methods delivered calibration constants using the criteria explained above. At the end, 49 calibration constants could be determined with the linear fit method, 45 with the profile method and 41 with the IWV method, which are shown in Fig. 4.5 and 4.6. The final calibration constant is a constant, which should only change, if the instrumental setup is changed. No such changes were done during the considered measurement period. Thus, all determined calibration constants were averaged for every method to retrieve one final constant for each method.
The two methods using the radiosonde profile deliver very similar mean calibration constants and standard deviations with $15.96 \pm 0.37\,\mathrm{g\,kg^{-1}}$ for the linear fit (Fig. 4.5a) and $16.01 \pm 0.35\,\mathrm{g\,kg^{-1}}$ for the profile method (Fig. 4.5b). In contrast, the error of each single constant is much higher for the profile method. Possible reasons are the different definitions of the errors for both methods (cf. Sect. 3.3.1) or the height dependence of the two methods. Possible shifts of vertical water vapour structures in the profiles of radiosonde and lidar due to the drift of the radiosonde play a large role in the height-dependent profile method, but are less important in the height-independent correlation of the linear fit.
The correlation between the constants of both methods itself is very good with a correlation coefficient of 0.9378 (Fig. 4.7) showing that both methods coincides, if the right height ranges are chosen. The used height ranges are shown in the bottom plots in Fig. 4.5 for the two methods, respectively. They are the same for many of the cases, but the height range for the profile method is smaller if necessary. The reason for that are the different requirements for a good calibration. While only a good conformity between lidar and radiosonde profile is important for the profile method, the range of the used WVMR values have to be large enough as well for the linear regression. Moreover, the bottom plot in Fig. 4.5a shows the correlation coefficient of the linear fit for each determined calibration constant. All correlation coefficients are greater than 0.9 as claimed by the calibration criteria, but it is visible, that larger correlation coeffients could be reached from October to mid of December, when the total amount of water vapour was higher. A higher total amount of water vapour leads to a greater range of WVMR values in the profile, which improves the correlation of the linear fit.

The calibration results of the IWV method are shown in Fig. 4.6. The mean calibration constant amounts to $16.36 \pm 0.36\,\mathrm{g\,kg^{-1}}$ and is 0.35 to $0.4\,\mathrm{g\,kg^{-1}}$ higher than the constants from the calibration with radiosonde. The standard deviation is similar to the other methods. Two calibration constants stand out with extraordinary high values, but they fulfill all the calibration criteria explained above. Thus, the IWV of the reference instrument, the MWR LHUMPRO, was compared to that derived from the radiosonde to evaluate the adequacy of the measurement periods used for calibration. The IWV of LHUMPRO was therefore averaged over the same 10 minutes around the corresponding radiosonde launch, which were used to calculate mean lidar profiles for the calibration with radiosonde. The IWV of both instruments could be calculated for 50 out of the 55 calibration cases due to missing data of the MWR and shifts between the calibration time period of the IWV method and the radiosonde launch. The determined values of the IWV are shown in Fig. 4.6b. In general, they are very well correlated, but looking at the relative difference between both, some values stand out. It could be determined, that the

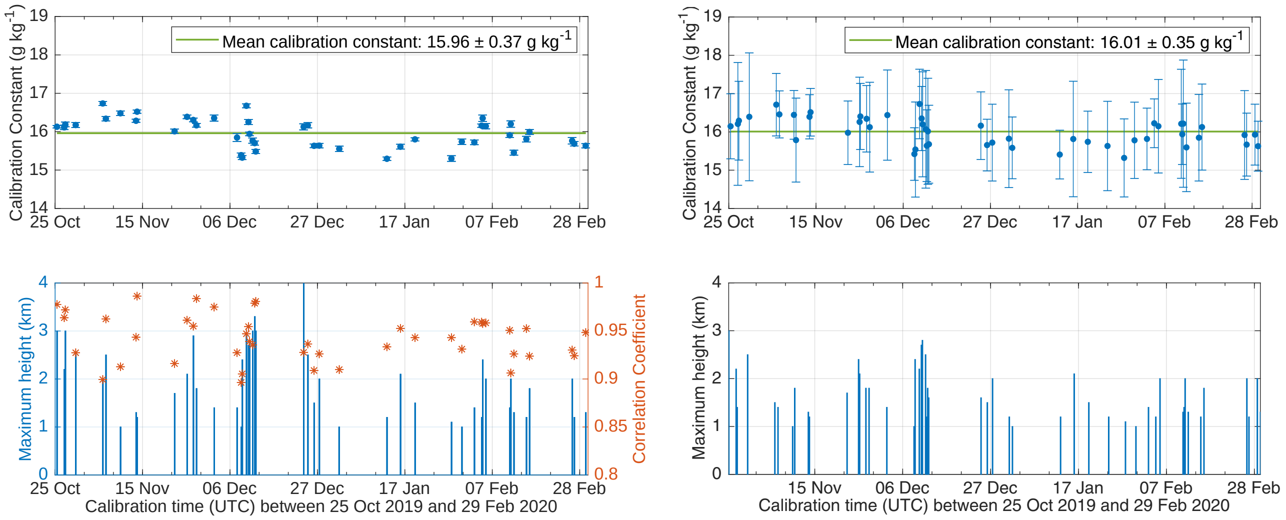

(a) Calibration results from the linear fit method: all determined calibration constants (top) were calculated from a height range between 0.1 km and a respective maximum height (bottom, bars), resulting in a mean of $15.96 \pm 0.37\,\mathrm{g\,kg^{-1}}$. The correlation coefficient of each determined constant is shown in orange (bottom).

(b) Calibration results from the profile method: all determined calibration constants (top) were calculated from a height range between 0.1 km and a respective maximum height (bottom), resulting in a mean of $16.01 \pm 0.35\,\mathrm{g\,kg^{-1}}$.

Figure 4.5: Results from the two calibration methods using radiosonde profiles.

calibration constants with the highest deviation from the mean correspond to the cases with the largest difference between the IWV from LHUMPRO I_{MWR} and the IWV of the radiosonde I_{RS}. This leads to an additional criterion for the choice of the calibration constants from IWV method. All constants with a relative difference larger than 10% between the I_{MWR} and the I_{RS} were excluded from the calculation of the mean calibration constant and are marked in red in Fig. 4.6a.

The resulting mean calibration constant is still 0.35 to $0.4\,\mathrm{g\,kg^{-1}}$ higher than the constants from the calibration with radiosonde. Moreover, the single calibration constants from the IWV method poorly correlate with those from the linear fit method as shown in in Fig. 4.7 (blue triangles). Beside the general shift of the IWV method towards greater calibration constants, they show a great spread. This leads to the conclusion, that the method is not very stable in the Arctic. Possible reasons for the differences could be the very small absolute amounts of water vapour in the Arctic atmosphere and associated problems of the instruments. Both, the lidar and the MWR are limited by very dry conditions. It could be seen, that the relative error of the IWV from the lidar is high with a defined limit of 30% for the calibration. Reducing this error is only possible by enlarging the temporal or vertical smoothing, which leads to a loss of information. Beside, the increasing smoothing with height could have an influence on the resulting IWV from the lidar, although the influence should be small (cf. Sect. 4.1.3). The large spread in the correlation of the calibration constants from different methods could be additionally influenced by a low stability in the calibration procedure. Many carefully selected, but still manually determined factors are influencing the calculation of each constant, which are the choice of proper cases, the different lengths of the calibration time periods, the threshold of the SNR and the changing quality of the data. In addition, the accuracy of the IWV from the MWR has an impact on the resulting calibration constant. The comparison with the radiosonde measurements showed a general overestimation of the IWV by around $0.08\,\mathrm{kg\,m^{-2}}$

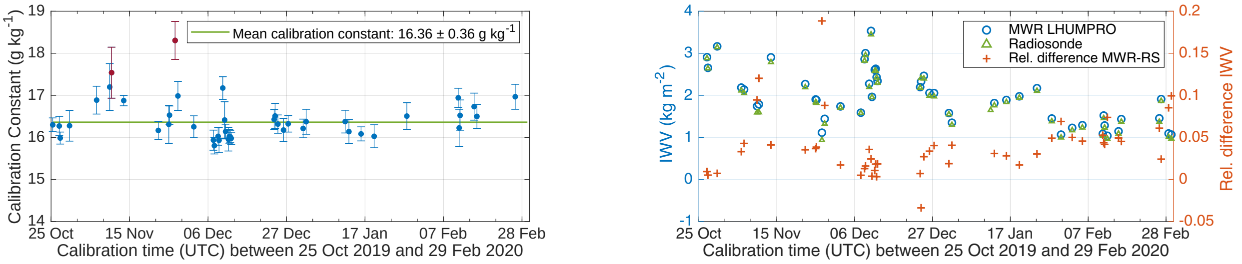

(a) Calibration constants from the IWV method.

(b) Comparison of the IWV from the MWR and the RS for the calibration times. The relative difference was calculated as $(I_{\mathrm{MWR}} - I_{\mathrm{RS}})/I_{\mathrm{RS}}$.

Figure 4.6: Results from the calibration with the IWV from the MWR LHUMPRO.

(Fig. 4.1), which contributes to higher calibration constants.

The values of the IWV help to evaluate the influence of the absolute amount of water vapour on the calibration and are shown in Fig. 4.6b. Cases with the highest IWV could be observed from October to the beginning of December, while the IWV was smaller in general afterwards due to colder temperatures. There is no clear correlation observable between the IWV and the deviation of the calibration constants from the mean. For the case with the highest IWV ($> 4\,\mathrm{kg\,m^{-2}}$), the calibration constants of all methods match the mean very well, but for most of the other cases, positive and negative deviations occur similarly. When looking at the cases with the smallest measured IWV ($< 1.2\,\mathrm{kg\,m^{-2}}$), the calibration constants from the radiosonde methods tend to be smaller than the mean, while the calibration constants from the IWV method are all larger then their mean. To summarize, there are small tendencies at very dry conditions for the different reference instruments, but in general no correlation between the deviation of the calibration constants from the mean and the IWV could be found.

To conclude, all shown calibration methods had to be adapted to the very dry conditions in the Arctic. In principle, all calibration procedures are reasonably working, but they have limitations at very low WVMR's. The comparison of the determined calibration constants showed a

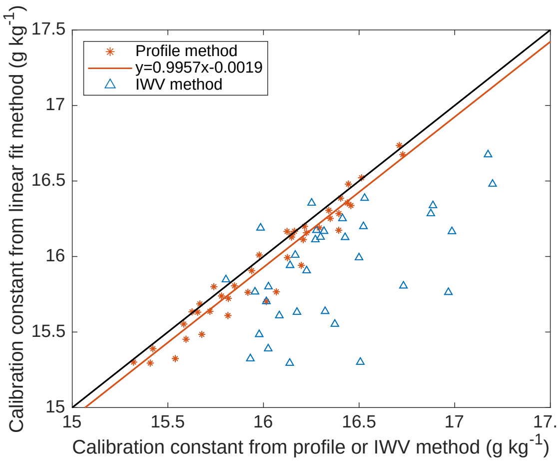

Figure 4.7: Correlation of the calibration constants determined by the linear fit method and the profile method (orange) and the linear fit and the IWV method (blue).

very good correlation between the two methods using radiosonde measurements. The most important factor for those calibrations is the determination of the height range. The determined errors of the single calibration constant are much lower for the linear fit method. In contrast, the IWV method delivered a higher mean calibration constant and a greater spread in the comparison with the linear fit method. The main reason for that is the large relative error in the IWV calculated from the lidar profiles of WVMR at the dry conditions in the Arctic, but also a small general overestimation of the IWV by the MWR LHUMPRO in comparison with the radiosonde. For that reason, the WVMR of the lidar should be calibrated with radiosonde profiles in the Arctic. The two radiosonde methods both deliver very good results, but the determined errors of the single calibration constants are smaller for the linear fit method. Furthermore the method is widely established and delivers stable results. For these reasons, it was chosen to use the calibration constant from the linear fit method as the final calibration constant. All further profiles of the WVMR are calibrated with that calibration constant of $15.96 \pm 0.37\,\mathrm{g\,kg^{-1}}$.

Chapter 5

Analysis of water vapour profiles

Profiles of the WVMR can be derived from the Raman lidar measurements according to Sect. 3.2 and calibrated with the determined calibration constant (Sect. 4.3). The period between 25 October 2019 and 29 February 2020 was chosen for the analyses in this chapter, because the water vapour measurements from the lidar are limited to polar night and the calibration was done for that time period. The vertically distributed water vapour in the Arctic is an important part of the Arctic climate system and influences for instance cloud formation and the longwave radiation fluxes. Possible sources are local sources, like evaporation or dissolving clouds, or the advection of water vapour from remote sources. Both, the vertical distribution and the sources of water vapour depend on the synoptic conditions, which are represented by the Arctic Oscillation in a first approximation. The following analyses aim to answer three main questions. Firstly, the vertical distribution of water vapour in the Central Arctic winter is considered in general. Secondly, the influence of the water vapour on the downward longwave radiation is evaluated (Sect. 5.3) and thirdly, a possible relation between the vertical structure of the water vapour and the AO is examined. There are two main methods to investigate those questions. Case studies deliver a very detailed view on single cases, whereas statistical analyses help to generalise conclusions. Two case studies are presented in Sect. 5.2 for a case with a negative and a case with a positive AO index. The correlation between the IWV and the DLR is combined for 7 selected cases in Sect. 5.3 and the influence of the temperature of the water vapour is evaluated. Many profiles, distributed over the whole time period, are analysed statistically in Sect. 5.4 regarding the amount of water vapour in different layers and the gradients in the WVMR. The applied methods to analyse the profiles are introduced in Sect. 5.1.

5.1 Methods to analyse profiles of the WVMR

There is a variety of options to evaluate the vertical profiles of WVMR from the lidar measurements. The lidar profiles are stored every 30 seconds and smoothed vertically and temporally according to the processing steps explained in Sect. 3.2.2. Two visualisations of the lidar measurements are used in this work. Colorplots are showing the temporal evolution of the vertical resolved WVMR. Mean profiles over 10 minutes are used to analyse the vertical structure in detail at a certain time. The data for the colorplot are smoothed temporally over 10 minutes. All shown data were calculated with a threshold of the SNR of 5 in the signal processing. The shown single profiles of the WVMR are smoothed vertically over 5 bins.

There are different possible parameters, which will be used to characterise each WVMR profile. Some of the following parameters are only possible with a coincident temperature profile, which is taken from the radiosonde. If their is no radiosounding at the time of the chosen lidar profile, the radiosonde data are linear interpolated over time. The simplest parameters to characterise the profiles are minimum, maximum and mean values the WVMR and the temperature profile. Another parameter is the IWV of the total profile, which represents the total amount of water vapour in the respective atmospheric column. The WVMR profiles can be divided into different layers to determine the IWV of humid layers and to get an overview over the layering without looking at each profile separately, which is especially important for the statistical analyses. The definition of layers was done according to the temperature or the WVMR profile and is explained in Sect. 5.1.1. The determination of one characteristic temperature for each profile is discussed in Sect. 5.1.3. Vertical gradients of the WVMR are calculated over specified vertical height ranges and analysed according to their strength and width in the WVMR (Sect. 5.1.2). Beside plotting the profile of the vertical gradients, all WVMR gradients of one selected profile are plotted in a histogram to analyse their frequency of occurrence. For all listed parameters, a specific height range has to be fixed for the analyses to get comparable results.

5.1.1 Definition of atmospheric layers

There are several possibilities to divide a profile of the WVMR into layers. The first possibility is to define layers separated by temperature inversions. Persson & Vihma (2017) defined the Arctic inversion at the height of the absolute maximum in the temperature profile. Usually, there is one dominating temperature inversion, but it could be seen, that there are several cases with more than one strong temperature inversion in the Arctic. Thus, all temperature inversions of a profile were determined by calculating all local maxima of the profile with a minimum prominence of 0.3 K (red circles in Fig. 5.1a). The prominence of a local temperature maximum in the profile is defined as follows: Firstly, a vertical line is drawn at the value of the local maximum. Secondly, the height of the next intersections of this vertical line with either the profile or the end of the plot is identified in both directions. Then, the local minima are determined in the height range between those intersections and the local maximum. Finally, the prominence of the local maximum is calculated as the temperature difference between the local maximum and the larger local minimum.

The inversion height is defined as the height of the local maximum in the temperature profile. To calculate the inversion strength, the local minimum between each two maxima is determined (blue circles in Fig. 5.1a). The temperature difference between the local maximum and the next minimum below is defined as the inversion strength. The determined inversion heights are then used to seperate the WVMR profile into layers, as shown in Fig. 5.1a. The inversion heights do not meet exactly the limits of the observed water vapour layers, but they are close to them and divide the profile reasonably. An advantage of using temperature inversions for the layer separation is a possible conclusion on airmasses and their limitations by the inversions. A disadvantage of using temperature profiles from the radiosonde is the small shift between the WVMR and the temperature profile due to the drift of the radiosonde and the time it needs for ascending.

The second possibility to define water vapour layers is to use the profile of the WVMR itself. Therefore the local minima of the WVMR profile were determined and their heights are used as layer boundaries. The minimum prominence of the local minima was defined as 10% of the absolute maximum of each WVMR profile to take the temporal variability in the total amount of water vapour into account. The determined heights of the local minima are marked in the profile in Fig. 5.1b. The lower two points meet the boundaries of the water vapour layers very well, but the upper point misses the top of the uppermost layer. The reason for the unexpected layer boundary in the height of the uppermost local minimum are strong vertical

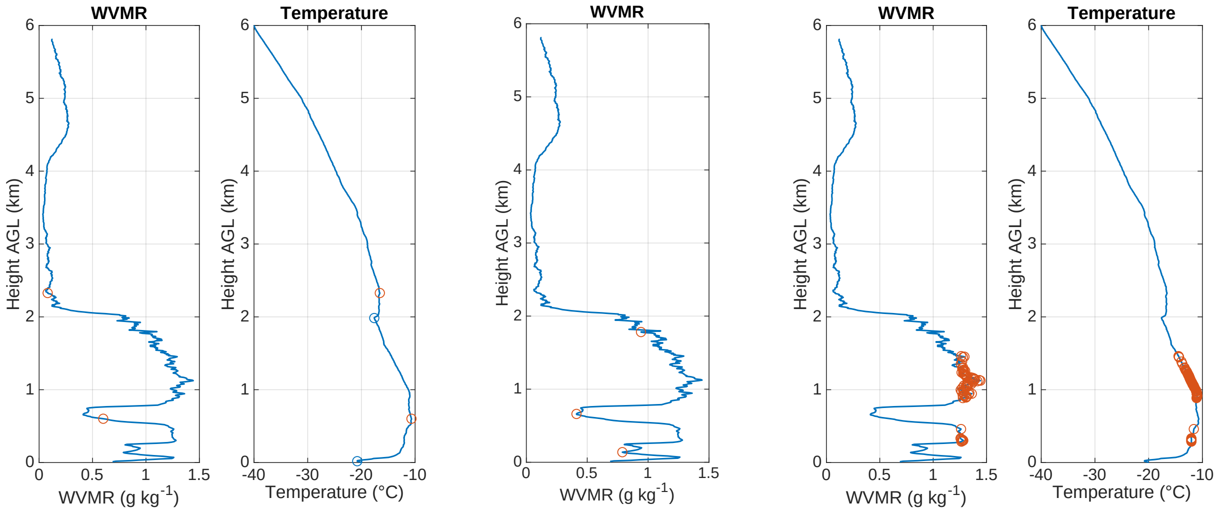

(a) Separation of the WVMR profile into layers limited by temperature inversions. The red circles mark the height of local maxima, the blue circles local minima in the temperature profile.

(b) Separation of the WVMR profile into layers between local minima in the WVMR (red circles).

(c) Determination of a mean temperature of the water vapour, its WVMR is larger than the 90. percentile of the WVMR profile between 100 m and 5 km height (red circles). The mean temperature of the marked heights amounts to −12.13 °C.

Figure 5.1: Methods to analyse WVMR profiles. The profiles show the mean WVMR profile from the 13 November 2019 19:50-20:00 UTC and the temperature profile at 19:55 UTC. Temperature profiles were measured by the radiosonde at 16:51 and 22:54 UTC and linear interpolated.

variations in the lidar signal due to the atmospheric variability or remaining noise. This is a limitation of the automatical division into layers, especially for cases with low WVMR values, but the example shows still a reasonable layer separation, that represents the main vertical water vapour distribution. The depth of each water vapour layer is calculated by determining the maximum between each two local minima. The layer depth is then the difference between the WVMR at the determined maximum and the WVMR at the larger neighbour minimum.

A third possibility is to use the vertical gradients of the WVMR profile. The calculation of the gradients is explained in Sect. 5.1.2. Heights with gradients and absolute differences in the WVMR larger than a defined limit mark the edges of the different layers. This method is not very robust for lidar profiles, because of the small-scale changes in the profile due to atmospheric variability or instrumental noise. Thus, it will not be used to separate the WVMR profile into layers. A possibility for an improvement could be a stronger smoothing of the lidar profiles and an adjustment of the limit for the gradients, but was not done in this study.

The IWV of the defined layers of a profile will be calculated for the first two methods to characterise the layers and the vertical structure. To get comparable results, the determined IWV of each layer will be weighted with the height of the layer and further called the layer IWV.

5.1.2 Analysis of gradients

Two methods are used to calculate vertical gradients of the WVMR. Firstly, the vertical gradients of the mean lidar profile are calculated over a fixed vertical range of 5 bins centered around each measurement bin. Beside plotting them as a profile, they are plotted in a histogram to consider their frequency distribution. For further analyses a normal distribution is fitted on the data to determine the mean μ_n and the standard deviation σ_n. The function for the normal distribution is:

$$f(x, \mu_\mathrm{n}, \sigma_\mathrm{n}) = \frac{1}{\sigma_\mathrm{n}\sqrt{2\pi}} \exp\left(\frac{-(x-\mu_\mathrm{n})^2}{2\sigma_\mathrm{n}^2}\right), \quad \text{for } x \in \mathbb{R}. \tag{5.1}$$

This function is scaled to a maximum of 1. Hence, the fitted function is multiplied with a scaling factor to adjust the function to the frequency distribution. The scaling factor is calculated by dividing the maximum of the frequency distribution through the maximum of the fitted normal distribution.

A second possibility is the calculation of gradients of specific layers. Therefore, the gradients are calculated over each bin in a first step and then the WVMR profile is seperated into segments with the same sign of the gradient. Segments with a length of just one bin are excluded and added to the neighbouring segments. In a second step the gradients and absolute differences in the WVMR are calculated for each of those segments and allocated to the top height of the segments. The resulting gradients are averaged values for the respective height range of the segments. Most of the resulting gradients are small and cover small ranges of WVMR. Thus, only gradients larger than a limit of $0.4\,\mathrm{g\,kg^{-1}}$ per $100\,\mathrm{m}$ are evaluated for a more focused analysis. Beside, a limit for a minimum absolute difference in the WVMR was set for a definition of water vapour layers. A limit of 20% of the maximum WVMR in the respective profile was found to be appropriate to take the temporal variability of the maximum WVMR into account.

5.1.3 Determination of a characteristic temperature

For analyses of the relation between the vertical distributed water vapour and the downward longwave radiation, it has become necessary to determine one characteristic temperature for each profile. The simplest solution would be to use the surface temperature or the absolute maximum temperature of the profile, but they do not represent the temperature of the water vapour, which emits the longwave radiation. The measured longwave radiation is the total downward longwave radiation from the sky, that means from all the different components, from all directions and from all heights. In this study only the influence of the water vapour is investigated. The water vapour is vertically distributed and has different temperatures in different heights. For the following investigations, the temperature at the height of the largest amounts of water vapour is used to get a temperature, that represents the water vapour as a source for the downward longwave radiation. To avoid the uncertainty of a single value in the lidar profile, that still contains some noise and atmospheric variability, the mean temperature of a height is used. Therefore, the 90. percentile of all WVMR values between 100 m and 5 km is calculated. Then, the heights of all WVMR values are determined, which are larger than this 90. percentile. These are the heights, that contain the largest amounts of water vapour and represent the largest contribution to the downward longwave radiation of the water vapour in the atmosphere. A mean temperature is calculated from the temperatures in these heights, that is used as the characteristic temperature of the water vapour profile when estimating its influence on the downward longwave radiation. This mean temperature is further called the mean temperature from the 90. percentile of the WVMR or simply the 90. percentile temperature. Beside, a mean WVMR is calculated from these heights, further called the mean WVMR of the 90. percentile. Figure 5.1c) shows the determined heights for the example of the 13 Nov 2019 19:50-20:00 UTC. The 90. percentile of the WVMR profile amounts to $1.2545\,\mathrm{g\,kg^{-1}}$ for that example. The calculated mean WVMR and temperature from the marked heights are $1.3075\,\mathrm{g\,kg^{-1}}$ and $-12.13\,°\mathrm{C}$, respectively. The determined height ranges cover the highest WVMR values, which are located in more than one layer. The calculated mean temperature of the height range is lower than the maximum temperature, but it represents the mean temperature of the heights with the largest WVMR. Using a lower percentile as limit, for example the 80. percentile, would lead to a larger temperature range and lower mean temperatures. The limit of the 90. percentile was chosen, because the smaller height range of the 90. percentile ensures, that the determined mean temperature is closer to the real temperatures of the water vapour in that heights.

5.2 Case studies

Case studies deliver detailed insights into specific events or processes and are used to illustrate answers to the three research questions: Firstly, the vertical distribution of water vapour in the Arctic and possible sinks and sources in different heights are analysed in general. Secondly, the relation between the vertical resolved WVMR and the downward longwave radiation is considered for specific cases. Thirdly, a relation to the Arctic Oscillation index is studied by choosing cases from the positive and the negative phase of the Arctic Oscillation. The results from the case studies are not comprehensive enough for a robust conclusion about a correlation between the AO index and parameters of the WVMR profiles, but they deliver a detailed view on specific cases and the influence of the synoptic conditions on the total amount and the vertical structure of the water vapour. In the next two sections, one case from each AO phase is shown in detail and brought in context with the synoptics. The examinations are limited on clear-sky cases due to the limitation of the lidar measurements by clouds. Profiles below clouds could be considered too, but this study concentrates on the evaluation of clear-sky cases only.

5.2.1 Water vapour profiles during the negative phase of the Arctic Oscillation - Case 13 November 2019

The AO index was negative between October and end of November. As an example for the negative phase, the 13 November was chosen with an AO index of -2.177. The attenuated backscatter at 1064 nm showed clear-sky conditions between 07:00 and 21:00 UTC on that day without any clouds or aerosol layers. Figure 5.2a shows the temporal development of the height resolved WVMR for the time period between 13 Nov 2019 06:00 UTC and 14 Nov 2019 00:00 UTC. The black areas at the beginning and the end of the time period are heightranges without lidar measurements due to clouds. Missing values in the middle of the plot are due to small SNR's in that heights. The plot shows two water vapour layers, a descending moist layer between 06:00 and 17:00 UTC and an advected layer after 17:00 UTC above a surface layer. A cloud developed at the top of the advected layer at the end of the shown period. Figure 5.2b shows three selected profiles of the WVMR during the advection, its times are marked as lines of the same color in the colourplot. The profile at 16:40-16:50 UTC still shows a rest of the first water vapour layer between 600 and 800 m height and the arriving of the lofted layer in around 1.25 km height. The two later profiles clearly show how the lofted layer is growing in height and the dry layer below is decreasing. Corresponding profiles of temperature, wind speed and wind direction from the radiosonde are shown to evaluate the total process and differentiate between

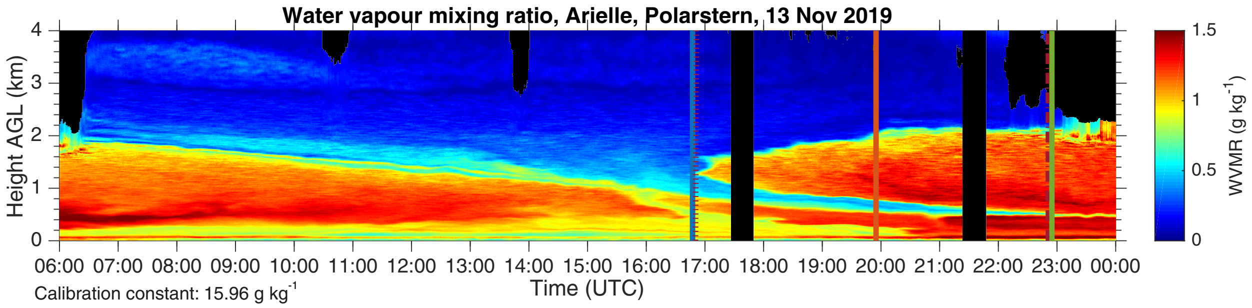

(a) The temporal evolution of the height resolved WVMR measured by the Raman lidar. The coloured lines represent the times, at which profiles of the WVMR and the temperature are shown in (b).

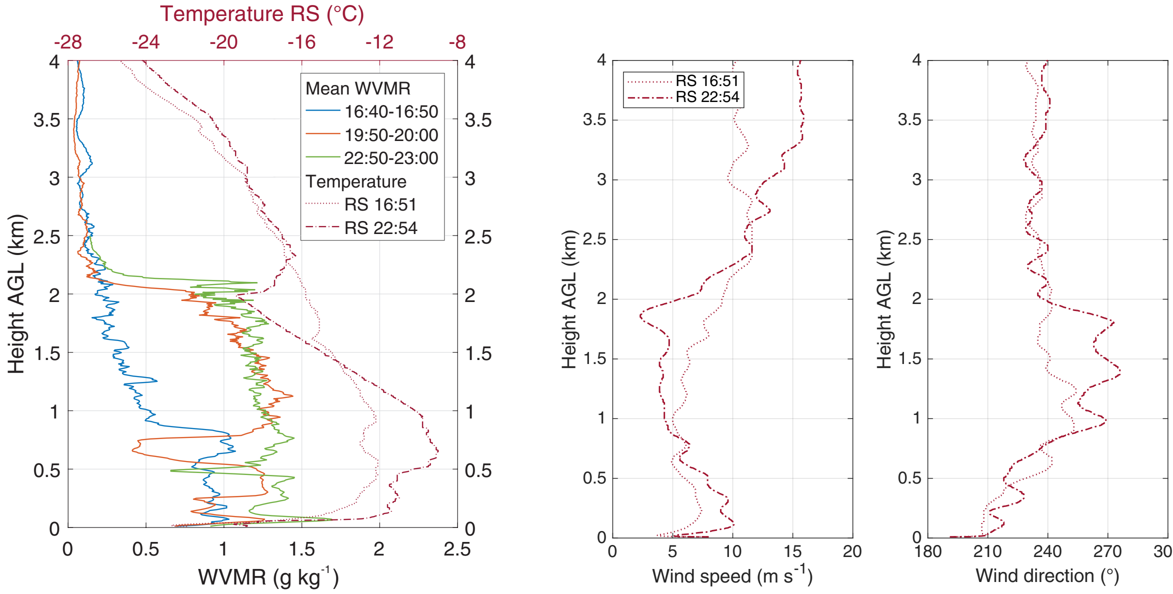

(b) Profiles of the WVMR of the lidar and the corresponding temperatures form the radiosonde.

(c) Profiles of wind speed and direction measured by the RS.

Figure 5.2: Lidar and radiosonde measurements for the measurement case on 13 November 2019 between 07:00 and 21:00 UTC.

airmasses. Typical for the Arctic is a strong surface inversion, but the shown profiles contain more than one temperature inversion. The heights of these temperature inversions correlate with the base or top height of the observed water vapour layers. Especially for the profile at 22:50-23:00 UTC, the lofted layer is limited by two strong temperature inversions, which seem to cause the strong gradients and clear boundaries of the layer. The values of the WVMR are not only increased inside this lofted layer but also in the surface layer compared to the earlier profiles. Beside, the radiosonde profile of 23:51 UTC shows warmer temperatures than at 16:51 UTC in both layers from the ground up to 1.5 km height, leading to the conclusion, that warm and most air was advected to the location of the Polarstern in the Central Arctic. The corresponding windprofiles show a lower wind speed and a different wind direction between 800 m and 1.5 km height, leading to the separation into two water vapour layers with a dry layer in between, which is limited by strong gradients. Considering all the shown parameters confirms that an airmass with different properties is advected from a remote place. The synoptics showed a strong high pressure system over the Beaufort Sea causing southerly winds at the location of the Polarstern with an inflow of airmasses from the Laptev Sea (Fig. A.1a). The Laptev Sea was already completely covered by sea ice (Fig. A.1b), but there are small areas of

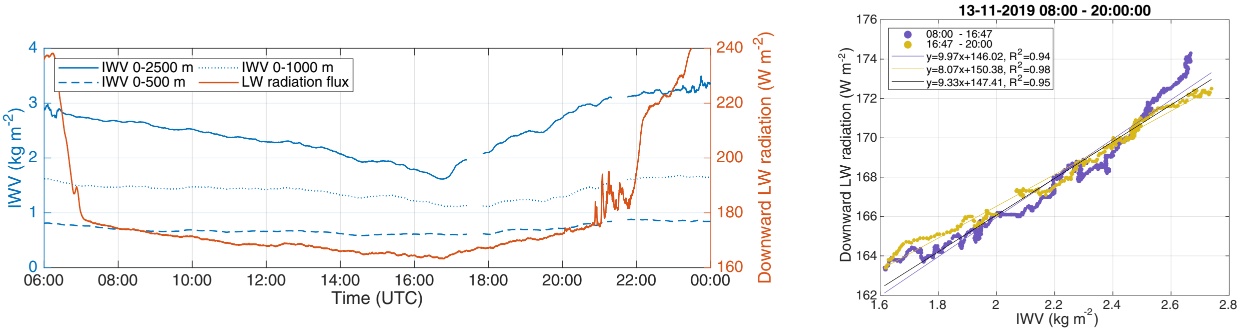

(a) The IWV was calculated for different height ranges and compared with the downward longwave radiation, which was measured at the surface.

(b) Correlation of the IWV between 0 and 2.5 km height and the downward longwave radiation for the descending moist layer and the advection.

Figure 5.3: Estimating the influence of water vapour on the downward longwave radiation at the surface for the case on 13 November 2019.

open ocean close to the coast of the New Siberian Islands, which could be a possible source of water vapour. Other possible sources could be open leads or polynyas in the sea ice or sources over land further south. Further investigations and the consideration of backward trajectories would be necessary to determine the sinks and sources of water vapour in different heights in more detail. Both, the colourplot and the WVMR profiles show a lot of small-scale structures and strong gradients, because of the high vertical resolution of the lidar data.

Beside looking at profiles, the integrated water vapour can be calculated from the lidar profiles (Eq. 3.21). Figure 5.3a shows the calculated IWV from different height ranges compared to the measured downward longwave radiation (DLR). The highest height range is up to 2.5 km for this case due to the missing data above, but this height range is covering the largest amounts of water vapour and the area of the highest temporal variability of the IWV. The IWV of that height range is decreasing until 16:47 UTC and increasing afterwards during the advection of warm and moist air. The DLR shows a similar evolution between 07:00 and 21:00 UTC, leading to the conclusion that the change of the total amount of water vapour with time is determining the temporal development of the DLR during clear-sky conditions. The influence of clouds on the DLR is visible in the beginning and the end of the time period and fog was present partly between 21:00 and 22:00 UTC, which caused higher values of the DLR. The IWV below 500 m is not changing much during the time period and also the IWV below 1000 m shows only small changes. Thus, the main variations occur in the height range between 1000 and 2500 m. Finally, the DLR was correlated with the IWV between 0 and 2.5 km height in Fig. 5.3b for the descending moist layer and the advected layer. The correlation coefficient of the linear fit is very high for all chosen time periods, but it is highest during the advection event between 16:47 and 20:00 UTC. The slope of the linear fit is a measure for the influence of the integrated water vapour on the DLR. A change in the IWV of 1 kg m^{-2} causes a differences in the DLR of 8.07 W m^{-2} during the advection, 9.97 W m^{-2} during the descending and 9.33 W m^{-2} in average for the whole time period on that day. To conlude, changes in the columnar integrated water vapour are the main influence on the DLR during clear-sky conditions.

The vertical gradients are analysed for the mean profile between 19:50-20:00 UTC and the results are shown in Fig. 5.4. Firstly, the vertical gradients were calculated over 5 bins centered around each height bin. The profile of those gradients is plotted in the middle plot of Fig.

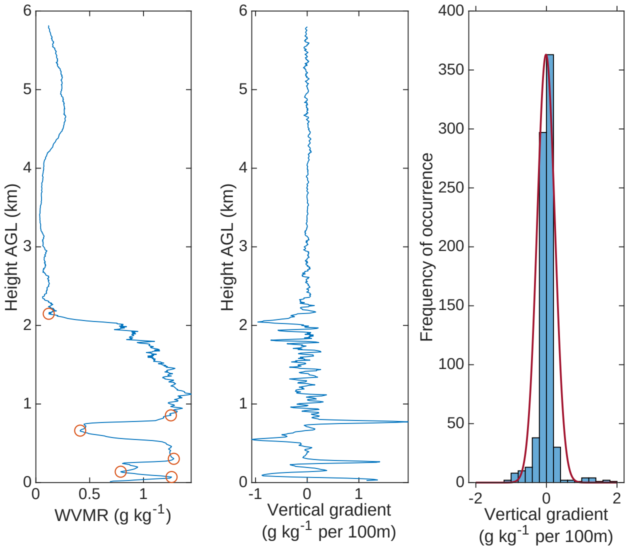

Figure 5.4: Mean WVMR profile at 13 Nov 2019 19:50-20:00 UTC with the determined heights of gradients larger than 0.4 g kg^{-1} per 100 m and with an absolute difference in the WVMR larger than 20% of the maximum WVMR of the profile (left). Vertical gradients over 5 bins centered around each bin plotted as profile (middle) and histogram (right). The red line in the histogram is the fitted normal distribution with $\mu_{\mathrm{n}} = 0.0117$, $\sigma_{\mathrm{n}} = 0.2523$ and a scaling factor of 2.2961 in y-direction (Eq. 5.1).

5.4. The gradients show small absolute values in most heights, but some positive and negative values are conspicuous, which mark the heights of very strong gradients at the base and the top heights of the water vapour layers. Plotting all the calculated gradients in a histogram reflects this result. There is a very high number of small absolute values of the vertical gradients and a decreasing number towards larger absolute values. There are more negative gradients and their number is decreasing towards higher absolute values, following the normal distribution. In contrast, there are larger absolute values of the positive gradients, but the number of positive gradients is already small for gradients larger than 0.5 g kg^{-1} per 100 m. The histogram shows a second small maximum around 1.2 g kg^{-1} per 100 m . That means, the water vapour layers have very clear boundaries at their base with strong positive gradients and large differences in the WVMR, while the WVMR decreases slowly at the top heights of the layers in this specific profile. The red curve shows the normal distribution, which was fitted on the data as explained in Sect. 5.1.2. The distribution of the measured gradients do not fit the normal distribution in that case, because medium high absolute values of the gradients are missing and there is this small second maximum at high positive gradients.

Secondly, gradients were calculated over height ranges with the same sign in the gradient per bin as explained in Sect. 5.1.2. To determine layers on the basis of these gradients, only the strongest gradients were chosen. The limits were set to a minimum gradient of 0.4 g kg^{-1} per 100 m and a minimum WVMR range of 20% of the profiles maximum. Height bins, that reach these limits are marked in the left plot in Fig. 5.4. The height of the largest negative gradients meet the boundaries of water vapour layers and could be used for a layer separation in this case. The largest gradient, that occur amounts to 0.96 g kg^{-1} per 100 m in a height of 71 m, but also the other two positive gradients are large with values of 0.80 and 0.72 g kg^{-1} per 100 m in heights of 303 and 855 m. The negative gradients are absolutely smaller. The strongest negative gradient was found in 138 m height and has a value of -0.70 g kg^{-1} per 100 m. It is the one in the lowest height, corresponding to the layer limited by the strongest positive gradient

at its base. This shallow humid layer close to the surface could be observed in many profiles, but not in all cases. Since it is no systematic error, it might be related to an influence of the ship during specific weather conditions. The negative gradients in greater heights have smaller absolute values with -0.42 and $-0.51\,\mathrm{g\,kg^{-1}}$ per 100 m in 661 and 2148 m height.
To conclude, the strongest gradients could be used for a layer separation for this specific case. The evaluation of gradients with different methods came to the conclusion, that the water vapour layers are limited by stronger gradients at their base than at their top for this advection case.

5.2.2 Water vapour profiles during the positive phase of the Arctic Oscillation - Case 11 February 2020

The Arctic Oscillation had an exceptional strong positive phase from January to March 2020 (Lawrence et al., 2020). The 11 February 2020 was chosen as an example case for the positive AO phase with an AO index of 4.422. The attenuated backscatter at 1064 nm showed cloudfree conditions between 00:00 and 14:00 UTC, but a thin aerosol layer was detected between 04:00 and 14:00 UTC. The temporal development of the height resolved WVMR is shown in Fig. 5.5a. It shows much lower values of the WVMR than the measurements on the 13 November 2019, with maximum values below $0.8\,\mathrm{g\,kg^{-1}}$, but still with a high variability. A lofted moist layer is visible after 03:00 UTC. The base of this lofted layer is at around 700 to 800 m height in the beginning as can be seen in the mean profile of the WVMR at 04:50-05:00 UTC in Fig. 5.5b. The later profiles show the lifting of the layer up to a base height of 2.8 km at 10:50-11:00 UTC. A temperature inversion is visible in the corresponding temperature profile at 04:48 UTC in around 1 km height, slightly higher than the base of the lofted moisture layer. This inversion is not measured anymore by the next radiosonde launch at 10:48 UTC. The profiles of wind speed and direction do not show clear changes inside the moisture layer. Thus, there are no indications for a different airmass. During the positive AO phase, the jetstream is strong and the Arctic airmass is enclosed with less exchange with lower latitudes, which could lead to the observed low values of the WVMR with high variability. The synoptics of that case show a low pressure system over the Kara Sea and high pressure over North America, which caused winds from East to Southeast at the location of Polarstern (Fig. A.2a). The inflow comes from the direction of the Laptev Sea, which is similar to the case from November 2019.
The two selected cases show, that a similar direction of the flow can cause contrasting amounts and vertical distributions of water vapour during different phases of the AO, in different seasons with different air temperatures. For a deeper conclusion about a relation between these parameters and the AO, more profiles are analysed in Sect. 5.4.

The IWV was calculated for different height ranges and compared to the measured downward longwave radiation at the surface in Fig. 5.6a. In a first step, the IWV was calculated from 0 to 3 km height, to exclude missing values in larger heights, because if the covered height range changes with time, the values of the calculated IWV may not be comparable. This consideration was a problem for that case, because of the ascending of moisture above 3 km. The comparison with the calculated IWV up to 3 km height in Fig. 5.6a shows a good conformity until 04:00 UTC, but strong differences afterwards. That means, the IWV up to 3 km do not cover the main part of the total column IWV and can not be used for comparisons with the DLR. In contrast, the missing values above 3-4 km height in the beginning have a negligible influence on the correlation of the IWV up to 5 km with the radiation. The values covered by the black areas are excluded due to the quality criterium at small SNR's. Small SNR's in those

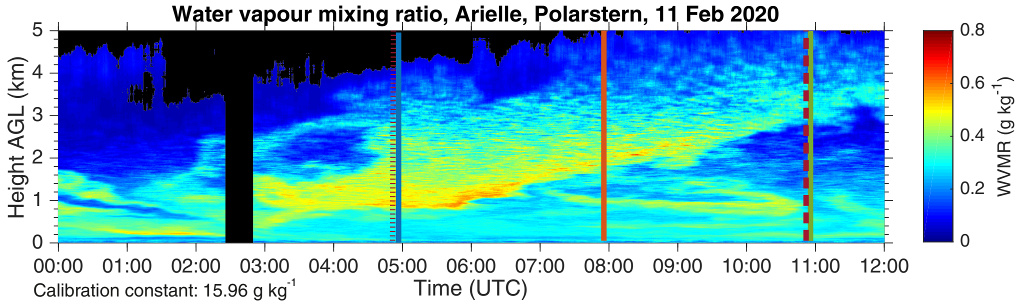

(a) The temporal evolution of the height resolved WVMR measured by the Raman lidar. The coloured lines represent the times, at which profiles of the WVMR and the temperature are shown in (b).

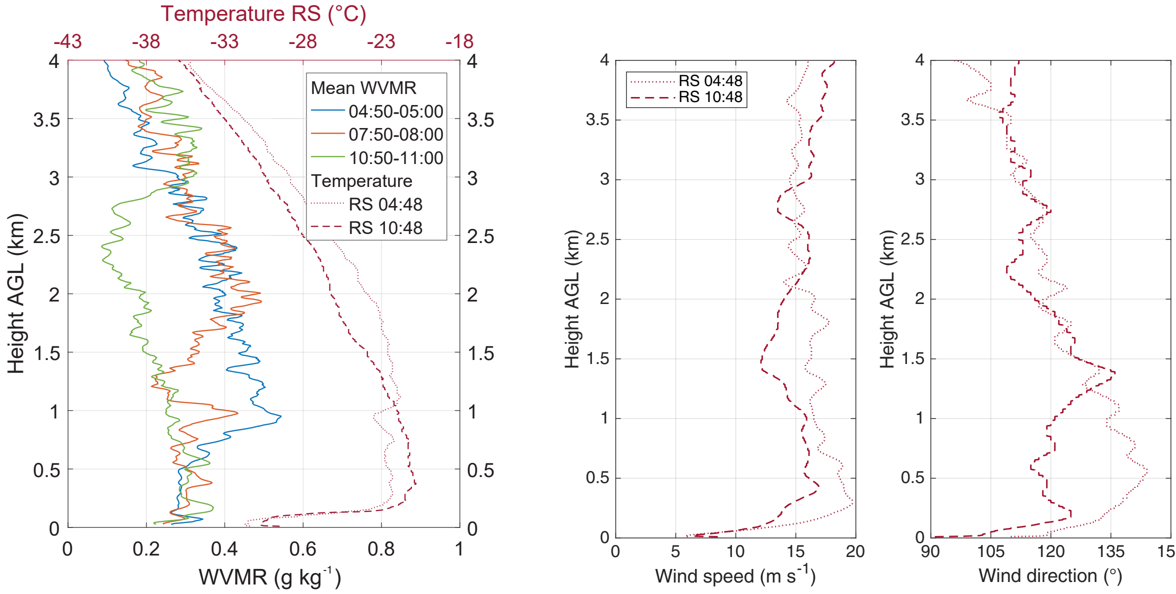

(b) Profiles of the WVMR of the lidar and the corresponding temperatures form the radiosonde.

(c) Profiles of wind speed and direction measured by the RS.

Figure 5.5: Lidar and radiosonde measurements for the measurement case on 11 February 2020.

heights imply low values of the WVMR, which have a small impact on the IWV. The comparison with the radiation shows, that it is better to take the maximum height reached by each profile although it changes drastically over time, instead of cutting all profiles at the smallest maximum height for the calculation of an IWV. The total height range up to 5 km height was then separated into two layers, where the lower layer is below the lofted water vapour layer and covers the height range from the surface to 800 m height. Its IWV is very small and stays relatively constant over time. The temporal variability of the IWV is determined by the water vapour between 800 m and 5 km height. The temporal development of the DLR and the IWV between the surface and 5 km height is very similar except for a small peak in the DLR around 01:50 UTC, which is due to some fog close to the surface. The DLR is correlated to the IWV for the time with the best correlation between 02:00 and 11:00 UTC (Fig. 5.6b). The correlation shows a high linear correlation coefficient of 0.97. In contrast, the correlation of the DLR and the IWV below 3 km (Fig. 5.6c) shows only a good linear fit between 01:00 and 05:00 UTC and large differences afterwards. This example shows, that the DLR only correlates linearly with the IWV, if the IWV includes the main amounts and variability of water vapour. The choice of the height range is crucial.

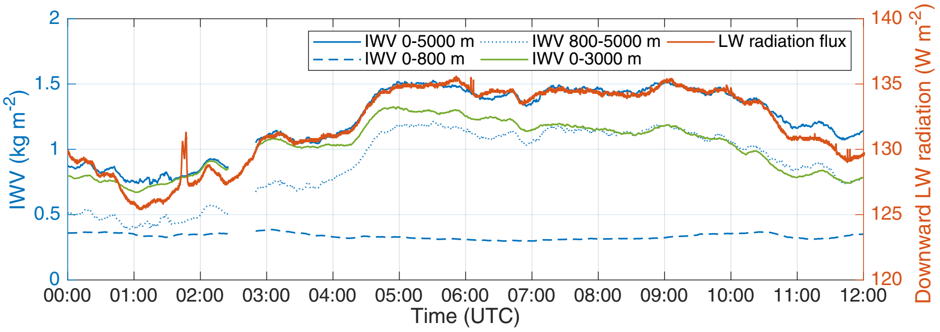

(a) The IWV was calculated for different height ranges and compared with the downward longwave radiation, which was measured at the surface.

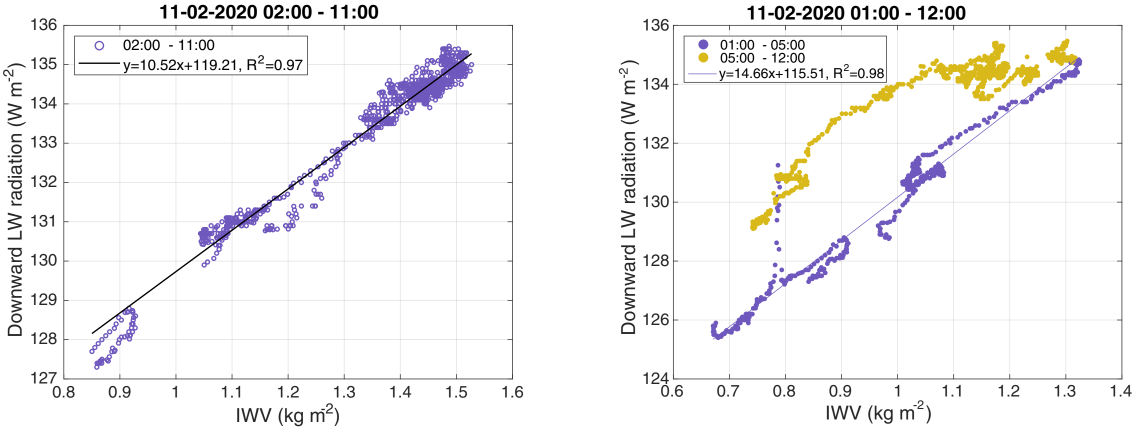

(b) The IWV between 0 and 5 km height is linearly correlated to the downward longwave radiation between 02:00 and 11:00 UTC.

(c) The IWV between 0 and 3 km height is only linearly correlated to the downward longwave radiation between 01:00 and 05:00 UTC, because the IWV of that height range covers the main amounts of water vapour uncompletely.

Figure 5.6: Estimating the influence of the water vapour on the downward longwave radiation at the surface for the case on 11 February 2020.

The mean profile at 10:50-11:00 UTC is analysed according to its gradients as shown in Fig. 5.7. The top height of the profile is in 5.19 km due to small SNR's above this altitude. Gradients of layers with the same sign in the gradients over one bin were calculated according to Sect. 5.1.2. The limits for strong gradients were set equally to the case of the 13 Nov 2019 to 0.4 g kg^{-1} per 100 m in the gradients and a minimum WVMR range of 20% of the profiles maximum. In that case, no gradients are found, that match these limits. Hence, the example profile do not include strong gradients over a relatively large WVMR range, although the WVMR range was defined relative to the maximum WVMR of the profile. The profile of the gradients over 5 bins shows no exceptional peaks, but similar gradients in all heights, changing between positive and negative values. These fluctuations are the sum of the instrumental noise of the lidar and the real atmospheric variability. The histogram shows a normal distribution of the gradients around a mean value of -0.0027 g kg^{-1}. The standard deviation is much smaller than for the case in November and amounts to 0.090 g kg^{-1}, reflecting that the most gradients are very small with absolute values close to 0. Larger gradients occur with similar numbers of values with positive and negative signs. The largest gradient is a positive gradient, which amounts to 0.4058 g kg^{-1}/100m and is located close to the surface. A larger bin range may be

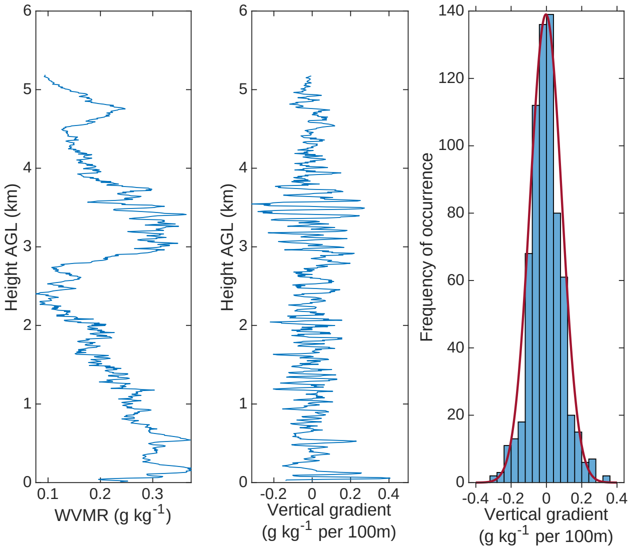

Figure 5.7: The mean WVMR profile at 11 Feb 2020 10:50-11:00 UTC (left), its vertical gradients over 5 bins centered around each bin plotted as a profile (middle) and as a histogram (right). The red line in the histogram is a fitted normal distribution with $\mu_\mathrm{n} = -0.0027$, $\sigma_\mathrm{n} = 0.0900$ and a scaling factor of 31.35 in y-direction (Eq. 5.1).

more appropriate for the calculation of gradients in that case to exclude the small-scale variations, but the bin range over 5 bins was chosen for both shown case studies for comparison. A larger bin range in the November case would have led to an underestimation of the very strong gradients in that measurements.

5.2.3 Summary from case studies

The case studies showed very different conditions for the negative and the positive phase of the Arctic Oscillation. While the absolute values of the WVMR and the IWV were much higher during the negative phase, both cases showed a high temporal and vertical variability. In general, a relation of the vertical distributed water vapour to temperature and wind profiles could be seen. Temperature inversions occured often in the heights of strong gradients in the WVMR and limited the water vapour layers vertically. The temporal and vertical change in temperature, wind speed and wind direction in the height of a water vapour layer is an indication for the advection of a different airmass in a certain height. The synoptic maps deliver information about the main wind direction and possible source regions of the airmasses. For a detailed consideration of the sources of the measured water vapour, backward trajectories would be necessary, which were not part of this study.

Beside, the case during the negative phase of the AO with large amounts of water vapour showed much stronger vertical gradients than the positive case with small WVMR values. The frequency distribution showed a maximum at low absolute values of the gradients for both cases, but with a normal distribution only for the positive case. For the case with the negative AO index, a second maximum at large positive gradients was found in the frequency distribution. Furthermore, the water vapour layers were limited by stronger positive gradients at their bases than negative gradients at their top.

5.3 The influence of the vertical distributed WVMR on the downward longwave radiation during clear-sky conditions

5.3.1 Results from correlating IWV, DLR and temperature

The case studies in Sect. 5.2 showed a linear correlation between the measured downward longwave radiation and the calculated IWV of a height range, that covers the main part of the total column IWV. Seven completely cloudfree cases were analysed regarding the influence of the water vapour on the DLR. A linear correlation between the IWV of the highest possible height range and the DLR was found for each of those cases. Fig. 5.8a combines the correlation data of all those cases in one plot, showing a shift of the linear functions in y-directions and a slightly change of the slopes. Table 5.1 lists the date and time period used for the correlation of each case, as well as the correlation coefficient, the slope m and the y-intercept n of each linear equation. The correlation coefficients of the chosen time periods are very high with values larger than 0.9, except for the case on 11 Dec 2019, where the correlation coefficient amounts to only 0.67 due to small changes in the IWV over time. The case is still included in the considerations, but is excluded from the comparison of the slopes and the y-intercepts of the linear fits. The slopes of the linear fits of all cases cover a range between 9.33 and 15.03 $\mathrm{W\,kg^{-1}}$, excluding the 11 Dec 2019. That means, an additional 1 $\mathrm{kg\,m^{-2}}$ IWV in the atmosphere causes a $9.33 - 15.03\,\mathrm{W\,m^{-2}}$ higher longwave radiation at the surface during clear-sky conditions in the Arctic winter. The correlation data in Fig. 5.8a and Table 5.1 show a different shift in y-direction for the cases, but the slope changes in a different manner. The height ranges for the calculation of the IWV differ for the cases and are listed in the plot, but they deliver no explanation for the different linear equations and the shifts in y-direction.
In contrast, different air temperatures during the seven cases were found to be one reason for the differences in the linear functions. The surface temperature could be taken for a first evaluation, but the temperature of the water vapour, that emits the radiation is more appropriate. Thus, a mean temperature over the heights with the largest amounts of water vapour was defined (Sect. 5.1.3) to get one characteristic temperature for the vertical distributed water vapour with changing temperatures. This mean temperature from the 90. percentile of the WVMR profile was calculated for each WVMR profile and is represented by the colours in Fig. 5.8b. A clear correlation of the temperatures to the data is visible. The same amount of IWV causes a higher longwave radiation flux at the surface, if the temperature of the largest amounts of water vapour is higher.

The used temperatures were further evaluated by comparing them with the radiation temperature of the sky in Fig. 5.9. The radiation temperature of the sky was calculated from the Stefan-Boltzmann law by inserting the measured longwave radiation flux and calculating the corresponding temperature from Eq. 3.7. As the pyrgeometer measures the longwave radiation that is emitted from all directions of the sky, the derived temperature represents the radiation temperature of the sky assuming it is a black body. The longwave radiation, that is emitted by water vapour is contributing to the measured value, but there are more components of the atmosphere emitting longwave radiation, as for example molecules, greenhouse gases, haze, ice crystals or invisible thin cirrus clouds (Hogan & Bozzo, 2018). Comparing the 90. percentile temperature of the WVMR with the radiation temperature of the total sky in Fig. 5.9 shows a linear correlation with a correlation coefficient of 0.86. That means, the WVMR greater than the 90. percentile of the profile contributes to the measured longwave radiation flux substan-

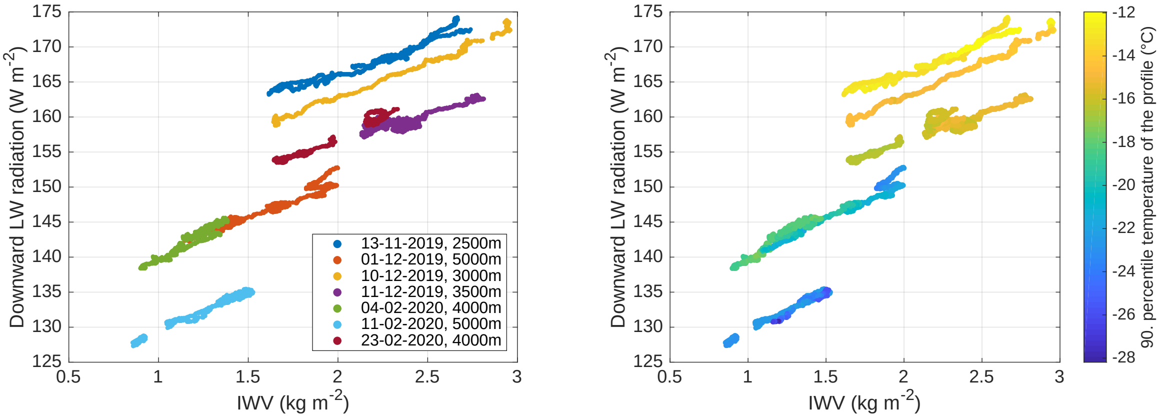

(a) Correlation for the seven selected cases. The IWV was calculated from the surface up to the given height. The data of each case are linearly correlated, but shifted in x- and y-direction.

(b) The mean temperature from the 90. percentile of the WVMR profiles is related to the linear fits between the DLR and the calculated IWV.

Figure 5.8: Correlation of the downward longwave radiation and the integrated water vapour calculated over different height ranges for 7 cloudfree cases in winter 2019-2020.

tially for all shown cases. The measurements in the middle of Fig. 5.9 stand out with large deviations from the linear fit. There are two possible explanations for this behaviour. On the one hand, the amount of water vapour could play a role, which is represented by the colours in the plot. The shown values are the mean WVMR of all heights, where the WVMR is larger than the 90. percentile of the profile. Low amounts of warmer water vapour contribute less to the DLR than large amounts of colder water vapour. On the other hand, the data with the largest deviations belong to the measurements from 01 to 02 Dec 2019. A cloud was present before the correlation time period, leading to an increased WVMR in the height of the dissolved cloud. That means, the calculated 90. percentile temperature is smaller, because of the larger height and the cooling due to evaporation, but the mean WVMR from the 90. percentile is high. Furthermore, the measured DLR could be influenced by the cloud, because it is measuring the radiation from the total hemisphere. The data of this case also stand out in Fig. 5.8b with lower temperatures at higher IWV and downward longwave radiation. Thus, this case differs from the others, because it is influenced by a dissolving cloud. The shown parameters are related differently and show a more complex correlation, leading to the conclusion, that the

Date	Time period	corr. coeff. R^2	slope m	y-intercept n
13-11-2019	08-20:00 UTC	0.95	9.33	147.41
01 to 02-12-2019	23:30-10:00 UTC	0.96	9.53	131.51
10-12-2019	11-16:30 UTC	0.99	10.03	142.73
11-12-2019	03-20:00 UTC	*0.67*	*6.27*	*144.52*
04-02-2020	08-17:30 UTC, excl. 11-12:10	0.92	15.03	124.55
11-02-2020	02-11:00 UTC	0.97	10.52	119.21
23-02-2020	16-21:00 UTC	0.93	13.17	133.03

Table 5.1: 7 cloudfree cases were chosen for the correlation of the DLR with the IWV of the highest possible height range. The slope m and the y-intercept n refer to the calculated linear equations $y = m \cdot x + n$ of the correlations of each case.

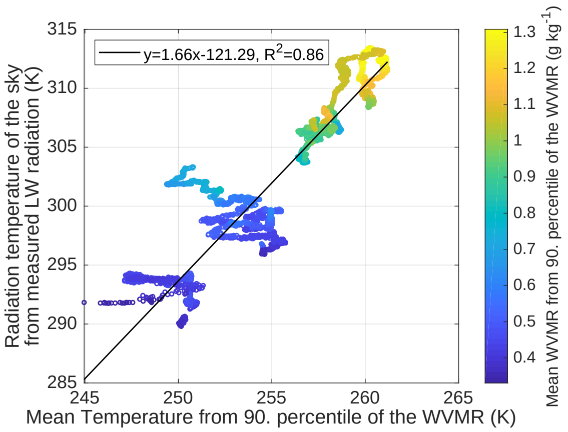

Figure 5.9: Correlation between the radiation temperature of the sky, which was calculated from the measured DLR at the surface, and the mean temperature from the 90. percentile of the WVMR for the seven selected cases (cf. Tab. 5.1).

simplified linear correlation only apply to similar and totally cloudfree cases. Nevertheless, the data are spread around the linear fit, which seems to be related to the amount of water vapour. To conclude, the measured DLR at the surface is influenced by the total amount of water vapour and its temperature during clear-sky conditions. For detailed calculations of the DLR at the surface, the vertical distributed WVMR and its temperatures would have to be considered. Fig. 5.8b and 5.9 show, that using the introduced method of determining the temperature of the largest amounts of water vapour, is a reasonable method for an initial estimate of the influence of the water vapour temperature on the DLR. The relation between the vertical distributed water vapour, its temperature and the DLR is complex and radiative transfer modelling would be necessary for further evaluations.

5.3.2 Discussion of the correlation between IWV, DLR and temperature

A comparison of the results with model studies from literature showed a good agreement regarding the correlation between the IWV and the DLR. Ghatak & Miller (2013) calculated monthly mean values of precipitable water vapour (PW) and downward longwave flux (DLF) from two different models between 1979 and 2011 and found a nonlinear correlation for all seasons (Fig. 2.1). As the IWV shows a strong seasonal cycle in the Arctic, the measurements from the MOSAiC winter cover only a small part of this correlation. Beside, the IWV was taken for the MOSAiC data instead of the PW, looking only at clear-sky cases and only on winter data. The temporal scale and the data range are much smaller for the MOSAiC data. Nevertheless, the calculated values from the MOSAiC winter data fit to the mean values from the models for the winter months. The comparison with that study illustrates, that analysing the winter data is only a small part of the relationship between the IWV and the DLR and an apparent linear correlation could also be a small part of a non-linear correlation. Nevertheless, a linear correlation is reasonable on smaller scales to the measurements of single cases.

Several quantities contribute to the uncertainty of the correlation. The calculation of the IWV was done for the highest possible height range for the complete time period of each case. The example of the 11 February 2020 showed, that this can lead to uncertainties if the contribution of the water vapour to the IWV is too high above the chosen height range. On the other hand, the development of the IWV is influenced by missing data in certain heights and at certain times, if it is calculated from larger height ranges. The reason for the missing data in that heights are very low values of the WVMR for the cloudfree cases, so that the impact on the IWV is very small. Beside, the height ranges are determined manually for each case, which could also lead to some uncertainties. A second discussable fact is the usage of the 90. percentile temperature as characteristic temperature for a profile. All WVMR values larger than the 90. percentile of each profile represents the largest values of the WVMR profile, but do not represent necessarily one water vapour layer. Taking a smaller percentile would counteract this fact, but still not cover a water vapour layer. Moreover, the mean temperature of a larger layer would be calculated over a wider temperature range and thus would be less representative for the layer. The advantage of taking the 90. percentile is to get a temperature of the maximum WVMR from a height range instead of a single height, which reduces uncertainties. Taking this temperature to calculate the longwave radiation of the water vapour in the respective heights with the Stefan-Boltzmann-law is a strong simplification, because of the assumption of the water vapour as a black body and the missing influences of molecules and greenhouse gases. Nevertheless, the results showed, that the calculated 90. percentile temperature can represent similar cases similarly and a linear correlation with the radiation temperature of the total sky is possible.

5.4 Statistical analyses of WVMR profiles and the influence of the Arctic Oscillation

Statistical analysis of many WVMR profiles were done to get an overview over the vertical structure of water vapour during the Arctic winter and to consider a possible relation to the Arctic Oscillation. All examinations are only done at clear-sky conditions due to the limitations of the lidar measurements by clouds. In total, 71 profiles of the WVMR were selected (Sect. 5.4.1) together with the corresponding temperature profiles. All profiles are analysed according their minimum, maximum and mean values to get an overview over the winter period (Sect. 5.4.2). Beside, the profiles are separated into different layers and the IWV of those layers is determined to examine the vertical distribution of water vapour (Sect. 5.4.3). In Sect. 5.4.4, the vertical gradients of the WVMR profiles are evaluated.

5.4.1 Choice of measurement cases for the statistical evaluations

71 profiles were chosen for the statistical analyses between the 25 October 2019 and the 29 February 2020. The profiles are chosen from clear-sky cases, whereat cases with clouds above 6 km height were treated as clear-sky. Most of the profiles are the same profiles, that were used for the calibration with the radiosonde, because they are cloudfree cases with corresponding temperature profiles from the radiosondes. The profiles are randomly distributed over the winter period and not chosen manually. To fill the gaps in the timeline, additional profiles of cloudfree periods were chosen between the calibration cases. These profiles are mostly not at the time of a radiosounding, so that the radiosonde data were linear interpolated over time. This interpolation comprise uncertainties in the temperature profiles due to differences between the interpolated profile and the true profile at that time. Most of the additional profiles could be chosen from cloudfree conditions, but some cases contain layers with high attenuated backscatter probably due to aerosol. The profile of the 16 Dec 2019 contains a cloud above 3.5 km height and the profile at the 17 Nov 2019 shows a layer of very high backscatter in

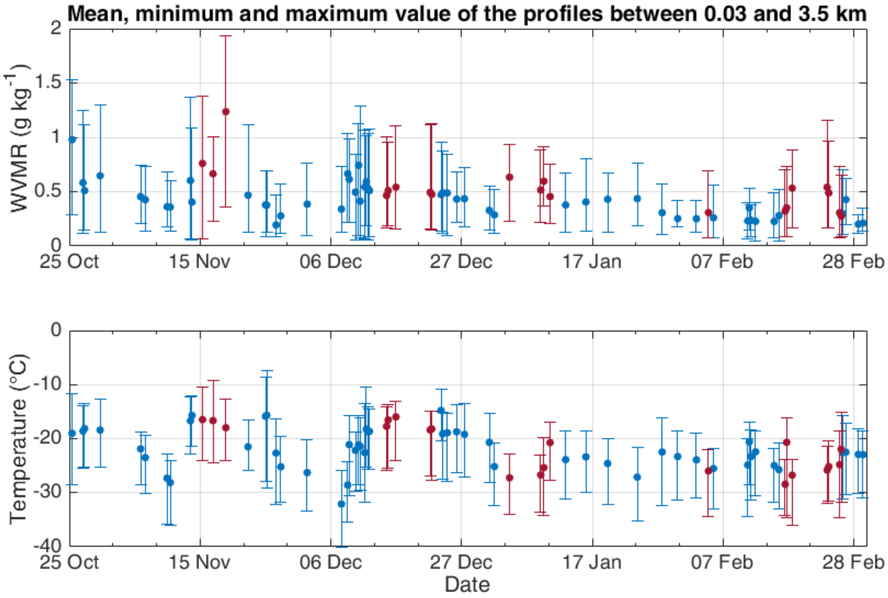

Figure 5.10: Overview over the WVMR and temperature value ranges of the selected 71 cases. The profiles were evaluated between 30 m and 3.5 km height. The dots represent the mean values, the ends of the bars the respective minimum and maximum values. The blue values mark the cases already used for calibration, the red values represent the additional chosen profiles.

around 500 m height. All additional profiles are chosen by eye and thus are influenced by the manual choice. They are marked in red in Fig. 5.10 to account for all these impacts.
Each WVMR profile is averaged over 10 minutes and a SNR threshold of 5 was used for the lidar data processing. The maximum height, that is reached by each profile depends on the SNR threshold and the number of water vapour molecules and differs for each case. To get comparable results, all statistical evaluations were done for the height range between 30 m and 3.5 km height. The minimum height was chosen to reduce influences of the ship. The maximum height was selected, because most of the profiles reach this height. 5 profiles end between 3 and 3.5 km height and 3 profiles even below 3 km, as can be seen in the analysis of water vapour layers in Fig. 5.12. The reason for the cut of the profiles in a certain height is a low SNR of the water vapour signal due to clouds or low WVMR's. The selected profiles are mainly cloudfree, so that the WVMR values are very low above the cut and have small impacts on the analyses.

5.4.2 Temporal development of the WVMR and the temperature

To get an overview over the WVMR profiles, a mean, maximum and minimum WVMR was calculated from each profile. The results are plotted in Fig. 5.10. Changes between higher and lower WVMR values occur during the whole shown time period, but higher maximum values are reached in October and November during the negative phase of the AO. During the positive phase from January on, the WVMR range is smaller. The profile from the 19 Nov 2019 03:00-03:10 UTC stands out with the highest WVMR values. A cyclone passed over Polarstern two days before, which led to the extraordinary high values in the WVMR. The same evaluation was done for the corresponding temperature profiles to investigate a possible relation. The temporal variation shows a similar trend as that of the WVMR, but also some differences. It is colder in January and February, when the AO index was positive, than in October and November with negative AO indices and the temperature variations are smaller. Colder air can contain less water vapour than warmer air, but if the temperature is higher the air does not necessarily have to contain more water vapour. Hence, the range of the WVMR values is mostly larger for higher temperature ranges, but not for every case. Furthermore, the largest WVMR values have not to be in the same height as the highest temperatures. On the other hand, the water vapour influences the surrounding temperatures by emitting longwave radiation, that warms the atmosphere or the surface. To conclude, the WVMR values do not only depend on the synoptics, but also on the air temperature. The air temperature is determined by the synoptics and the AO index is based on the large-scale synoptics. Thus, the profiles of the WVMR and the temperature are connected to the AO index.

5.4.3 Analysis of vertical water vapour layers

The WVMR profiles were vertically divided into different layers as defined in Sect. 5.1.1 using two different methods. For the first method, temperature inversion heights and strengths were determined, which are plotted in Fig. 5.11a. A strong surface inversion is present most of the time in the Arctic due to the very cold surface temperature above the sea ice. Weaker surface inversions with higher surface temperatures occur mainly in October and November during the negative phase of the AO. A possible reason could be a smaller sea ice fraction during that time of the year due to the uncomplete freezing or due to more open leads and polynyas caused by more cyclones during the negative phase of the AO. The strongest surface inversions are reaching the highest altitudes and occur during the positive phase of the AO in January and February and during the transition phase in December. Some cases show only one temperature inversion with a height up to 800 m, but for many cases there is at least one small temperature inversion above the surface inversion in higher altitudes.

The IWV of each layer between two temperature inversions is plotted in Fig. 5.11b, weighted with the layer height. The layer with the highest IWV per 100 m is mostly the lowest layer, namely the layer below the strong surface inversion. That means, the largest amounts of water vapour are located close to the surface restricted by a strong temperature inversion. This could be an indication for a coupling of the moisture to the surface. Beside, there are cases with the highest IWV per 100 m in an elevated layer above the surface inversion as for example on the 13 Nov 2019 or the 18 Feb 2020, representing a decoupling of the main moisture from the surface, that may be related to an advection of moisture. Moreover, there are cases with small IWV in all layers independent from the inversion strength of the respective layers. During the negative phase of the AO in October and November, the layer IWV reaches higher values than during the positive or the transition phase. The IWV is very low from mid January to mid February. In contrast, there is an alternation between days with high layer IWV in some heights and days with low layer IWV in all heights during the whole time period except in December, which could be related to synoptic events as for example passing cyclones. For a relation of the vertical water vapour structure and the AO index, the December is considered separately, because of the transition between the negative phase of the AO and the following exceptional strong positive phase of the AO (cf. Sect. 2.3.2). The profile from the 19 Nov 2019 stands out again with the highest layer IWV. A closer look into the temperature profile showed high surface temperatures, which decrease with height and the first inversion in 900 m height. A similar behaviour of the temperature profile was observed in the next selected profile on 22 Nov 2019 16:55-17:05 UTC, but with decreased values in the WVMR profile. Both cases are related to two cyclones, which passed over Polarstern on 16-17 and on 20 Nov 2019.

The second method for the determination of water vapour layers uses the minima in the WVMR profile as layer boundaries (cf. Sect. 5.1.1). The determined layers and their layer IWV are

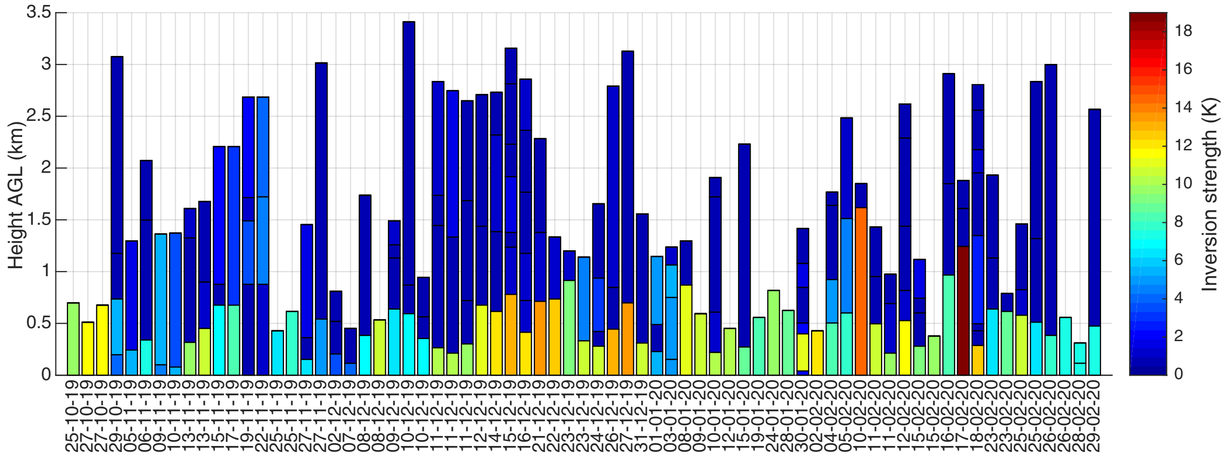

(a) Temperature inversion strength of all detected temperature inversions between 30 m and 3.5 km height. The inversion strength was defined as the temperature difference between the local maximum at the inversion height and the local minimum in the layer below. The layers represent the height range between two local temperature maxima and give no information about the temperature development within the layer.

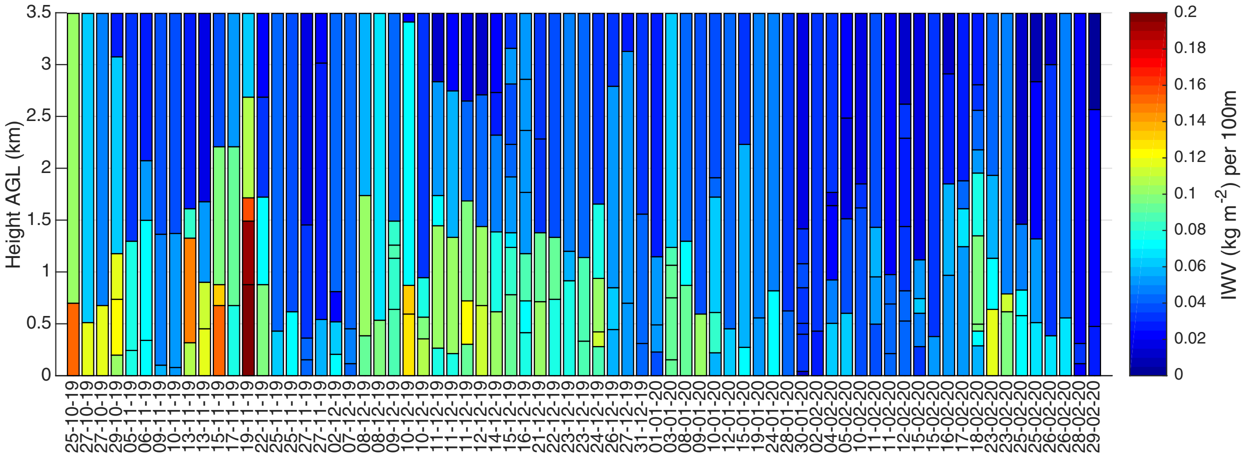

(b) IWV of the water vapour layers separated by the detected temperature inversions. The IWV of each layer was weighted with the layer height.

Figure 5.11: Division of the 71 selected WVMR profiles into layers separated by temperature inversions (TI) larger than 0.3 K. The upper limit of each stacked bar mark the height of the temperature maximum, the colours represent the inversion strength (a) and the layer IWV (b). The selected profiles are ordered in time, but not equally distributed on the x-axis.

plotted in Fig. 5.12. Two groups of cases can be distinguished for the vertical distribution of the water vapour. Firstly, there are cases with a shallow surface layer and the main amount of water vapour in an elevated layer. The highest layer IWV is mostly contained in the second layer. The surface layer is very shallow with heights mainly below 200 m and contains always less IWV than the layer above. This lowest layer could be seen in many lidar profiles as a peak in the WVMR. It was not checked, if the lidar profiles are correct for the lowest heights. The peak was not be found in every lidar profile, as it is also visible in the analysis in Fig. 5.12, leading to the conclusion, that it is no systematic error of the lidar and has to be included in the analysis. Possibly, the peak is a result of an influence of the ship or its orientation in the wind on the measurements at the lowest altitudes during specific weather conditions. The

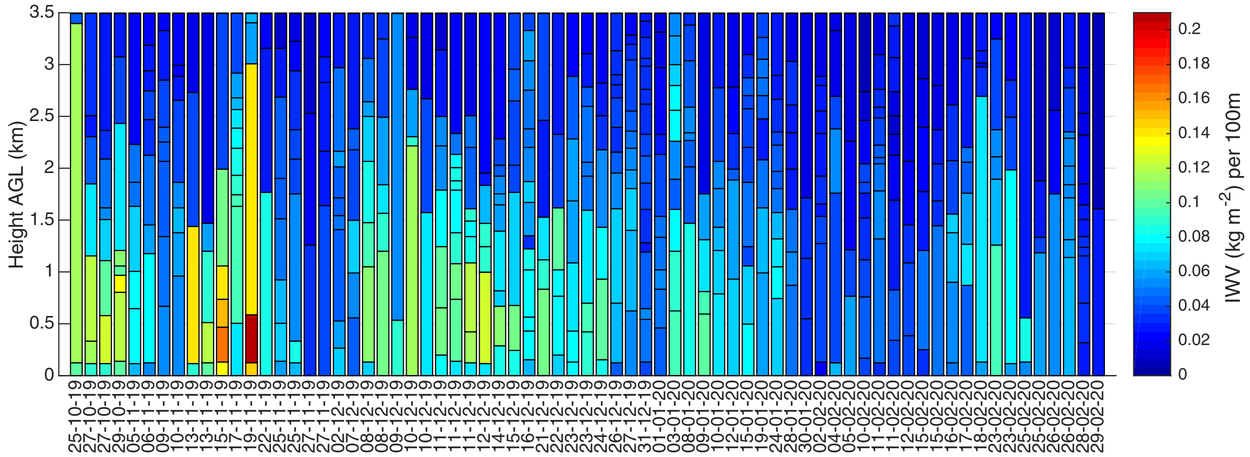

Figure 5.12: Division of the 71 selected WVMR profiles into layers separated by minima in the WVMR profile with a minimum prominence of 10% of the absolute maximum of each profile. The upper limit of each stacked bar mark the height of the local minimum in the WVMR, the colours represent the IWV of each layer weighted with the layer height. The selected profiles are ordered in time, but not equally distributed on the x-axis.

layer, that contains the most water vapour is elevated from the surface for this first group and seems to be decoupled from the surface. A second group of cases shows a large surface layer, that contains the highest IWV per 100 m and a decreasing layer IWV in the layers above. In those cases, the moisture seems to be coupled to the surface. Beside, there are cases in both groups, which represent a very dry atmosphere and show very low values of the layer IWV in all heights. The highest layer IWV occur in October and November during the negative phase of the AO. In contrast, the values of the layer IWV are small during the positive phase of the AO including many cases with very dry conditions. The temporal variety between moist and dry cases is equal to Fig. 5.11b, as the same water vapour content is separated in different layers.

To proof the influence of synoptic events, the synoptic conditions were checked for the periods with higher layer IWV's. Cyclones passed north of the Polarstern on 16-17 Nov and 20 Nov 2019, which led to higher amounts of water vapour around these days. Another cyclone south of Polarstern influenced the conditions at the location of Polarstern between the 18 and 25 Feb 2020. Several periods with southerly winds from the direction of Siberia, Laptev or Kara Sea or from the Barents Sea were found between 25-30 Oct 2019, on 13 Nov 2019, 6-11 Dec 2019, 03-06 and 12-16 January 2020. During all those periods, higher values of the layer IWV are observed. This indicates two main sources for water vapour in the Eastern Central Arctic, which are passing cyclones or a main wind direction from the Seas north of Siberia namely Laptev, Kara and Barents Sea. This finding correlates with the results from Vázquez et al. (2016), who found Siberia to be one of four source regions for water vapour in the Arctic, but also showed the major influence of each source on the region northeast of the source. As the Polarstern was located northeast of Siberia during the winter period 2019/20, the presented source region fits to the findings from Vázquez et al. (2016).

To conclude, the temporal variety of the layer IWV in the Eastern Central Arctic during winter is influenced by synoptic events like the passage of a cyclone or a wind direction from Siberia/Laptev Sea or Barents Sea and Kara Sea in all phases of the Arctic Oscillation, but the layer IWV reaches higher values during the negative phase of the AO than during the positive phase. The air temperatures were higher and showed larger variations from October to December 2019 than in January and February 2020, which correlates with the time periods of the negative or transition phase and the positive phase of the AO and has an influence on the possible amounts of water vapour in the atmosphere. Hence, the temporal development of both, the air temperature and the WVMR are related to the recent synoptics at the location of Polarstern and thus to the AO index.

5.4.4 Analysis of the vertical gradients of the WVMR

The vertical gradients were calculated for each of the selected profiles within the selected height range between 0.03 and 3.5 km height. To exclude large gradients over only one bin, they were calculated over the range of 5 bins centered around each measurement bin (cf. Sect. 5.1.2). The frequency of occurence of the determined gradients is plotted as a histogram in Fig. 5.13 for all cases and separated in cases with a positive or a negative AO index. A normal distribution was fitted on the data as explained in Sect. 5.1.2, which fits very well for all times. The parameters of the function of the normal distributions are shown in Tab. 5.2. They show a slightly negative mean value for all, the positive and the negative AO cases, which means, negative gradients occur more often than positive gradients. The standard deviation of the distributions is larger during the negative phase of the AO, leading to a broader distribution and a more frequent occurence of stronger gradients. A closer look on the edges of the distributions is showing a gap towards large absolute values of the gradients. This gap is located at smaller absolute values and has a larger width for the positive cases than for the negative cases. During the positive phase of the AO, smaller values of the WVMR and the IWV were found, leading to the observed smaller gradients. Large positive or negative gradients occur very seldom, medium high gradients are missing completely in the distribution. In contrast, the distribution is more uniform during the negative phase of the AO and strong positive or negative gradients occur more often. All the distributions show a small unbalance towards positive gradients at large absolute values of the gradients. Considering only gradients with an absolute value larger than 1 g kg^{-1} per 100 m, positive gradients occur with a number of 43 more often than negative gradients with a total number of 30. The difference is particularly large during the negative phase of the AO with a number of 33 positive gradients and 22 negative gradients. Beside, these numbers confirm the higher occurence of large gradients during the negative AO phase, where a total number of 55 absolute values of the gradients were larger than 1 g kg^{-1} per 100 m in contrast to only 18 during the positive phase. The number of evaluated profiles may not be large enough to draw conclusions about the edges and the occuring gaps in the distributions, but it is large enough to derive tendencies in the shape of the distributions.

To conclude, the profiles of the WVMR contain small gradients in most of the heights, but also some strong positive and negative gradients. Strong positive gradients occur more often than strong negative gradients, which implies more clear boundaries at the bases of water vapour layers than at their tops. More high absolute values of the gradients occur during the negative

	mean μ_{n}	standard deviation σ_{n}	scaling factor
All cases	-0.0091	0.2061	4 505
Positive AO	-0.0073	0.1888	2 644
Negative AO	-0.0120	0.2311	1 813

Table 5.2: Parameters of the normal distribution functions (Eq. 5.1) for all gradients of all profiles and separated in cases with positive and negative AO index.

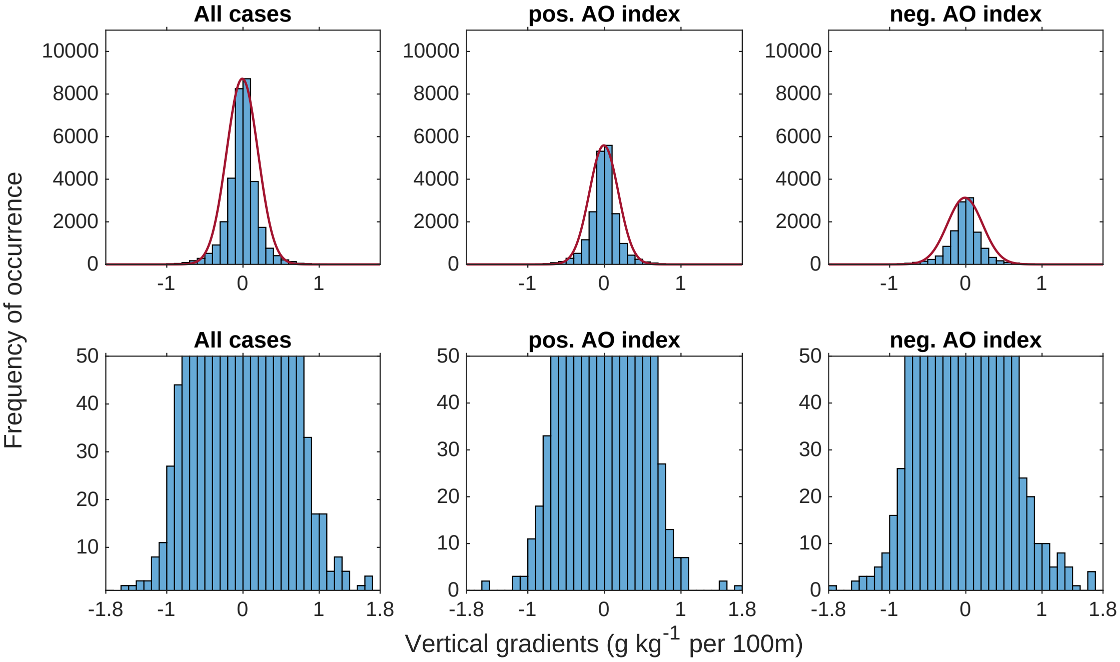

Figure 5.13: Frequency of occurence of the vertical gradients of all shown profiles and separated in all cases with positive or negative AO index. The gradients were calculated over 5 bins centered around each measurement bin. Only gradients from the analysis height range between 0.03 and 3.5 km are evaluated.

AO phase, which could be related to the observed larger amounts of water vapour or more advection of water vapour into the Arctic due to a larger meridional tranport.
A second opportunity of calculating the gradients of the profiles was explained in Sect. 5.1.2. For this method, the gradients of each measurement bin were calculated and segments of the profile were defined with the same sign in the bin gradients. For each of these segments a gradient could be calculated. Only gradients larger than 0.4 g kg^{-1} per 100 m were used for the further analysis. Fig. 5.14 shows the determined gradients of all selected profiles. Beside the gradient of each segment, its absolute difference in the WVMR was calculated and is shown as size of the circles. The larger gradients occur between October and December during the negative or the transition phase of the AO. Moreover the absolute difference in the WVMR is larger during this time, which is related to the conclusion from the statistics before of larger maximum values of the WVMR and the layer IWV during the negative AO phase. There is a number of points in the first half of the plot at low heights with similar size and gradients, which could be related to the observed peak in the WVMR in many profiles. By excluding the lowest 30 m, most of the peaks are excluded, but for some cases the negative gradient of the peak is still included. Thus, those points can not be taken into consideration in this study, because the origin of those peaks was not evaluated here. Nevertheless, more strong gradients in lower heights are observed between October and December. In January and February, most of the points are above 600 m with low differences in the WVMR. It is to notice, that the analysis only covers layers with a constantly positive or negative gradient. Changes of the sign over one just bin are included in the layers, but changes over more than one bin separate two layers. The noise of the lidar signal increase for small WVMR's, which is the case especially during the positive phase of the AO in January and February. Larger signal noise influences the calculated

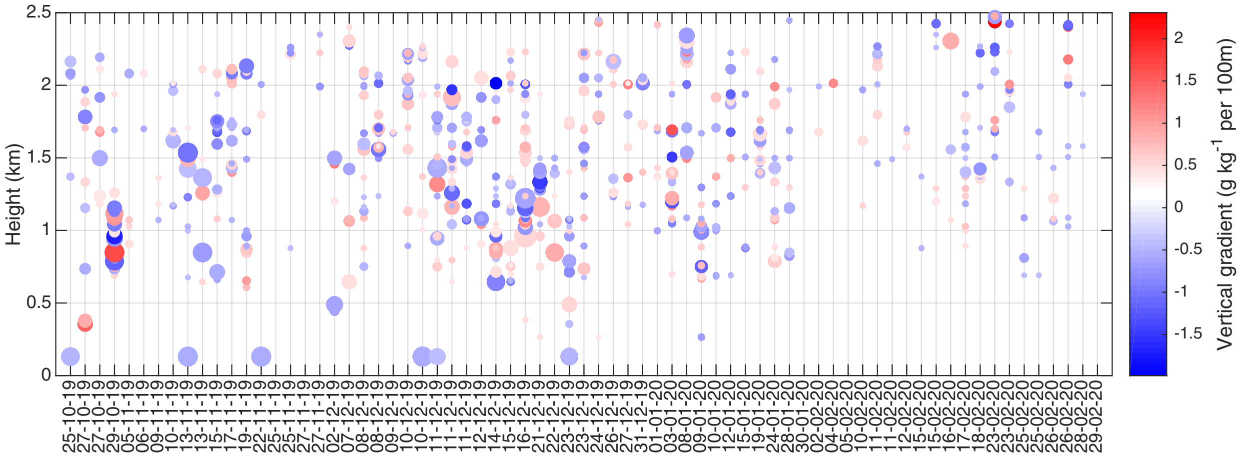

Figure 5.14: Analysis of the occuring gradients larger than 0.4 g kg^{-1} per 100 m in all selected profiles. The shown gradients are calculated over layers with the same sign in the gradient over 1 bin. The height of the markers are the upper height of those layers. The colors represent the vertical gradient over the layer, the size of the points represent the absolute difference in the WVMR.

gradients and absolute differences in the WVMR and could lead to a missinterpretation of the results. Excluding gradients over just one bin, counteract this influence.

To sum up, larger gradients are observed during the negative phase of the AO, they cover a larger range of WVMR values and occur in lower heights. In contrast, smaller gradients, over low WVMR ranges and in greater heights dominate during the positive phase of the AO.

The calculated gradients from both methods are influenced by the data processing of the lidar data and their noise. All profiles are processed equally, which makes them comparable, but the lidar noise differs with the amount of water vapour and is thus different at each measurement time.

Chapter 6

Conclusion and Outlook

Vertical profiles of water vapour were measured for the first time in the Central Arctic during the MOSAiC campaign. Continuous measurements of the Raman lidar PollyXT delivered high-resolved vertical profiles of the water vapour mixing ratio (WVMR) during the polar night in the Arctic winter. The collected data were calibrated within this work and first analyses were conducted. The time period between 25 October 2019 and 29 February 2020 was used for both, the calibration and the analyses. Beside, radiosonde profiles were used to get information about the air temperature, the air density and the wind. The integrated water vapour (IWV) was taken from two different microwave radiometers. A pyrgeometer delivered measurements of the downward longwave radiation (DLR) for correlations with the vertical distributed water vapour.

Profiles of the WVMR were derived from the Raman signals of water vapour and nitrogen. The differential transmission at the two wavelengths and the dependence of the signal ratio on the temperature of the atmospheric scatterers was considered in the calculations, as well as the calibration constant. The signals were smoothed temporally and vertically according to the balance between minimising the signal noise to improve the data quality and keeping the resolution of the atmospheric variability. The calculation of the IWV from the WVMR profiles shown in (Foth et al., 2015) could be improved by implementing the vertical profile of the air density in the calculations. An error analysis was done for the total lidar data processing to derive the uncertainties of the resulting WVMR profiles and values of the IWV.

A calibration is needed to determine calibrated profiles of the WVMR. Three calibration methods were presented and compared for the MOSAiC winter data using radiosonde profiles or the IWV from a microwave radiometer. The calibration with a radiosonde profile was done height-related with the profile method or height-independent with the linear fit method. While the calibration with a radiosonde profile is only possible at the times of radiosonde launches, which means every 6 hours for MOSAiC, the calibration with IWV can be done continuously. All methods are limited to clear-sky periods. The data processing and the choice of the SNR threshold is crucial for the calibration and was adapted to the very dry conditions in the Arctic for each method. Each lidar profile reaches a different maximum height due to the exclusion of data with a SNR below a certain threshold. Thus, a height-correction was implemented in the calculation of the lidar IWV to make it comparable with the IWV of the total atmospheric column, which was measured by the microwave radiometer (MWR). The lidar IWV shows large uncertainties, so that the temporal smoothing was increased to 30 minutes, which requires cases with a stable layering over time for the calibrations. Two criteria were defined for the calibration with IWV to get reasonable and comparable results. The mean relative error of the lidar IWV had to be smaller than 30% and the height coverage of the lidar IWV should amount to

more than 90% of the total IWV in average for each case. The calibration with radiosonde requires also stable conditions, but only for a short time period around the radiosonde launch. It was found, that the height range, which is used for the calibration is crucial, because of the difference of the lidar and the radiosonde profile in larger heights. Reasons for the differences in the vertical profiles are the drift of the radiosonde with the wind, the time it needs for ascending and the averaging time of the lidar data. Hence, the calibration height range was started close to the surface for all cases, but the maximum height was chosen individually for each profile. The maximum height was adapted manually for each profile, so that the correlation coefficient is larger than 0.9 for the linear fit and the standard deviation of the calibration constant from the profile method is below 10%. The latter condition was set to a maximum standard deviation of 5% for the calibration constant from the profile method with some exceptions. It was found, that a smaller height range is better for the profile method, because of the drift of the radiosonde in larger heights. In contrast, a larger height range delivers often a more accurate calibration constant from the linear fit method (with a higher correlation coefficient), because of the coverage of a larger range of WVMR values.
In total, 55 cases were used for the determination of a mean calibration constant for each method. The linear fit and the profile method delivered similar constants of $15.96 \pm 0.37\,\mathrm{g\,kg^{-1}}$ and $16.01 \pm 0.35\,\mathrm{g\,kg^{-1}}$, respectively, but the errors of each single calibration constant is much larger for the profile method. In contrast, the mean calibration constant from the IWV method is with $16.36 \pm 0.36\,\mathrm{g\,kg^{-1}}$ larger than the constants from the radiosonde methods. The reason for this deviation is attributed to the large uncertainties in the lidar IWV at the dry conditions in the Arctic and a small overestimation of the IWV from the MWR LHUMPRO in comparison with the radiosonde. Considering all the described facts, it was chosen to use the determined mean calibration constant from the linear fit method. This calibration constant is now applied on all WVMR profiles of the time period between 25 October 2019 and 29 February 2020.
The lidar measurements are limited by clouds and low signals. WVMR profiles can be derived up to the cloud base during cloudy conditions or up to the height, where the SNR reaches a defined threshold at clear-sky conditions. This work concentrated on the evaluation of the vertical water vapour distribution during clear-sky conditions, because of its influence on the longwave radiation budget and its relation to the surface temperatures.

The analyses of the water vapour profiles were conducted to examine three research questions. Firstly, the vertical distribution of water vapour was examined in general. The amount of water vapour is very small during the Arctic winter with values of the WVMR below $2\,\mathrm{g\,kg^{-1}}$. The maximum WVMR of each profile fluctuates between higher and lower values in periods of weeks. The lowest maximum WVMR of the selected cases was measured end of February with $0.28\,\mathrm{g\,kg^{-1}}$ and the highest value was reached on 19 November 2019 with $1.94\,\mathrm{g\,kg^{-1}}$. A comparison with the temperature profiles showed a clear relation between higher WVMR and warmer temperatures. On the one hand, warmer air can contain more water vapour. On the other hand, large amounts of water vapour influences the temperature by emitting longwave radiation. A very strong surface inversion was found in the temperature profiles most of the time in the Arctic winter, but also some cases with warmer surface temperatures. Most of the profiles contain more than one temperature inversion, which leads to a very stable layering. Case studies showed, that water vapour layers often are limited by temperature inversions at their top and bottom. Hence, temperature inversions were used for a separation of the WVMR profiles into layers, which belong to different airmasses. Two cases of layering could be distinguished. For most cases, the highest amount of water vapour is captured in the lowest layer below the strong surface inversion, which may be an indication for a coupling of the moisture to the surface. In other cases, the largest amounts of water vapour are located in a lofted layer,

which is decoupled from the surface and can be an indication for advection.
The automatic separation of the WVMR profiles into layers by using the height of local minima in the profiles delivered also two cases of layering. Firstly, many cases show a shallow surface layer below 200 m height with low layer IWV and the highest layer IWV in the second layer. The shallow surface layer covers mostly a peak in the WVMR, which was observed in many lidar profiles close to the surface and could be an influence of the ship at specific weather conditions. Secondly, there are cases with the highest IWV in the lowest layer and a decreasing layer IWV in the layers above, where the moisture seems to be coupled to the surface. Beside, there are cases with very low IWV in all layers, that still can be assigned to one of the first two cases. The automatic separation into layers strongly depends on the lidar data processing and fluctuations in the vertical WVMR profile, but gives a good overview over the vertical distribution of the water vapour. Independent of the method for layer separation, there are cases with higher total IWV and very low total IWV. The height of the observed water vapour layers, which means layers with a higher IWV, differs for each case, but is mostly below 2 km height.
The investigation of the gradients in the WVMR profile yielded to a normal distribution of the occuring gradients over 5 bins with a small peak at strong positive gradients. The gradients are small in most of the heights, but some strong positive and strong negative gradients occur at the boundaries of water vapour layers. More and stronger large positive gradients were found, which implies more clear boundaries at the base of water vapour layers than at their top. The calculated gradients are influenced by the vertical fluctuations in the lidar profile due to the atmospheric variability, but also due to the residual instrumental noise.

The atmospheric water vapour content influences the downward longwave radiation (DLR) at the surface (Doyle et al., 2011; Ghatak & Miller, 2013). Correlations of selected cases were investigated to answer the second research question about the influence of the vertical distributed water vapour on the DLR during cloudfree conditions. The comparison of the IWV calculated from lidar profiles and the DLR showed a very good correlation during clear-sky periods. It is crucial to choose a height range of the WVMR profiles, that covers the main amount and variability of water vapour to calculate an appropriate IWV, that can be correlated with the DLR. A linear correlation was found between the IWV and the DLR for each of 7 selected clear-sky cases, but with an offset in the DLR and differences in the slope. The impact of the integrated water vapour on the DLR could be determined to $9.33 - 15.03\,\mathrm{W\,kg^{-1}}$. The different offsets in the linear fit between the DLR and the IWV could be explained by the temperature of the largest amounts of water vapour in each profile. The same amount of water vapour causes higher DLR at warmer temperatures. Comparing the temperature of the largest amounts of water vapour with the radiation temperature of the total sky, which was derived from the Stefan-Boltzmann-law and the measured DLR, delivered a linear correlation between those two parameters for the selected cases. The spread around the linear fit could be caused by the amount of water vapour. It could be found, that the choice of completely cloudfree cases with similar conditions is crucial to get a linear correlation. The largest deviation from the general behaviour of both correlations belonged to one specific case, that differs from all the others, because it is influenced by a dissolving cloud. The linear correlation between the 90. percentile temperature and the radiation temperature of the total sky implies, that the WVMR values larger than the 90. percentile of each profile contribute similarly to the measured total DLR at the surface for all selected cases. This result confirms, that the largest WVMR values determine the DLR during clear-sky conditions. The results of the correlation between the IWV and the DLR are in a good agreement with findings from model studies of (Ghatak & Miller, 2013) as far as they are comparable due to different temporal and horizontal scales.

The third research question of this work had the aim to investigate a possible correlation of the Arctic Oscillation (AO) index to the vertical distributed water vapour in the Arctic. The relation of the water vapour conditions to the atmospheric circulation and the meridional transport was already described in many studies (Vázquez et al., 2016; Nash et al., 2018; Naakka et al., 2019; Nygård et al., 2019, 2020). In this work, the Arctic Oscillation index was used to quantify the general atmospheric circulation in the Arctic. While very stable conditions with weak exchange with lower latitudes are expected during the positive phase of the AO, a stronger meridional transport is expected during the negative phase of the AO. Two case studies showed very different amounts and vertical structures of water vapour for positive and negative AO indices. The statistical evaluation of 71 cases confirmed the differences. Although fluctuations in the maximum WVMR occur during the whole time period, the maximum values of the WVMR profiles and the WVMR range of each single profile were larger during the negative phase of the AO. Beside, also the maximum layer IWV was larger. In accordance with the larger amounts of water vapour, the vertical gradients were stronger and covering larger absolute differences in the WVMR. Considering only the largest absolute values of the gradients, they were located in lower heights. Moreover, the temperatures were higher during the time of the negative phase of the AO, which could be related to a stronger meridional transport, that carries warm and moist air into the Arctic. Beside the stronger meridional transport, stronger or more storms could be possible reasons for higher WVMR's at negative AO indices. Strong storms lead to cracks in the sea ice and opened leads and polynyas are a further source of water vapour. In contrast, the atmospheric conditions were very stable during the positive phase of the AO with stronger surface inversions in temperature and low amounts of water vapour, but also colder temperatures. Less strong gradients were found covering lower ranges of WVMR. The meridional transport is weak during phases with positive AO indices, leading to less exchange with lower latitudes, less advection of warmer and moist air and an enclosure of the Arctic air mass. The atmospheric conditions were exceptional in the evaluated time period, because of the very strong positive phase of the AO during January to March 2020. It could be seen, that the amount and vertical structure of water vapour is not only related to the atmospheric circulation, but also to the air temperature, which depends on the season and the synoptics. Rinke et al. (2021) showed, that the air temperatures and also the total column water vapour usually decrease between October and February according to the long-term mean. Hence, it can not be concluded, that the decreasing trend in temperature, maximum WVMR and layer IWV in the used data is related to the AO. In contrast, the fluctuations between high and low amounts of water vapour and related warmer or colder temperatures can not be seen in the long-term mean (Rinke et al., 2021), but could be related to the synoptic conditions. Time periods with higher layer IWV and higher maximum WVMR in the profile could be related to specific synoptic events, namely the passing of a cyclone or an inflow from the direction of Laptev, Kara or Barents Sea. Thus, two main sources could be determined for advected water vapour in the Central Arctic. The specified source region is in a good agreement with the findings of Vázquez et al. (2016) for the location of the Polarstern northeast of Siberia.

The results show, that the continuously and vertically high-resolved measurements of a Raman lidar deliver a great data set for different analyses and process studies. It was shown, that the Raman lidar captures the low amounts of water vapour in the Arctic with a very good vertical and temporal resolution, that allows studies of the temporal evolution of the vertical distibuted water vapour and its influence on surface parameters. Further investigations should quantify the impact of the water vapour on the DLR and the surface temperature during clear-sky conditions with radiative transfer modeling. Beside, the measurements can be used to validate the input of reanalyses data into radiative transfer models. The sources of water vapour in different heights should be quantified with backward trajectories. As this work concentrated on clear-sky conditions, further investigations could evaluate profiles of WVMR and relative humidity below clouds and the influence of the vertical distributed water vapour on cloud processes.

Chapter 7

Bibliography

Andreas, E. L., Guest, P. S., Persson, P. O. G., Fairall, C. W., Horst, T. W., Moritz, R. E., & Semmer, S. R. (2002). Near-surface water vapor over polar sea ice is always near ice saturation. *Journal of Geophysical Research: Oceans*, 107(C10), SHE–8.

Boeke, R. C. & Taylor, P. C. (2018). Seasonal energy exchange in sea ice retreat regions contributes to differences in projected Arctic warming. *Nature communications*, 9(1), 1–14.

Bucholtz, A. (1995). Rayleigh-scattering calculations for the terrestrial atmosphere. *Applied optics*, 34(15), 2765–2773.

Chahine, M. T. (1992). The hydrological cycle and its influence on climate. *Nature*, 359(6394), 373–380.

Dai, G., Althausen, D., Hofer, J., Engelmann, R., Seifert, P., Bühl, J., Mamouri, R.-E., Wu, S., & Ansmann, A. (2018). Calibration of Raman lidar water vapor profiles by means of AERONET photometer observations and GDAS meteorological data. *Atmospheric Measurement Techniques*, 11(5), 2735–2748.

Devasthale, A., Tjernström, M., Caian, M., Thomas, M. A., Kahn, B. H., & Fetzer, E. J. (2012). Influence of the arctic oscillation on the vertical distribution of clouds as observed by the a-train constellation of satellites. *Atmospheric Chemistry and Physics*, 12(21), 10535–10544. `https://doi.org/10.5194/acp-12-10535-2012`

Doyle, J., Lesins, G., Thackray, C., Perro, C., Nott, G., Duck, T., Damoah, R., & Drummond, J. (2011). Water vapor intrusions into the high arctic during winter. *Geophysical research letters*, 38(12).

Ebell, K., Walbröl, A., Engelmann, R., Griesche, H., Radenz, M., Hofer, J., & Althausen, D. (2022). *Temperature and humidity profiles, integrated water vapour and liquid water path derived from the HATPRO microwave radiometer onboard the Polarstern during the MOSAiC expedition.* `https://doi.org/10.1594/PANGAEA.941389`

Elgered, G., Rönnäng, B., & Askne, J. (1982). Measurements of atmospheric water vapor with microwave radiometry. *Radio Science*, 17(5), 1258–1264.

Engelmann, R., Ansmann, A., Ohneiser, K., Griesche, H., Radenz, M., Hofer, J., Althausen, D., Dahlke, S., Maturilli, M., Veselovskii, I., et al. (2021). Wildfire smoke, Arctic haze, and aerosol effects on mixed-phase and cirrus clouds over the North Pole region during MOSAiC: an introduction. *Atmospheric Chemistry and Physics*, 21(17), 13397–13423.

Engelmann, R., Kanitz, T., Baars, H., Heese, B., Althausen, D., Skupin, A., Wandinger, U., Komppula, M., Stachlewska, I. S., Amiridis, V., et al. (2016). The automated multiwavelength Raman polarization and water-vapor lidar PollyXT: the neXT generation. *Atmospheric Measurement Techniques*, 9(4), 1767–1784.

Foth, A., Baars, H., Di Girolamo, P., & Pospichal, B. (2015). Water vapour profiles from Raman lidar automatically calibrated by microwave radiometer data during HOPE. *Atmospheric Chemistry and Physics*, 15(14), 7753–7763.

Gerding, M., Ritter, C., Müller, M., & Neuber, R. (2004). Tropospheric water vapour soundings by lidar at high Arctic latitudes. *Atmospheric research*, 71(4), 289–302.

Ghatak, D. & Miller, J. (2013). Implications for Arctic amplification of changes in the strength of the water vapor feedback. *Journal of Geophysical Research: Atmospheres*, 118(14), 7569–7578.

Graversen, R. G., Mauritsen, T., Tjernström, M., Källén, E., & Svensson, G. (2008). Vertical structure of recent Arctic warming. *Nature*, 451(7174), 53–56.

Heese, B., Flentje, H., Althausen, D., Ansmann, A., & Frey, S. (2010). Ceilometer lidar comparison: backscatter coefficient retrieval and signal-to-noise ratio determination. *Atmospheric Measurement Techniques*, 3(6), 1763–1770.

Herold, C., Althausen, D., Müller, D., Tesche, M., Seifert, P., Engelmann, R., Flamant, C., Bhawar, R., & Di Girolamo, P. (2011). Comparison of Raman lidar observations of water vapor with COSMO-DE forecasts during COPS 2007. *Weather and forecasting*, 26(6), 1056–1066.

Hogan, R. J. & Bozzo, A. (2018). A flexible and efficient radiation scheme for the ecmwf model. *Journal of Advances in Modeling Earth Systems*, 10(8), 1990–2008.

Jacob, D. (2001). The role of water vapour in the atmosphere. a short overview from a climate modeller's point of view. *Physics and Chemistry of the Earth, Part A: Solid Earth and Geodesy*, 26(6-8), 523–527.

Janssen, M. A. (1994). Atmospheric remote sensing by microwave radiometry.

Kraus, H. (2007). *Die Atmosphäre der Erde: Eine Einführung in die Meteorologie*. Springer-Verlag.

Krumpen, T., Belter, H. J., Boetius, A., Damm, E., Haas, C., Hendricks, S., Nicolaus, M., Nöthig, E.-M., Paul, S., Peeken, I., et al. (2019). Arctic warming interrupts the transpolar drift and affects long-range transport of sea ice and ice-rafted matter. *Scientific Reports*, 9(1), 1–9.

Lawrence, Z. D., Perlwitz, J., Butler, A. H., Manney, G. L., Newman, P. A., Lee, S. H., & Nash, E. R. (2020). The remarkably strong Arctic stratospheric polar vortex of winter 2020: Links to record-breaking Arctic Oscillation and ozone loss. *Journal of Geophysical Research: Atmospheres*, 125(22), e2020JD033271.

Maturilli, M., Holdridge, D. J., Dahlke, S., Graeser, J., Sommerfeld, A., Jaiser, R., Deckelmann, H., & Schulz, A. (2021). *Initial radiosonde data from 2019-10 to 2020-09 during project MOSAiC*. `https://doi.org/10.1594/PANGAEA.928656`

Measures, R. M. (1984). Laser remote sensing: Fundamentals and applications (Book). *New York, Wiley-Interscience, 1984, 521 p.*

Mech, M., Kliesch, L.-L., Anhäuser, A., Rose, T., Kollias, P., & Crewell, S. (2019). Microwave Radar/radiometer for Arctic Clouds (MiRAC): first insights from the ACLOUD campaign. *Atmospheric Measurement Techniques*, 12(9), 5019–5037.

Melfi, S., Lawrence Jr, J., & McCormick, M. (1969). Observation of raman scattering by water vapor in the atmosphere. *Applied Physics Letters*, 15(9), 295–297.

Melfi, S. & Whiteman, D. (1985). Observation of lower-atmospheric moisture structure and its evolution using a raman lidar. *Bulletin of the American Meteorological Society*, 66(10), 1288–1292.

Naakka, T., Nygård, T., & Vihma, T. (2018). Arctic humidity inversions: Climatology and processes. *Journal of Climate*, 31(10), 3765–3787.

Naakka, T., Nygård, T., Vihma, T., Sedlar, J., & Graversen, R. (2019). Atmospheric moisture transport between mid-latitudes and the Arctic: Regional, seasonal and vertical distributions. *International Journal of Climatology*, 39(6), 2862–2879.

Nash, D., Waliser, D., Guan, B., Ye, H., & Ralph, F. M. (2018). The role of atmospheric rivers in extratropical and polar hydroclimate. *Journal of Geophysical Research: Atmospheres*, 123(13), 6804–6821.

Nygård, T., Graversen, R. G., Uotila, P., Naakka, T., & Vihma, T. (2019). Strong dependence of wintertime arctic moisture and cloud distributions on atmospheric large-scale circulation. *Journal of Climate*, 32(24), 8771–8790.

Nygård, T., Naakka, T., & Vihma, T. (2020). Horizontal moisture transport dominates the regional moistening patterns in the Arctic. *Journal of Climate*, 33(16), 6793–6807.

O'Gorman, P. A. & Muller, C. J. (2010). How closely do changes in surface and column water vapor follow Clausius–Clapeyron scaling in climate change simulations? *Environmental Research Letters*, 5(2), 025207. `https://doi.org/10.1088/1748-9326/5/2/025207`

Ohneiser, K., Ansmann, A., Chudnovsky, A., Engelmann, R., Ritter, C., Veselovskii, I., Baars, H., Gebauer, H., Griesche, H., Radenz, M., et al. (2021). The unexpected smoke layer in the High Arctic winter stratosphere during MOSAiC 2019–2020. *Atmospheric Chemistry and Physics*, 21(20), 15783–15808.

Perovich, D., Meier, W., Tschudi, M., Farrell, S., Hendricks, S., Gerland, S., Haas, S., Krumpen, T., Polashenski, C., Ricker, R., et al. (2019). The arctic sea ice cover inßtate of the climate in 2018". *Bull. Am. Meteorol. Soc*, 100, S146–S150.

Persson, O. & Vihma, T. (2017). The atmosphere over sea ice. *Sea ice*, 160–196.

Rinke, A., Cassano, J. J., Cassano, E. N., Jaiser, R., & Handorf, D. (2021). Meteorological conditions during the mosaic expedition: Normal or anomalous? *Elem Sci Anth*, 9(1), 00023.

Rinke, A., Segger, B., Crewell, S., Maturilli, M., Naakka, T., Nygård, T., Vihma, T., Alshawaf, F., Dick, G., Wickert, J., et al. (2019). Trends of vertically integrated water vapor over the Arctic during 1979–2016: Consistent moistening all over? *Journal of Climate*, 32(18), 6097–6116.

Rose, T., Crewell, S., Löhnert, U., & Simmer, C. (2005). A network suitable microwave radiometer for operational monitoring of the cloudy atmosphere. *Atmospheric research*, 75(3), 183–200.

Ruckstuhl, C., Philipona, R., Morland, J., & Ohmura, A. (2007). Observed relationship between surface specific humidity, integrated water vapor, and longwave downward radiation at different altitudes. *Journal of Geophysical Research: Atmospheres*, 112(D3).

Screen, J. A. & Simmonds, I. (2010). The central role of diminishing sea ice in recent Arctic temperature amplification. *Nature*, 464(7293), 1334–1337.

Serreze, M. C. & Barry, R. G. (2014). *The Arctic climate system*. Cambridge University Press.

Shupe, M., Rex, M., Dethloff, K., Damm, E., Fong, A., Gradinger, R., Heuzé, C., Loose, B., Makarov, A., Maslowski, W., et al. (2020). The mosaic expedition: A year drifting with the arctic sea ice. *Arctic report card*.

Shupe, M. D., Rex, M., Blomquist, B., Persson, P. O. G., Schmale, J., Uttal, T., Althausen, D., Angot, H., Archer, S., Bariteau, L., et al. (2022). *Overview of the mosaic expedition: Atmosphere*.

Spreen, G., Kaleschke, L., & Heygster, G. (2008). Sea ice remote sensing using amsr-e 89-ghz channels. *Journal of Geophysical Research: Oceans*, 113(C2). `https://doi.org/doi:10.1029/2005JC003384`

Survo, P., Turunen, M., Salo, T., & Jauhiainen, H. (2014). *Vaisala radiosonde RS41–new sensing technologies for operational upper air measurements*.

Thompson, D. W. & Wallace, J. M. (1998). The Arctic Oscillation signature in the wintertime geopotential height and temperature fields. *Geophysical research letters*, 25(9), 1297–1300.

Timmermans, M.-L. & Marshall, J. (2020). Understanding arctic ocean circulation: A review of ocean dynamics in a changing climate. *Journal of Geophysical Research: Oceans*, 125(4), e2018JC014378.

Uttal, T., Curry, J. A., McPhee, M. G., Perovich, D. K., Moritz, R. E., Maslanik, J. A., Guest, P. S., Stern, H. L., Moore, J. A., Turenne, R., et al. (2002). Surface heat budget of the Arctic Ocean. *Bulletin of the American Meteorological Society*, 83(2), 255–276.

Vázquez, M., Nieto, R., Drumond, A., & Gimeno, L. (2016). Moisture transport into the arctic: Source-receptor relationships and the roles of atmospheric circulation and evaporation. *Journal of Geophysical Research: Atmospheres*, 121(22), 13–493.

Walbröl, A., Konjari, P., Engelmann, R., Griesche, H., Radenz, M., Hofer, J., Althausen, D., Crewell, S., & Ebell, K. (2021). First insight into thermodynamic profiles, IWV and LWP from ground-based microwave radiometers during MOSAiC. *EGU General Assembly Conference 2021, online, 19-30 Apr 2021*. `https://doi.org/https://doi.org/10.5194/egusphere-egu21-9053`

Walbröl, A., Orlandi, E., Crewell, S., & Ebell, K. (2022). *Integrated water vapour derived from the MiRAC-P microwave radiometer onboard the Polarstern during the MOSAiC expedition*. `https://doi.org/10.1594/PANGAEA.941470`

Wandinger, U. (2005). Raman lidar. *Lidar - range-resolved optical remote sensing of the atmosphere*, 241–271. Springer.

Weitkamp, C. (2006). *Lidar: range-resolved optical remote sensing of the atmosphere*, volume 102. Springer Science & Business.

Wendisch, M., Brückner, M., Burrows, J., Crewell, S., Dethloff, K., Ebell, K., Lüpkes, C., Macke, A., Notholt, J., Quaas, J., et al. (2017). Understanding causes and effects of rapid warming in the Arctic. *Eos*, 98.

Whiteman, D. N. (2003a). Examination of the traditional Raman lidar technique. i. Evaluating the temperature-dependent lidar equations. *Applied Optics*, 42(15), 2571–2592.

Whiteman, D. N. (2003b). Examination of the traditional Raman lidar technique. ii. Evaluating the ratios for water vapor and aerosols. *Applied optics*, 42(15), 2593–2608.

List of Symbols

Symbol	Description	Unit
α_λ	atmospheric extinction coefficient at the wavelength λ	$\mathrm{m^{-1}}$
A	fraction of the total IWV, that is covered by the lidar IWV ($I_{\mathrm{RS,part}}/I_{\mathrm{RS}}$)	–
$\beta^{\mathrm{m}}_\lambda$	total molecular volume scattering coefficient	$\mathrm{m^{-1}}$
β_{R}	Raman backscattering coefficient	$\mathrm{m^2\,sr^{-1}}$
$\mathrm{C_{H_2O}}$	calibration constant for the WVMR of the lidar	$\mathrm{g\,kg^{-1}}$
δ_x	standard deviation of the quantity x	unit of x
Δx	error of the quantity x due to measurement uncertainties	unit of x
ΔT_{r}	differential transmission term	–
e_{sat}	saturation pressure	hPa
$F_{387}{=}F_{\mathrm{N_2}}[T]$, $F_{407}{=}F_{\mathrm{H_2O}}[T]$	temperature dependent term of the lidar equation at the wavelengths 387 nm and 407 nm	–
F_{LW}	broadband longwave radiation	$\mathrm{W\,m^{-2}}$
I	integrated water vapour	$\mathrm{kg\,m^{-2}}$
λ_0, λ_{R}	emitted wavelength of the laser, wavelength of the Raman scattered radiation	nm
$\lambda_{\mathrm{H_2O}}$, $\lambda_{\mathrm{N_2}}$	wavelength of the Raman scattered radiation by water vapour or nitrogen molecules	nm
$m_{\mathrm{H_2O}}$, m_{air}	mass of water vapour and dry air	kg
μ_{n}	mean value of the normal distribution	–
N	molecular number density	$\mathrm{cm^{-3}}$
$O(z)$	Overlap function	–
p	pressure	hPa
P_{R}, P_{bg}, P_{sig}	measured lidar signal at a specific wavelength, background signal, signal of the backscattered photons	counts
$\rho_{\mathrm{H_2O}}$, ρ_{air}	density of water vapour and dry air	$\mathrm{kg\,m^{-3}}$
R_{F}	$F_{\mathrm{N_2}}[T(z)]/F_{\mathrm{H_2O}}[T(z)]$, ratio of the temperature dependent terms for nitrogen and water vapour	–
R_{w}	$P_{\mathrm{H_2O}}(z)/P_{\mathrm{N_2}}(z)$, ratio of the lidar signals	–
$\mathrm{R_d}$	individual gas constant for dry air ($\mathrm{R_d}$=287.06 $\mathrm{J\,kg^{-1}\,K^{-1}}$)	$\mathrm{J\,kg^{-1}\,K^{-1}}$
R^2	correlation coefficient of the linear fit	–
σ^{m}	total Rayleigh scattering cross section	$\mathrm{cm^2}$
σ^{m}_π	Rayleigh backscattering cross section	$\mathrm{cm^2\,sr^{-1}}$
σ_x	uncertainty of a quantity x	unit of x
σ_{n}	standard deviation of the normal distribution	–
S	signal-to-noise ratio	–
T	temperature	°C, K
T_{rad}	radiation temperature of the sky	K
u	relative humidity	%
$w_{\mathrm{H_2O}}$	water vapour mixing ratio	$\mathrm{g\,kg^{-1}}$
z	height / distance between the scattering particle and the lidar	m
z_{s}	scale height of the atmosphere	m

List of Abbreviations

Abbreviation	Description
AO	Arctic Oscillation
bg	background
DLR	downward longwave radiation
FWHM	full width at half maximum
GDAS	Global Data Assimilation System
HATPRO	Humidity and Temperature PROfiler
IWV	integrated water vapour
layer IWV	integrated water vapour of an atmospheric layer
lidar	light detection and ranging
LHUMPRO	passive Microwave Radiometer for Arctic Clouds (MiRAC-P)
LWP	liquid water path
m, p	molecular, particle
MOSAiC	Multidisciplinary drifting Observatory for the Study of Arctic Climate
MWR	microwave radiometer
PW	precipitable water vapour
RS	radiosonde
sig	signal
SHEBA	Surface Heat Budget of the Arctic Ocean
SNR	signal-to-noise ratio
TROPOS	Leibniz Institute for Tropospheric Research
WVMR	water vapour mixing ratio
$\mathrm{WVMR}_{\mathrm{uncal}}$	uncalibrated water vapour mixing ratio

List of Figures

2.1 Relationship of DLF and PW from model results 9
2.2 Time series of the AO index and the IWV 10

3.1 Profiles of the molecular extinction and the differential transmission 19
3.2 Signal transmission through the filters at different wavelengths 20

4.1 Correlation of the IWV measured by RS and the MWR LHUMPRO 27
4.2 Calibration with radiosonde using the example case on 27 October 2019 29
4.3 Colorplot for the calibration case on 27 October 2019 31
4.4 Calibration with IWV using the example case on 27 October 2019 31
4.5 Results from the calibration with radiosonde 33
4.6 Results from the calibration with the IWV 34
4.7 Correlation of the calibration constants from different methods 34

5.1 Methods to analyse WVMR profiles 38
5.2 Lidar and radiosonde measurements from 13 November 2019 41
5.3 Downward longwave radiation on 13 November 2019 42
5.4 Gradient analysis for the mean WVMR profile at 13 Nov 2019 19:50-20:00 UTC 43
5.5 Lidar and radiosonde measurements from 11 February 2020 45
5.6 Downward longwave radiation on 11 February 2020 46
5.7 Gradient analysis for the mean WVMR profile at 11 Feb 2020 10:50-11:00 UTC 47
5.8 Correlation of the DLR and the IWV for seven selected cases 49
5.9 Correlation between the radiation temperature of the sky and the 90. percentile temperature 50
5.10 Statistics - Mean, maximum and minimum of WVMR and temperature profiles. 52
5.11 Statistics - Division of the WVMR profiles into layers separated by temperature inversions 54
5.12 Statistics - Division of the WVMR profiles into layers separated by minima in the WVMR profile 55
5.13 Statistics - Frequency of occurence of the vertical gradients 57
5.14 Statistics - Analysis of the occuring gradients larger than 0.4 $\mathrm{g\,kg^{-1}}$ per 100 m . 58

A.1 Synoptics and sea ice concentration for the case on 13 November 2019 73

A.2 Synoptics and sea ice concentration for the case on 11 February 2020 74

List of Tables

5.1 Cases for the correlation of DLR and IWV 49
5.2 Parameters of the normal distributions for all gradients 56

Appendix A

Additional figures

A.1 Synoptic conditions for the case studies

Two case studies were presented. The synoptic weather map and the observed sea ice concentration are shown here for the two dates to bring the results from the water vapour and radiation measurements in context with the actual atmospheric circulation. The sea ice concentration was derived from satellite measurements by Spreen et al. (2008) and is used to investigate areas with an ice-free ocean. The data of the sea ice concentration for the 13 November 2019 and the 11 February 2020 originate from `https://www.meereisportal.de` (funding: REKLIM-2013-04).

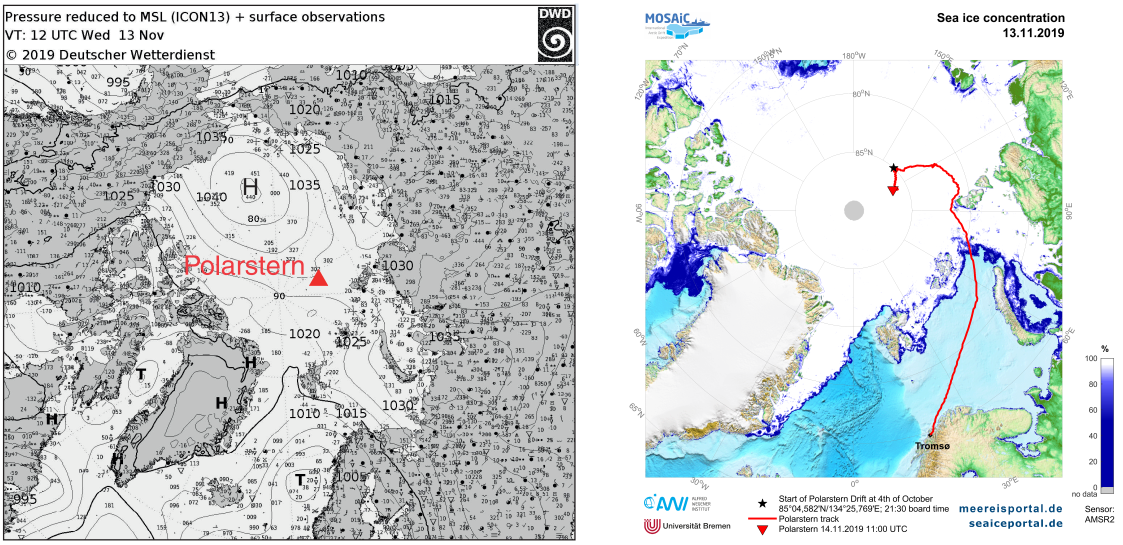

(a) The synoptic map showed a strong high pressure system over the Beaufort sea causing southerly winds from the direction of the Laptev Sea at the location of the Polarstern.

(b) Sea ice concentration of the Arctic Ocean from meereisportal.de (Spreen et al., 2008). The Arctic Ocean was covered completely by sea ice in the area of the Laptev Sea, where the airmasses came from based on the synoptics.

Figure A.1: Synoptics and sea ice concentration for the case on 13 November 2019.

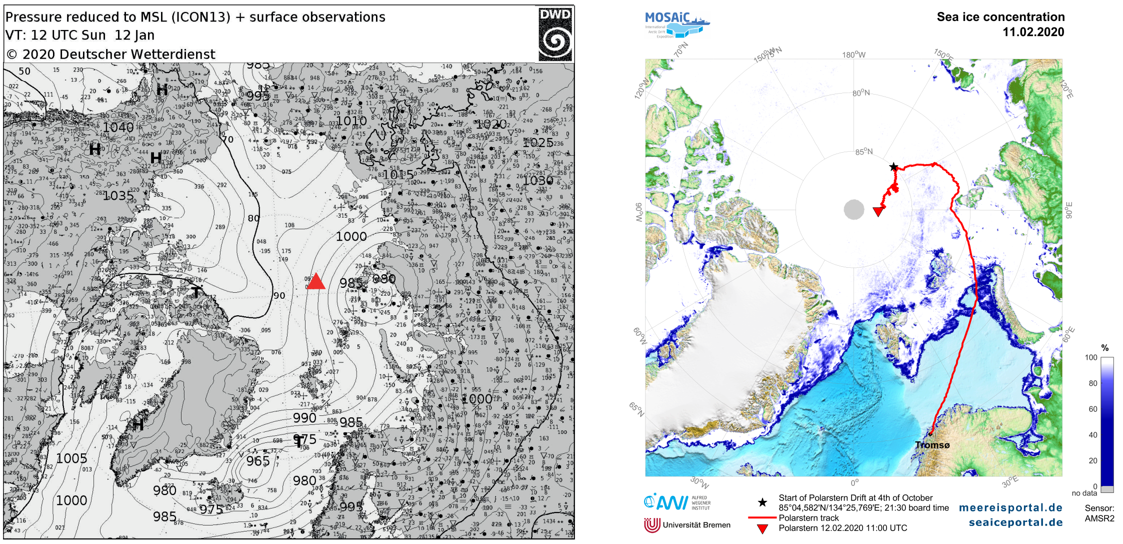

(a) The synoptics show a low pressure system over the Kara Sea and high pressure over North America, which caused winds from east to southeast at the location of Polarstern.

(b) Sea ice concentration of the Arctic Ocean from meereisportal.de (Spreen et al., 2008). The Arctic Ocean was covered completely by sea ice in the area of the Laptev Sea, where the airmasses came from based on the synoptics.

Figure A.2: Synoptics and sea ice concentration for the case on 11 February 2020.

Selbstständigkeitserklärung

Hiermit bestätige ich, dass ich die vorliegende Masterarbeit selbstständig verfasst und keine anderen als die angegebenen Quellen und Hilfsmittel verwendet habe. Jegliche verwendete Literatur oder andere Quelle wurde als solche gekennzeichnet und zitiert. Alle Abbildungen ohne Quellenangabe habe ich über die durch meinen Betreuer zur Verfügung gestellten Daten selbst erstellt. Des Weiteren wurde diese Arbeit noch nie in gleicher oder ähnlicher Form bei einer anderen Prüfungsbehörde eingereicht. Ich erkläre mich damit einverstanden, eine positive Bewertung der Arbeit vorausgesetzt, dass Kopien dieser Arbeit in der Bücherei der Fakultät für Physik und Geowissenschaften der Universität Leipzig sowie am Leibniz Institut für Troposphärenforschung in Leipzig zur Verfügung gestellt werden.

Ort, Datum   Unterschrift des Verfassers